

Washington University in St. Louis

## Washington University Open Scholarship

---

All Theses and Dissertations (ETDs)

---

January 2009

### Electrocardiographic Consequences Of Electrical And Anatomical Remodeling In Diabetic And Obese Humans

Shuli Wang

*Washington University in St. Louis*

Follow this and additional works at: <https://openscholarship.wustl.edu/etd>

---

#### Recommended Citation

Wang, Shuli, "Electrocardiographic Consequences Of Electrical And Anatomical Remodeling In Diabetic And Obese Humans" (2009). *All Theses and Dissertations (ETDs)*. 363.

<https://openscholarship.wustl.edu/etd/363>

This Dissertation is brought to you for free and open access by Washington University Open Scholarship. It has been accepted for inclusion in All Theses and Dissertations (ETDs) by an authorized administrator of Washington University Open Scholarship. For more information, please contact [digital@wumail.wustl.edu](mailto:digital@wumail.wustl.edu).

WASHINGTON UNIVERSITY IN ST. LOUIS  
School of Engineering and Applied Science  
Department of Electrical and Systems Engineering

Thesis Examination Committee:  
R. Martin Arthur, Chair  
Tao Ju  
Jr-Shin Li  
Hiroaki Mukai  
Arye Nehorai  
Jason W. Trobaugh  
Kathryn Yamada

ELECTROCARDIOGRAPHIC CONSEQUENCES OF ELECTRICAL AND  
ANATOMICAL REMODELING IN DIABETIC AND OBESE HUMANS

by

Shuli Wang

A dissertation presented to the School of Engineering  
of Washington University in partial fulfillment of the  
requirements for the degree of

DOCTOR OF PHILOSOPHY

December 2009  
Saint Louis, Missouri

copyright by

Shuli Wang

2009

## ABSTRACT OF THE THESIS

Electrocardiographic Consequences of Electrical and Anatomical Remodeling in  
Diabetic and Obese Humans

by

Shuli Wang

Doctor of Philosophy in Electrical Engineering

Washington University in St. Louis, 2009

Research Advisor: Professor R. Martin Arthur

*Background.* Diabetes and obesity are two major risk factors for cardiovascular disease. Both can cause changes due to cardiac sources in body-surface potentials (BSPs), that is, in electrocardiograms (ECGs). By identifying the major effects of diabetes and obesity on BSPs, we hope to reveal the electrical phenotype of diabetes in body-surface ECGs in the presence of obesity.

*Methods.* A Bidomain Platform was constructed to link heart-surface transmembrane potentials (TMPs) and BSPs. The Forward-Problem Module of the platform calculates BSPs from a bidomain-model of myocyte TMPs and torso anatomy. The platform also contains a Cardio-myocyte TMP Estimation Module in which an innovative method, named regularized waveform identification (RWI), was developed. It is a new approach used to reconstruct the TMPs from BSPs, that is, solving the electrocardiographic inverse bidomain problem. Using normal TMPs, BSPs were simulated on obese torsos and compared to BSPs on a normal torso to determine ECG changes that might accompany certain obese habitus. BSPs on a normal torso were also simulated with both normal TMPs and TMPs whose duration was increased in a manner expected to occur in the diabetic. In addition, BSPs were measured, heart and torso models were found on two adult male subjects: one normal and one obese diabetic. BSPs and estimated TMPs in these subjects, found by using the RWI method, were compared to identify ECG changes that might be found in the obese diabetic in a clinical setting.

*Results.* Forward-problem solutions found for obese heart-torso models with normal TMPs compared to normal had relative errors (RE) of 12, 30, and 68% for 20% left-ventricular hypertrophy, 16% abdomen extension, and displaced heart, respectively. These results suggest that standard 12-lead ECG measurement could be significantly affected by the anatomical changes associated with obesity. Simulation results also showed diabetic electrical remodeling may have a strong impact on BSPs. An RE of 125% was observed between normal and diabetic BSPs due to prolongation of recovery that might accompany diabetes. Energy reduction of BSPs was found in both simulated and measured BSPs with obesity. Although QT interval prolongation found in simulated BSPs was not seen in the ECGs recorded from the obese diabetic subject, QT dispersion(QTd) was found increased in diabetic in both simulated and measure ECGs. Obviously, no statistical conclusions can be reached with our limited data set, but the suggestive results call for further clinical observations. TMPs were estimated in realistic, normal heart-torso model simulations using the RWI method. REs of about 15% were found for up to 10% noise added to BSPs; and for errors in heart size of 10% and heart location of  $\pm 1$  cm, which were significant improvements over conventional regularization methods alone.

*Conclusions.* In this study, we characterized electrical changes with diabetes and anatomical changes with obesity; then independently evaluated their influences on body surface potentials (BSPs). These results suggest that standard 12-lead ECG measurements could be strongly influenced by the anatomical changes associated with obesity. Body-surface maps and inverse solutions to the heart-surface that minimize volume-conductor effects are likely to be more useful in investigating the influence of diabetic electrical remodeling among obese diabetic patients. Simulation results showed that the RWI inverse solution performed much better than traditional regularization methods alone and is robust in the presence of noise and geometric error. By incorporating temporal information, in the form of the basic TMP wave shape, estimation accuracy was enhanced while maintaining computational simplicity.

# Acknowledgments

I would like to especially thank my advisor, Dr. Martin Arthur, for his continuous support, guidance, kindness and patience. His spirit and passion in research inspired me throughout the years of my candidature. Without his help, this dissertation would not have been possible.

I would also like to thank other members of my dissertation committee, Dr. Tao Ju, Dr. Jr-Shin Li, Dr. Hiroaki Mukai, Dr. Arye Nehorai, Dr. Jason W. Trobaugh, and Dr. Kathryn Yamada for their willingness to serve on the committee and for their constructive suggestions and help. My appreciation also goes to Dr. Daniel Fuhrmann, the committee member of my Ph.D. proposal examination.

Special thanks to Li Ding and Ken Chen at the Genome Sequencing Center (GSC) at Washington University in St. Louis School of Medicine for the valuable Internship opportunities they provided to me. The technologies I learned there facilitated the implementation of my research. I would also acknowledge Dr. Trobaugh and Prof. Alan Waggoner for their help during the data collection in the body surface potential mapping experiment. In particular, I am also very grateful to Dr. Trobaugh for providing the help and suggestions during my doctoral research.

I would like to express my gratitude to Sandra Matteucci for reviewing the final draft of my dissertation. I would also like to thank my labmates, YuZheng Guo and Debomita Basu for their support throughout my studies. It has been a great pleasure to know and work with them.

Finally, I would like to thank my husband, Yunde, my parents, Fuyuan and Shiyang, and my sister, Qianli for their love and persistent support. Words fail me to express my appreciation to all of them.

Shuli Wang

*Washington University in Saint Louis  
December 2009*

Dedicated to my husband, Yunde, my parents, Fuyuan and Shiyong, and my sister,  
Qianli.

# Contents

<b>Abstract</b> . . . . .	<b>ii</b>
<b>Acknowledgments</b> . . . . .	<b>iv</b>
<b>List of Tables</b> . . . . .	<b>ix</b>
<b>List of Figures</b> . . . . .	<b>x</b>
<b>1 Introduction</b> . . . . .	<b>1</b>
<b>2 Background</b> . . . . .	<b>5</b>
2.1 Effects of Diabetes and Obesity . . . . .	5
2.1.1 Electrical Abnormalities due to Diabetes . . . . .	6
2.1.2 Anatomical Abnormalities due to Obesity . . . . .	9
2.2 Bidomain Forward and Inverse Problems . . . . .	10
2.2.1 Forward Problem . . . . .	11
2.2.2 Inverse Problem . . . . .	13
<b>3 Bidomain Forward Problem</b> . . . . .	<b>15</b>
3.1 Myocyte Transmembrane Potential (TMP) . . . . .	16
3.1.1 Biophysical Context of Transmembrane Potential . . . . .	16
3.2 Bidomain Double-layer Forward Problem . . . . .	17
3.2.1 Bidomain Source Model . . . . .	19
3.2.2 Bidomain Double-layer Forward Problem Model . . . . .	20
3.3 Bidomain Forward Problem Numerical Implement . . . . .	24
3.3.1 Numerical Representation of Transmembrane Potentials . . . . .	24
3.3.2 Numerical Representation of Torso Anatomy . . . . .	28
3.4 Bidomain Forward Problem Verification . . . . .	30
3.4.1 Fundamental Tests . . . . .	31
3.4.2 Homogeneous Volume Test . . . . .	33
3.4.3 Inhomogeneous Volume Test . . . . .	37
<b>4 Bidomain Inverse Problem</b> . . . . .	<b>40</b>
4.1 Problem Statement . . . . .	40
4.2 Theoretical Framework . . . . .	41
4.2.1 Least Squares Estimation (LSE) . . . . .	41
4.2.2 Regularization . . . . .	42



4.2.3	Regularized Waveform Identification (RWI)	44
4.3	Methods and Results	49
4.3.1	Sensitivity of RWI to Electrical Noise	54
4.3.2	Sensitivity of RWI to Geometric Errors	60
4.4	Conclusions	61
<b>5</b>	<b>Obese Anatomical Remodeling</b>	<b>62</b>
5.1	Introduction	62
5.2	Obese Anatomical Features	64
5.2.1	Left Ventricular Hypertrophy (LVH)	64
5.2.2	Heart Displacement in Obesity	65
5.2.3	Abdominal Size Enlargement	66
5.3	Effects of Obese Anatomy on BSPs	67
5.4	Discussions and Conclusions	78
<b>6</b>	<b>Diabetic Electrical Remodeling</b>	<b>79</b>
6.1	Diabetic Electrical Remodeling for TMPs	80
6.2	Effects of Diabetic Electrical Remodeling on BSPs	83
6.3	Discussions and Conclusions	92
<b>7</b>	<b>Geometrical and Electrical Remodeling in Human Subjects</b>	<b>93</b>
7.1	Clinical Data Acquisition	94
7.1.1	Protocol	96
7.1.2	Heart and Torso Geometry	97
7.1.3	Electrical Body-Surface Measurements	97
7.2	Heart and Torso Models	97
7.3	Body Surface Potentials (BSPs)	98
7.4	Heart Surface Transmembrane Potentials (TMPs)	99
7.5	Characteristics of BSPs and TMPs	103
7.6	Conclusions	107
<b>8</b>	<b>Summary, Conclusion and Future Work</b>	<b>109</b>
<b>Appendix A</b>	<b>ECGSIM Simulation Platform</b>	<b>113</b>
<b>Appendix B</b>	<b>Deflation Procedure</b>	<b>115</b>
<b>Appendix C</b>	<b>Torso Extension Routine</b>	<b>117</b>
<b>Appendix D</b>	<b>Clinical Data Acquisition Protocol</b>	<b>121</b>
D.1	Equipment	121
D.2	Preparation	122
D.3	Data Acquisition	123
D.4	Notes	125

Appendix E	Table of Symbols . . . . .	126
References . . . . .		128
Vita . . . . .		139

# List of Tables

2.1	Disease Risk for Type II Diabetes, Hypertension, and CVD <sup>†</sup> . . . . .	11
3.1	Multipole coefficients recovered from BSP integration. . . . .	35
4.1	Relative errors (REs) of TMP reconstruction with noises . . . . .	58
4.2	Correlation coefficient (CC) of TMP reconstruction with noises . . . . .	58
4.3	Relative errors (REs) of repolarization parameters with noises . . . . .	58
4.4	Correlation coefficient (CC) of repolarization parameters with noises . . . . .	59
4.5	RE and CC of epicardial potential (EP) reconstruction with noises . . . . .	60
4.6	RE and CC of TMPs with geometric errors . . . . .	60
5.1	RE of BSPs at R-peak, T-peak and Q-T interval due to obese habitus . . . . .	73
5.2	RE and CC of BSPs due to obese habitus . . . . .	77

# List of Figures

1.1	Bidomain ECG analysis platform . . . . .	4
2.1	12-lead ECG system. . . . .	8
2.2	BMI indicator . . . . .	10
3.1	Schematic representation of cardiac transmembrane potential (TMP) . . . . .	17
3.2	Transmembrane potential (TMP) template . . . . .	25
3.3	Dominant T wave and repolarization TMP template . . . . .	26
3.4	TMP timing parameters from ECGSIM [111]. . . . .	27
3.5	Approximated ECGSIM Transmembrane potentials . . . . .	28
3.6	ECGSIM geometries and lung models . . . . .	29
3.7	ECGSIM ventricle and derived blood mass . . . . .	29
3.8	Solid angle verifications . . . . .	31
3.9	External field of a uniform strength double-layer source . . . . .	32
3.10	A dipole source inside a homogeneous torso . . . . .	34
3.11	BSPs generated by dipole sources inside a homogeneous torso . . . . .	36
3.12	Multipole coefficients recovery. . . . .	36
3.13	Eccentric spheres (ESS) models . . . . .	37
3.14	Simulated and Analytic potentials in ESS test . . . . .	38
4.1	L-curve used in Tikhonov regularization . . . . .	44
4.2	The regularized waveform identification (RWI) scheme . . . . .	50
4.3	The reference TMPs and corresponding BSPs . . . . .	51
4.4	The flow chart of RWI . . . . .	52
4.5	TMPs reconstructed from BSPs without noise . . . . .	53
4.6	Reconstructed repolarization Timing parameters . . . . .	54
4.7	Regularization TMP estimated under 1% white noise. . . . .	55
4.8	TMP waveforms reconstructed under 1% white noise . . . . .	56
4.9	TMP maps reconstructed under 1% white noise . . . . .	57
4.10	The RE and CC of TMP reconstruction . . . . .	59
5.1	Normal and LVH ventricle models . . . . .	64
5.2	Normal and displaced heart models in normal torso . . . . .	65
5.3	Normal and obese torso models . . . . .	66
5.4	Obesity habitus related STD variations . . . . .	68
5.5	Obesity habitus related PSD variations . . . . .	69
5.6	Obesity habitus related PCA variations . . . . .	71
5.7	Obesity habitus related changes in BSPs maps at R-peak . . . . .	73
5.8	Obesity habitus related changes in BSPs maps at T-peak . . . . .	74

5.9	Obesity habitus related changes in iso-integral maps . . . . .	75
5.10	Obesity habitus related changes in 12-lead ECGs . . . . .	77
6.1	ECGSIM ventricle marked at three regions . . . . .	80
6.2	TMPs of normal and diabetic rats . . . . .	81
6.3	APD of normal and diabetic subjects . . . . .	82
6.4	Diabetes related changes in STD . . . . .	84
6.5	Diabetes related changes in PSD . . . . .	86
6.6	Diabetes related changes in PCA . . . . .	87
6.7	The distribution of QT corrections (QTc) . . . . .	89
6.8	Diabetes related changes in BSPs maps at T-peak . . . . .	90
6.9	Diabetes related changes in 12-lead ECGs . . . . .	91
7.1	Portable Mapping System . . . . .	94
7.2	Torso surface measurements . . . . .	95
7.3	Interface of BioSemi ECG Mapping System . . . . .	96
7.4	The torso models of the obese diabetic and normal subjects . . . . .	98
7.5	The signal averaged ECG (SAECG) . . . . .	99
7.6	The BSPs measurements of the normal and obese diabetic subjects . . . . .	100
7.7	BSPs during T wave of the normal and obese diabetic subjects . . . . .	101
7.8	Regularization TMPs of the normal and obese diabetic subjects . . . . .	102
7.9	Averaged TMPs of the normal and obese diabetic subjects . . . . .	102
7.10	Reconstructed TMPs of the normal and obese diabetic subjects . . . . .	103
7.11	BSP SD of the normal and obese diabetic subjects . . . . .	104
7.12	BSP PSD of the normal and obese diabetic subjects . . . . .	104
7.13	BSP PCA of the normal and obese diabetic subjects . . . . .	105
7.14	QTc intervals of the normal and obese diabetic subjects . . . . .	106
A.1	A snap shot of ECGSIM interface . . . . .	113
A.2	Data exported from the ECGSIM platform . . . . .	114
C.1	ECGSIM torso and a realistic obese torso . . . . .	118
C.2	Interpolation operation based on normal and obese torso surface contours . . . . .	118
C.3	Obese torso model generated with the interpolated approach . . . . .	120
D.1	Ultrasonic measuring procedure . . . . .	122
D.2	Body surface potential measuring procedure . . . . .	123
D.3	Torso shape measuring procedure . . . . .	124

# Chapter 1

## Introduction

Risk for cardiovascular dysfunction, myocardial infarction (MI) and sudden cardiac death are markedly increased by diabetes. We hypothesize that deleterious electrical remodeling presumed to occur in the diabetic heart is a result of metabolic derangements in the myocyte, structural damage to the myocardium, or both. Furthermore, we believe this remodeling can be measured on the body surface and linked to underlying cardiac dysfunction. These electrical changes may presage mechanical, vascular, or electrical dysfunction or be additive to other biomarkers of cardiovascular risk.

Few studies have focused on electrical activity in the diabetic heart. Nevertheless, some standard electrocardiographic features have been found to be associated with diabetes specifically. Electrocardiographic studies of diabetes, however, may be complicated by accompanying obesity, which also carries risk for MI, heart failure, and cardiovascular disease [87]. According to the American Heart Association in 2004 obesity affected over 66 million adults while more than 15 million were diagnosed with Diabetes Mellitus. Based on statistical data from the Medical Expenditure Panel Survey-Household Component, approximately 79% of diabetics in America are extremely obese, obese, or overweight [101]. The long-term goal of this study is to characterize the cardiac electrical phenotype of both obesity and diabetes to improve our ability to predict risk for cardiac dysfunction associated with these conditions.

In obese subjects, geometrical changes produce differences in body-surface potentials (BSPs) compared to normal subjects. Changes include left ventricular hypertrophy (LVH), variation in heart position and orientation, and increased fat deposition in the abdomen. In diabetic patients, symptoms which may be associated with cardiac

electrical remodeling include derangement of metabolism and both glucose and insulin sensitivity. In several animal-based experiments, cardiac cell transmembrane potentials measured from diabetic animals differed from those in normal animals. Furthermore, these changes in transmembrane potentials were manifest in BSPs.

The goal of this work is to reveal the electrical phenotype of diabetes in body-surface ECGs in the presence of obesity. Research presented in each chapter of this dissertation contributes to the accomplishment of the goal. The electrical remodeling in diabetes that poses cardiovascular risk is expected to be seen in cardiac cellular transmembrane potentials (TMPs), as well as in BSPs. Along with it, key anatomical changes with obesity are also considered to affect BSPs. To study the disease associated electrical phenotypes, we develop a bidomain framework as the foundation of this research.

To achieve the overall goal, the following four modules will be embedded into the framework: 1) a *Bidomain Source Module*, to approximate the general waveform of cardiac cellular TMPs; 2) a *Bidomain Forward-Problem Module*, to estimate epicardium and BSPs from cardiac TMPs by solving the bidomain forward problem; 3) a *Cardio-myocyte transmembrane potential Estimation Module*, to estimate cardiac-surface TMPs from BSPs by solving inverse-problems; 4) a *Body Surface Potential Mapping Module*, to pre-process and calibrate body surface ECG measurements. In addition to these modules, two disease related remodelings will be interpreted and incorporated into the framework, as *Diabetic Heart TMP features* and *Obese Habitus features*. All the work is summarized in the following five specific aims:

**AIM 1. To construct a simulation platform to evaluate heart- and body-surface potentials from cellular level electrophysiological features.** Boundary-element biophysical models, with realistic torso geometry, will be based on a double-layer source model and the bidomain theorem. *This forward-problem platform is designed as a convenient and reliable tool for the current research on diabetes and obesity. It will also help identify electrical phenotypes of other conditions that cause cardiac dysfunction.* To determine the impact of TMP variations in diabetes on ECGs, BSPs will be calculated from cardiac TMPs and a description of torso volume conductors using bidomain forward problem model. The phenotypes of diabetes and obesity will be revealed by changes in spatial and temporal features of BSPs.

**AIM 2. To devise methods suitable for the boundary element method (BEM) bidomain inverse-problem in the clinical study.** New schemes for solution of the inverse-problem will, of course, rely on the forward-problem formulation developed in Aim 1. *With these schemes, we will not only study electrical remodeling in simulation, but will also determine cellular cardiac electrical features from body-surface measurement in normal and obese diabetic subjects.*

**AIM 3. To investigate the geometric influence of obesity on heart- and body- surface potentials.** Obesity causes dramatic variations in heart and torso anatomic structure, such as an increased thickness in the left ventricular wall, changes in the position and orientation of the heart, and an increase in abdominal fat volume. *Electrical changes that accompany variations in habitus will be determined by comparing heart- and body-surface potentials in obese heart and torso models to potentials in normal models with the same cardiac source description.*

**AIM 4. To evaluate the electrophysiological influence of diabetes on heart- and body- surface potentials.** Diabetes triggers changes in ion channel current densities and transmembrane potentials in cardiac cells. *Findings in diabetic animal studies will be used as the reference to approximate diabetic human myocyte transmembrane potentials. The resulting BSPs changes will be estimated with the bidomain forward problem module designed in Aim 1.*

**AIM 5. To estimate the electrophysiological influence of diabetes on heart- and body- surface potentials among normal, and obese diabetic subjects.** We collected electrical and geometrical measurements from one normal and one obese diabetic subjects. Given body surface ECG measurements, the heart surface myocyte transmembrane potentials are reconstructed with the bidomain inverse problem module designed in Aim 2. *By comparing heart- and body-surface potentials of normal and obese diabetic adult males, electrocardiographic variations that accompany cell-level changes will be determined. Differences discovered will serve as a foundation for future studies to identify effects of obesity and diabetes.*

To accomplish the above aims, we have made measurements of heart-torso geometries and BSPs from two subjects: one normal control and one obese diabetic. Also, we have exported simulation data of normal heart-torso geometry, BSPs, and a set



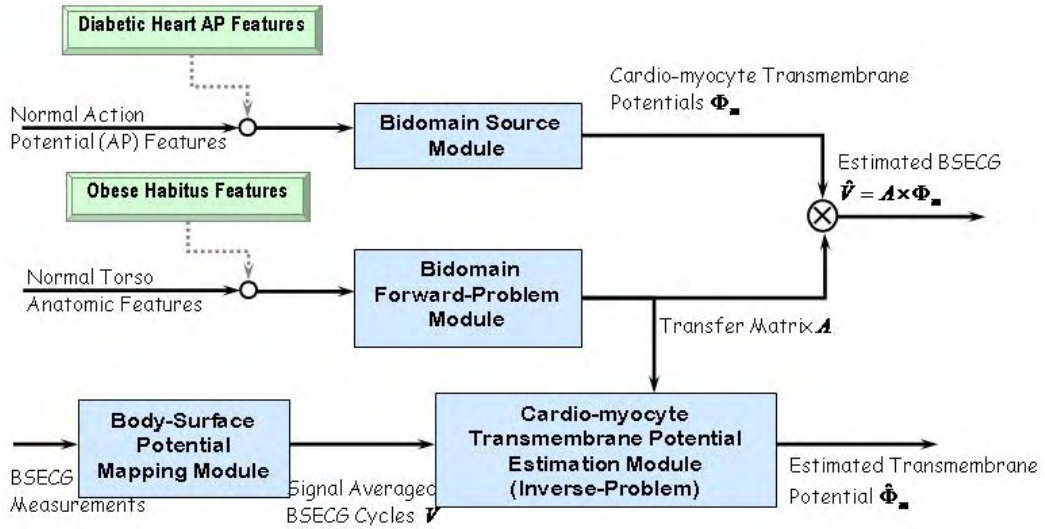


Figure 1.1: Bidomain ECG analysis platform is built to estimate heart and torso surface potentials based on the bidomain model.

of reference timing parameters of TMPs from the interactive simulation program ECGSIM (University of Nijmegen, the Netherlands. <http://www.ecgsim.org>).

As show in Figure 1.1, a framework is constructed to achieve aims of the study. It is composed of: a *Bidomain Forward-Problem Module*; a *Cardio-myocyte Transmembrane Potential Estimation Module* used to solve the forward- and inverse-problems; a *Bidomain Source Module* used to represent cardiac electrical activities with APs; and a *Body-Surface Potential Mapping Module* used to pre-process measured ECG signals. Diabetes related electrical remodeling and obesity-related geometrical remodeling are characterized and included in this platform. This pioneering work will help to identify electrical biomarkers for diabetes available in a clinical setting.

# Chapter 2

## Background

The motivation behind this work is to find out the electrical phenotype of diabetes from the measurable body surface electrocardiograms (ECGs). Diabetes Mellitus (DM) is one of the most prevalent and dangerous diseases in the United States. It increases the risk and mortality of heart diseases. The study is designed to understand the cardiac electrophysiological environment within diabetic patients, and identify the electrical phenotypes related to diabetes. The more we know about the diabetes phenotypes, the better we may understand the underlying link between diabetes and certain heart disease.

In this chapter, we review the effects of diabetes and obesity on ECGs. Obesity is a major compounding factor of diabetes. The approaches used to solve the ECG forward and inverse problem are also reviewed in this section. These approaches connect the potentials distributed over heart and body surfaces, from which the diabetes phenotypes are identified.

### 2.1 Effects of Diabetes and Obesity

In a technical report published by the World Health Organization (WHO), diabetes mellitus (DM) is defined as "a metabolic disorder of multiple aetiology characterized by chronic hyperglycaemia with disturbances of carbohydrate, fat and protein metabolism resulting from defects in insulin secretion, insulin action, or both" [2]. There are two types of diabetes: Type I and Type II diabetes. Type I diabetes (also

called insulin-dependent or immune-mediated diabetes) occurs when the body cannot produce insulin; most of Type I diabetes appears before the age of 18. Type II diabetes (also called non-insulin-dependent diabetes) occurs when the body can produce insulin, but it either does not produce enough or it cannot use it properly. About 90% of diabetics have Type II diabetes. Because of its prevalence and its role in cardiac dysfunction, this study will focus on the Type II diabetes, which will be referred to as just diabetes.

In 2004, more than 15 million people were diagnosed with DM and more than 72 thousand deaths have been reported because of it [87]. In addition, statistics show an increasing trend in the prevalence of DM. The Framingham study indicates a doubling in the incidence of diabetes over the past 30 years, with the most dramatic increase occurring during the 1990s [31]. From 1994 to 2002, the percentage of diabetic patients increased from 4.8 to 7.3 among adults in the United States[1].

Heart disease, stroke, and kidney disease are complications of diabetes. The effect of diabetes on the heart includes abnormalities in both structure and function [7, 58]. Furthermore, diabetes increases mortality and morbidity of heart disease [87, 79, 13, 76, 50, 117, 59]. More than 65% of diabetic patients die of some form of heart disease or stroke. The heart disease death rate among diabetic adults is two to four times higher than the rate of non-diabetic adults [87].

The Strong Heart Study among Native Americans showed that left ventricular hypertrophy (LVH) happens more frequently among diabetic patients than non-diabetic subjects, and that the average left ventricle (LV) mass is about 10% higher in diabetic patients than in glucose-tolerant subjects. Furthermore, the interventricular septal (IVS) wall and posterior wall were on average 3% ~ 5% thicker in the diabetic group [25, 79, 30]. This tendency for wall thickening is even more pronounced in obese diabetes.

### **2.1.1 Electrical Abnormalities due to Diabetes**

Although, diabetes is one major risk factor for cardiovascular disease, the prognostic value of the electrocardiogram (ECG) in diabetics has not been fully studied. In

the dissertation, I will focus on diabetic associated abnormalities in two important electrical characters: myocyte transmembrane potentials (TMPs) and body surface ECGs.

Diabetes is related with deviations in the ion channel current density. Several animal-based diabetic cardiomyopathy studies suggested diabetic animals tend to have different current densities in cardiac cells. Specifically, the decreases of potassium ( $K^+$ ) current densities ( $I_{to}$  and  $I_{ss}$ ) and the increase of calcium ( $Ca^{2+}$ ) current density ( $I_{Ca}$ ) were found in many diabetic animals [77, 21, 122, 14]. These diabetes-related current density variations can lead to prolongation of myocyte TMP duration [83, 27, 97, 78, 98].

Myocyte TMPs signal the depolarization and repolarization of the transmembrane potential of a cell. *In this study, TMPs are used to characterize cardiac sources.* The relationship between TMPs and body surface potentials (BSPs) can be explained with a bidomain mathematical model [100]. With the bidomain model, we can simulate the effect of diabetes on BSPs based on its effect on TMPs. This theory will be verified later with ECGs recorded from the diabetic subject.

Electrocardiographic features linked to diabetes, for the most part, come from studies of the conventional 12-lead ECG system. The 12-lead system consists of 8 electrode signals presented as 12 waveforms:  $V_I$ ,  $V_{II}$ ,  $V_{III}$ ,  $aV_R$ ,  $aV_L$ ,  $aV_F$ ,  $V_1$ ,  $V_2$ ,  $V_3$ ,  $V_4$ ,  $V_5$ ,  $V_6$  (see Figure 2.1). Among these leads, the first 2 represent electrical activity projected onto the frontal plane; while the 6 precordial leads represent activities projected onto the transverse plane [68].

The 12-lead ECG system provides a convenient way to characterize heart electrical activity. It has been employed to find risk indicators for cardiac dysfunction, CVD, and all-cause mortality among Type II diabetic patients [81, 80, 45, 39, 75, 93, 24, 113, 58]. Specifically, the following ECG features have been used to detect diabetes related heart problems: QT interval parameters (such as corrected QT interval (QTc), or QT dispersion (QTd)), ST segment depression (STD), and T wave alternans (TWA) [81, 75, 93, 24, 113, 22, 57, 74].

With the 12 lead system, we can estimate certain cardiac electrical activities from non-invasive measurements. The estimation is based on the assumption of a sphere

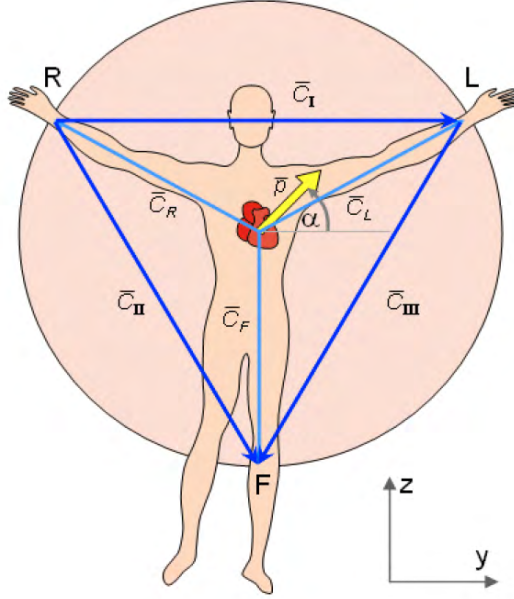


Figure 2.1: Limb-lead description of the 12-lead ECG system, from *Bioelectromagnetism* by Jaakko Malmivuo [68]

torso volume conductor, as shown in figure 2.1. The cardiac source is represented by a dipole  $\vec{p}$  located on the center of the great circle that is the frontal circumference of sphere conductor. Three limb leads ( $V_I$ ,  $V_{II}$ ,  $V_{III}$ ) are located on a inter-tangent equilateral triangle of the great circle. Limb leads are calculated from  $p$  and its angle  $\alpha$  as

$$V_I = p \cos \alpha \quad (2.1)$$

$$V_{II} = \frac{p}{2} \cos \alpha - \frac{\sqrt{3}}{2} p \sin \alpha \quad (2.2)$$

$$V_{III} = -\frac{p}{2} \cos \alpha - \frac{\sqrt{3}}{2} p \sin \alpha \quad (2.3)$$

Based on the above equations, the strength and angle of source dipole  $\vec{p}$  can be reconstructed from these limb leads [68].

As a matter of fact, the sphere volume assumption ignores the torso anatomic structure, and does not consider the great diversity in anatomy among different individuals, such as slim, normal, obese, and severely obese subjects. Therefore, it is hard

to evaluate specific anatomic effects based on 12-lead system. On the other hand, body-surface mapping uses a realistic torso model, provides a comprehensive view of cardiac activity with higher spatial resolution. Therefore, it may be more successful in identifying electrical characteristics of diabetes. A body-surface potential mapping (BSPM) system typically uses  $> 60$  electrodes to cover most of the torso surface, not just the limbs and the precordial region [72, 73, 62, 63]. Measurements from each electrode are registered to a common reference, such as the Wilson central terminal (WCT), a single site on the back, or on the left leg. *In this study, body-surface maps are used to study electrical remodeling in diabetic and obese subjects.*

### 2.1.2 Anatomical Abnormalities due to Obesity

Obesity is a main coherent factor of Type II diabetes and heart disease [39]. Based on definitions from the World Health Organization (WHO), subjects with a body mass index (BMI) of  $25\text{kg}/\text{m}^2$  or above are overweight, and with BMI of  $30\text{kg}/\text{m}^2$  or greater are obese [121]. In 2004, 140 million U.S. adults were diagnosed as overweight and 66 million were obese, which amounts to 66% and 31% of the population, respectively [87]. According to WHO, if current trends continue, the number of overweight and obese people worldwide will increase to 1.5 billion by 2015.

Several parameters have been employed to calibrate obesity status: 1) body mass index (BMI); 2) waist circumference (WC); 3) waist-to-hip ratio (WHR); 3) skinfold measurements with callipers; 4) dual wavelength X-ray absorption; and 5) percentage body fat [96]. BMI, WC and WHR are the most prevalent indicators, and may explain the correlation between obesity and its complications, including diabetes and heart disease [17, 56, 55, 43, 119]. Figure 2.2 shows that the relative risks of several diseases, including diabetes, are monotonically increased with higher BMI. The cutoff points of the disease risk for Type II diabetes, hypertension, and CVD in terms of BMI, WC and WHR are given in Table 2.1.

Many studies have shown that obesity is closely related to the changes in cardiac structure and function. In particular, obesity can cause left ventricular hypertrophy (LVH). Specifically, obese subjects tend to have, on average, 25 to 60% higher left ventricular (LV) mass; 15 to 25% thicker posterior wall thickness in diastole; (PWTd)

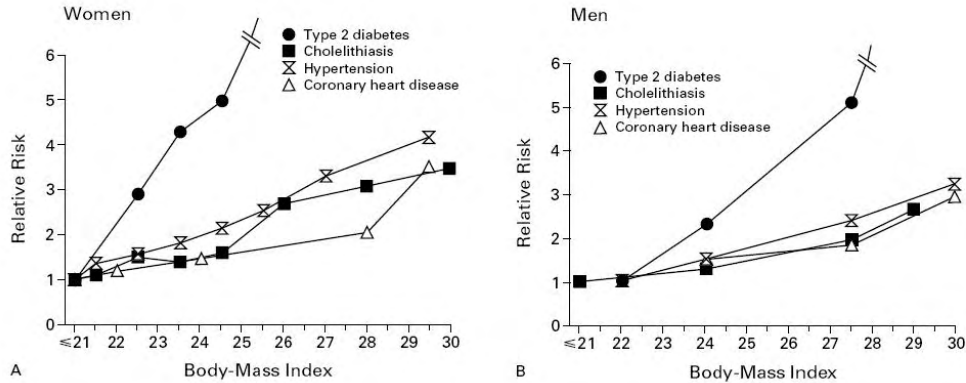


Figure 2.2: Relation between BMI and the Relative Risk of Type II Diabetes, Hypertension, Coronary Heart Disease, and Cholelithiasis (from Willett and coworkers [119].)

and the interventricular septum thickness in diastole (IVSd) [32, 84, 8, 120]. These changes are more dramatic in the severely obese group [8, 120], but can be reversed by weight loss [51, 67].

According to the National Heart Lung and Blood Institute (NHLBI), an increase in abdominal fat is associated with an increased risk for diabetes, cardiovascular disease (CVD) and hypertension, when BMI in the ranges of  $25 \sim 35$  [60]. People with an apple body shape (body fat stored around the abdomen, chest and surrounding internal organs) tend to have a higher risk of diabetes, heart disease and hypertension than people with a pear body shape (body fat stored on the hip and thigh areas) [20, 116, 42]. Because obese diabetics tend to be apple-shaped, in this study, we use Waist circumference (WC) to evaluate the degree of obesity and to separate normal from obese torsos. WC is an indicator of abdominal fat distribution, is also considered one of the important anthropometric measures for the risk of CVD [17].

## 2.2 Bidomain Forward and Inverse Problems

In the last section, we reviewed the electrical and anatomical abnormalities observed in past studies. In this section, we will briefly introduce the forward and inverse

Table 2.1: Disease Risk for Type II Diabetes, Hypertension, and CVD<sup>†</sup>

	Women	Men
BMI( $kg/m^2$ )	>30	>30
Waist Circumference (WC) (cm)	>88	>102
Waist/Hip Ratio (WHR) (%)	>80	>95

<sup>†</sup>from the guidelines on overweight and obesity published by National Heart Lung and Blood Institute[60]

approaches used to link heart TMPs and body surface ECGs. With these approaches, the underlying electrical and anatomical causes can be connected to the observed abnormal ECG patterns.

### 2.2.1 Forward Problem

Generally, the forward problem of the electrocardiogram (ECG) is formulated to determine BSPs for given cardiac sources inside the volume-conductor models. Approaches used in solving the forward problem fall into two categories: surface methods and volume methods [40, 90]. In surface methods, the volume outside the source is decomposed into isotropic conductivity regions separated by interface boundaries. Surface forward problem methods are built on the analysis of these interfaces; therefore, they are also termed boundary-element methods (BEM). Volume methods include finite-difference method (FDM) and finite-element methods (FEM). In volume methods, the entire 3-D torso model is numerically represented by a combination of elements with a certain shape. Volume methods can incorporate conductivity variation in high resolution, but they require more complex representation of the torso model. In this study, we chose surface methods because they require a relatively simple torso model, more suitable for clinical research.

Typically, the forward problem takes two inputs, source and volume conductor. The general BEM source models include: *dipole*, *multipole*, *distributed dipole* and *epicardial potentials* [68]. Among them, the dipole model represents a single current vector with a certain orientation, magnitude and location. Just as the dipole is formed from two equal and opposite monopoles, a multipole source is formed with two or more pairs of



equal opposite monopoles that are close together. What is important about multipoles is that it can be shown that any given source configuration can be expressed as an infinite sum of multipoles of increasing order (i.e., dipole, quadrupole, octapole, etc.). The distribute dipole source is composed of a set of dipoles located over a certain anatomical region of the heart. The double-layer is one form of distribute dipole source, when dipoles are uniformly distributed over a surface with enough density so that the distribution of dipoles can be well approximated with a continuous function. Epicardial potentials represent the potentials measured outside the heart surface. *In this study, we use the double-layer source model to present heart surface myocyte transmembrane potentials (TMPs).*

As the second input for the forward problem, the volume conductor can be classified based on whether it is finite or infinite, homogeneous or inhomogeneous. In this study, we solve the forward problem based on a double-layer source located in a finite realistic inhomogeneous volume conductor, in which internal in-homogeneities include heart muscle, lungs, and blood masses. As a volume conductor, the anatomy of the heart and torso is an important contributor to the body surface ECG patterns among obese diabetes. With this model, we can quantify the anatomic effects on BSPs in an obese diabetic heart.

After choosing BEM to formulate the forward problem, we use the bidomain model to incorporate myocyte transmembrane potentials (TMPs) as the double-layer source. The bidomain model describes electrophysiological behavior based on discrete cell structure. In this model, the tissue space is classified into intra- and extra-cellular domains. The current passes from one domain to another, through the cell membrane [68, 105, 36]. Similar applications appeared in several other studies [100, 36, 28, 107]. Among them, Fischer and Tilg combined FEM and BEM bidomain models. In their work, an FEM bidomain model was applied to the myocardium inside the heart, while a BEM bidomain formulation was adopted in the volume conductor outside the heart [28]. *In this study, we use the BEM bidomain model described by Geselowitz and coworkers, in which BSPs are estimated from heart-surface TMPs and the heart-torso anatomical structure [100, 36, 34].*

## 2.2.2 Inverse Problem

The reconstruction of the heart bioelectrical features has significant clinical impact. By solving the inverse problem, the heart electrical activities can be reconstructed non-invasively. This technique can be used to locate disease associated abnormalities, such as myocardial infarction (MI), ischemia, pre-arrhythmic events, and accessory pathway in Wolf-Parkinson-White(WPW) syndrome [11]. Additionally, some recent studies indicate diabetes and long QT (LQT) syndrome are associated with a deviation of cardiac myocyte transmembrane potentials (TMPs) [124, 52, 21, 122]. Here, TMP is defined as the difference between intra- and extra-cellular potentials. It represents basic heart bioelectrical activities on the cellular level. Later in this paper, TMP will play the role of the cardiac source in both forward and inverse problems.

It is well known that the ECG inverse-problem is an ill-conditioned problem, i.e. the transfer matrix solved by the forward problem has an extremely high condition number. Even small fluctuations in measured BSPs could lead to drastic deviations in estimated results of TMPs. To solve this problem, a regularization process has been introduced to smooth or to set bounds on the inverse problem solution. In previous ECG inverse problem studies, regularization techniques have been widely used. They include Tikhonov regularization (considering amplitude or spatial constraints)[69, 90]; truncated singular value decomposition (TSVD)[95, 44, 47]; Twomey regularization (considering temporal constraints)[69, 82]; and multiple constraint methods [15, 16, 66]. This study selects two well-developed regularization approaches, TSVD and zero-order Tikhonov, to handle the ill-conditioned situation.

Considering the property of the source model, the bidomain inverse problem is a rank-deficient problem, i.e. transfer matrix is not a numerically full-rank matrix[44]. Then, based on the forward problem solution, there will be infinite estimations for source TMPs. Among them, regularization results are just approximations, which do not match the basic characters of TMP waveform. In this study, we used the nature of TMP waveform as prior information to adjust regularization outputs to the 'ideal' estimation of source potentials.

Several previous studies have been focused on reconstructing features or segments of myocyte TMPs from body surface potentials (BSPs) [103, 70, 107, 106, 110]. In these

studies, Messnarz and Tilg used a spatiotemporal regularization approach to calculate activation time (AT) imaging and potentials during depolarization [103, 70]. van Oosterom and coworkers introduced fixed waveform and optimization methods to estimate timing parameters and potentials during repolarization and depolarization [107, 106, 47]. Nevertheless, insufficient accuracy and noise sensitivity are still the problems that have not been fully resolved. This study develops an innovative inverse calculation, which achieves relatively high accuracy, and acts less sensitive to measurement noise, without increasing the computational complexity.

In this chapter, we reviewed electrical and geometrical abnormalities related to diabetes and obesity. In the following sections, these abnormalities are used to identify the diabetes phenotypes in the presence of obesity. In addition, we also introduced the bidomain forward and inverse problem approaches, which are used to connect an electrical pattern over heart and body surfaces.

# Chapter 3

## Bidomain Forward Problem

The goal of this work was to characterize the electrical phenotypes of diabetes in the presence of obesity. Based on available knowledge on diabetic electrophysiology, two electrical phenotypes are considered to be related to diabetes: 1) cardio-myocyte transmembrane potentials (TMPs), and 2) body surface potentials (BSPs). The former parameter is a cellular-level electrical feature commonly studied in diabetic electrophysiologic research; the latter represents the electrical potential distribution over body surface, which can be recorded during a clinical procedure. These are not independent features: myocyte TMPs are considered as electrical generators, and BSPs are the corresponding observations on the body surface. To systematically investigate the diabetic effects on the torso electrical environment, we need to link the electrophysiology findings of diabetic research to clinical ECG observations. In this study, we connect myocyte TMPs with BSPs through the bidomain forward problem model.

The forward problem of electrocardiography is formulated to calculate BSPs from the heart electrical activities, as influenced by the torso volume conductor. By employing the bidomain model, myocyte TMPs are incorporated into the forward problem formulation as a double-layer source. The volume conductor is represented with a set of boundaries surrounding different torso homogeneous regions. These boundaries' geometries and the conductivities within them were used to estimate the transfer matrix  $\mathbf{A}$ , which links BSPs to TMPs. Based on the representations of source and volume conductor, we call this formulation the bidomain double-layer, forward problem.

The Algorithms developed to solve the bidomain double-layer forward-problem were developed in the Matlab<sup>®</sup> (Mathworks, Inc., Natick, MA) environment, and assembled as a *bidomain forward-problem Module*. This module takes torso anatomy, including organ geometries and conductivities, as inputs. Its output is the transfer matrix  $\mathbf{A}$ . BSPs were estimated by multiplying  $\mathbf{A}$  by the source TMPs. In addition, the inverse problem was formulated using  $\mathbf{A}$ , the solution of the forward problem.

In this chapter, the representation of myocyte TMPs is introduced first. Based on this representation, the bidomain double-layer, forward-problem approach is derived in detail. Finally, the forward-problem solution was carefully verified.

## 3.1 Myocyte Transmembrane Potential (TMP)

Ventricular myocyte electrical activities are responsible for BSPs during segments of QRS-complex and T wave, where most of diabetes related ECG features were found. Therefore, ventricular myocyte TMPs were selected as the electrical source in our forward-problem formulation. In this section, we explain what TMP is, and how to represent it.

### 3.1.1 Biophysical Context of Transmembrane Potential

Transmembrane potential is also called the action potential when it reaches a certain threshold. TMP is defined as the difference between intracellular  $\phi_i$  and extracellular potentials  $\phi_o$ , as

$$\phi_m = \phi_i - \phi_o \quad , \quad (3.1)$$

in which,  $\phi_m$  will be used as the symbol of myocyte TMP.

Figure 3.1 demonstrates a typical waveform of ventricular myocyte TMP. It can be divided roughly into five phases. They are: 0) depolarization, 1) notch, 2) plateau, 3) repolarization, and 4) resting phases [52]. These phases are caused by movements of sodium, calcium, potassium and chlorine ions. Specifically, during the depolarization phase, voltage-gated fast sodium channels open, a rapid influx of positive sodium ions

produces the inward sodium current  $I_{Na}$ , which leads to a dramatic jump in membrane potential. The notch phase starts when the fast sodium channel fails to be active. The major ion channels at this state are  $K^+$  and  $Cl^-$ , and the outward potassium current density  $I_{to}$  is responsible for the notch in ventricular myocyte TMPs.

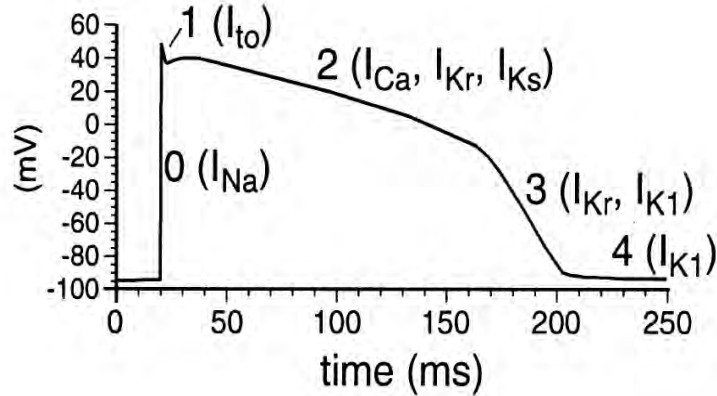


Figure 3.1: Schematic representation of the cardiac transmembrane potential. It is composed with five phases: 0) depolarization, 1) notch, 2) plateau, 3) repolarization, and 4) resting. From Keating and Sanguinetti [52].

During the plateau stage, the calcium ion  $Ca^{2+}$  influx  $I_{Ca}$  and the  $K^+$  efflux  $I_{Ks}$  remain in balance. As a result, the overall membrane potential remains roughly unchanged. In the repolarization phase, the  $Ca^{2+}$  channels close while the  $K^+$  channels remain open, and the outward currents  $I_{Kr}$  and  $I_{K1}$  persist. The TMP keeps falling until it reaches the resting potential. Typical myocyte resting potential is around  $-90mV$ . During the resting phase, the net movement of sodium  $Na^+$  into the cell equals the net movement of potassium  $K^+$  out of the cell, i.e., the net current is zero. The duration of repolarization is approximately 100 msec. The amplitude of the TMP is about 100 mV for both muscle and nerve cells [68].

## 3.2 Bidomain Double-layer Forward Problem

The ECG forward problem is used to estimate body surface potentials (BSPs) from heart electrical activities and the torso volume conductor. In the previous section,

heart electrical activities were expressed as myocyte TMPs. In this section, heart-torso geometries and conductivities are incorporated into the forward problem formulation to generate  $\mathbf{A}$ , which is the transfer matrix from source TMPs to BSPs.

The methods used to solve the forward problem can be classified into two groups: boundary element methods (BEM) and volume methods. Here, we choose BEM, because BEM require a relatively simple description of the torso geometry, suitable for clinical studies. In BEM, the inhomogeneous volume conductor is decomposed into homogeneous regions surrounded by closed boundaries, which will be discretized and represented in the forward problem formulation. Potentials over these boundaries (including BSPs) will be estimated from the output of the forward problem.

Tissue capacitance is negligible within the frequency band of heart electrical activity [37]. Thus, this electromagnetic problem is quasi-static, which means the electric and magnetic fields are decoupled, and the forward and inverse-problems can be solved at each instant of time without considering previous conditions [36].

In BEM, boundary potentials  $\mathbf{V}$  are composed of two terms, primary-source potentials and secondary-source potentials. The primary-source potentials are potentials produced by the cardiac sources in a infinite homogeneous volume. The secondary-source potentials are potentials reflected by boundaries.

The general form of BEM for forward problem is:

$$\begin{aligned}
 V(r) &= \frac{1}{2\pi(\sigma_r^- + \sigma_r^+)} \int_v \mathbf{J}^i \cdot \nabla \left( \frac{1}{r} \right) dv \\
 &- \sum_{s=1, s \neq r}^m \frac{(\sigma_s^- - \sigma_s^+)}{2\pi(\sigma_r^- + \sigma_r^+)} \int_{S_s} V(r') \nabla \left( \frac{1}{r'} \right) \cdot dS,
 \end{aligned} \tag{3.2}$$

in which the first term on the right side is the primary source potential, and the second term represents the secondary source potential [41]. By adding them together, we obtain a boundary potential  $V(r)$ , where  $r$  is the vector from observation to source element of integration  $dv$ , and  $r'$  presents the vector from observation to reflecting boundary element  $dS$ . Conductivities,  $\sigma_s^-$  and  $\sigma_s^+$  represent values inside and outside

the source boundary; while  $\sigma_r^-$  and  $\sigma_r^+$  represent values inside and outside the observation boundary, respectively. In equation (3.3),  $\mathbf{J}^i$  is the impressed current density, which is used to describe ion movements driven by metabolic activities.

### 3.2.1 Bidomain Source Model

Rather than using cell transmembrane potential  $\Phi_m$ , the BEM form in equation (3.3) employs the impressed current density  $\mathbf{J}^i$  to represent the primary source. Therefore, to incorporate diabetes-effected  $\Phi_m$ , we need to use the bidomain model to explain the relation between  $\Phi_m$  and  $\mathbf{J}^i$ . To understand how it works requires a knowledge of some of the physical features of current density.

The overall current density,  $\mathbf{J}$  is the summation of the impressed current density  $\mathbf{J}^i$  and conduction current density. The conduction current density is proportional to the negative of the gradient of the electric scalar potential  $\Phi$  [36].

$$\nabla \cdot \mathbf{J} = \nabla \cdot \mathbf{J}^i - \nabla \cdot \sigma \nabla \Phi \quad . \quad (3.3)$$

We assume that the currents in the volume conductors are stationary, i.e., that there is not an accumulation of charge outside source. In this case, the divergence of the total current density is zero.

$$\nabla \cdot \mathbf{J} = 0 \quad . \quad (3.4)$$

Based on Equation (3.3) and (3.4), we get

$$\nabla \cdot \mathbf{J}^i = \nabla \cdot \sigma \nabla \Phi \quad . \quad (3.5)$$

In the bidomain model, the microscopic space is broken into intracellular and extracellular regions, which are separated by cell membrane. Based on this structure, the current densities in these two regions are expressed as:

$$\mathbf{J}_i = -\sigma_i \nabla \Phi_i \quad (3.6)$$

$$\mathbf{J}_o = -\sigma_o \nabla \Phi_o \quad , \quad (3.7)$$



where subscripts  $i$  and  $o$  represent intracellular and extracellular region respectively [36].  $\sigma_i$  and  $\sigma_o$  are conductivities, and  $\Phi_i$  and  $\Phi_o$  are potentials in these regions.

The transmembrane potential, or so called the action potential (AP),  $\Phi_m$  is defined as difference between  $\Phi_i$  and  $\Phi_o$ , as shown in Equation (3.1). The overall current density,  $\mathbf{J}$  in Equation (3.3) can also be expressed as the summation of  $\mathbf{J}_i$  and  $\mathbf{J}_o$ , then

$$\mathbf{J} = \mathbf{J}_i + \mathbf{J}_o \quad (3.8)$$

$$= -\sigma_i \nabla \Phi_i - \sigma_o \nabla \Phi_o \quad (3.9)$$

$$= -\sigma_i \nabla \Phi_m - \sigma_i \nabla \Phi_o - \sigma_o \nabla \Phi_o \quad (3.10)$$

$$= -\sigma_i \nabla \Phi_m - \sigma_H \nabla \Phi_o \quad (3.11)$$

For stationary volume conductors, based on Equation (3.4),

$$\nabla \cdot \sigma_i \Phi_m = -\nabla \cdot \sigma_H \Phi_o \quad (3.12)$$

where  $\sigma_H = \sigma_i + \sigma_o$  is the bulk conductivity that can be taken as the average conductivity of heart muscle. In the volume conductor close to the heart surface the scalar potential  $\Phi$  in Equation (3.5) is equal to the extracellular potential  $\Phi_o$ , and  $\sigma$  in Equation (3.5) becomes  $\sigma_H$ . By combining Equation (3.5) and (3.12), we get

$$\mathbf{J}^i = -\sigma_i \nabla \Phi_m \quad (3.13)$$

in which,  $\mathbf{J}^i$  is proportional to the gradient of myocyte TMP  $\Phi_m$ . Equation (3.13) enables us to bring  $\Phi_m$  into the forward problem equation, and estimate the resulting boundary potentials, such as BSPs. Then, the TMP variance due to diabetes will lead to certain changes in BSPs. By analyzing these changes, we can have a better understanding of the electrophysiologic effects of diabetes.

### 3.2.2 Bidomain Double-layer Forward Problem Model

In the previous section, the impressed current density  $\mathbf{J}^i$  in Equation (3.3) was derived as a function of the myocyte TMP  $\Phi_m$ . By substituting Equation (3.13) into (3.3),

we then get

$$\begin{aligned}
V(r) &= -\frac{1}{2\pi(\sigma_r^- + \sigma_r^+)} \int_v \sigma_i \nabla \Phi_m \cdot \nabla \left( \frac{1}{r} \right) dv \\
&\quad - \sum_{s=1, s \neq r}^m \frac{(\sigma_s^- - \sigma_s^+)}{2\pi(\sigma_r^- + \sigma_r^+)} \int_{S_s} V(r') \nabla \left( \frac{1}{r'} \right) \cdot dS,
\end{aligned} \tag{3.14}$$

Based on the rule of integration by parts, the first integration term in Equation (3.15) can be written as:

$$\begin{aligned}
-\int_v \sigma_i \nabla \Phi_m \cdot \nabla \left( \frac{1}{r'} \right) dv &= -\int_v \nabla \cdot (\sigma_i \Phi_m \nabla \left( \frac{1}{r'} \right)) dv \\
&\quad + \int_v \Phi_m \nabla \cdot (\sigma_i \nabla \left( \frac{1}{r'} \right)) dv \quad .
\end{aligned} \tag{3.15}$$

In the above equation,  $\sigma_i \nabla \left( \frac{1}{r'} \right)$  represents lead field current, whose divergence will vanish outside the source [36]. Therefore, the second term on the right side equals zero. By applying the divergence theorem, the first term on the right side can be written in the form of a surface integral over heart surface  $S_H$ :

$$\begin{aligned}
-\int_v \sigma_i \nabla \Phi_m \cdot \nabla \left( \frac{1}{r'} \right) dv &= -\int_v \nabla \cdot (\sigma_i \Phi_m \nabla \left( \frac{1}{r'} \right)) dv \\
&= -\int_{S_H} \sigma_i \Phi_m \nabla \left( \frac{1}{r'} \right) \cdot dS_H
\end{aligned} \tag{3.16}$$

By substituting the above expression into Equation (3.15), the bidomain forward-problem becomes

$$\begin{aligned}
V(r) &= -\frac{1}{2\pi(\sigma_r^- + \sigma_r^+)} \int \sigma_h \Phi_m \nabla \left( \frac{1}{r} \right) \cdot dS_H \\
&\quad - \sum_{s=1, s \neq r}^m \frac{\sigma_s^- - \sigma_s^+}{2\pi(\sigma_r^- + \sigma_r^+)} \int_{S_s} V(r') \nabla \left( \frac{1}{r'} \right) \cdot dS \quad .
\end{aligned} \tag{3.17}$$

To implement Equation (3.17) numerically, we use a set of triangular surface elements  $\triangle$  to approximate smooth boundaries in 3-D. Additionally, a solid angle expression is introduced to represent a source surface projection onto the unit sphere centered at the observation location. For example, the solid angle subtended by source triangle

$\Delta_j$  at observation point  $i$  is  $\Omega_{ji}$  [41], whose derivative becomes:

$$d\Omega_{ji} = \nabla \left( \frac{1}{r'} \right) \cdot dS_j \quad (3.18)$$

Then, Equation (3.17) becomes

$$V_i = -\frac{1}{2\pi(\sigma_r^- + \sigma_r^+)} \int \sigma_h \Phi_m \, d\Omega_{Hi} - \sum_{s=1, s \neq r}^m \frac{\sigma_s^- - \sigma_s^+}{2\pi(\sigma_r^- + \sigma_r^+)} \int_{\Delta_j} V_j \, d\Omega_{ji} \quad (3.19)$$

In matrix notation, the discretized version of Equation (3.19) is

$$\begin{aligned} \begin{bmatrix} V_t \\ V_h \\ V_l \end{bmatrix} &= -\frac{1}{2\pi} \begin{bmatrix} \frac{\sigma_h \Omega_{th}}{\sigma_t} \\ \frac{\sigma_h \Omega_{hh}}{\sigma_h + \sigma_t} \\ \frac{\sigma_h \Omega_{lh}}{\sigma_l + \sigma_t} \end{bmatrix} [\Phi_m] - \frac{1}{2\pi} \begin{bmatrix} \Omega_{tt} & \frac{(\sigma_h - \sigma_t) \Omega_{th}}{\sigma_t} & \frac{(\sigma_l - \sigma_t) \Omega_{tl}}{\sigma_t} \\ \frac{\sigma_t \Omega_{ht}}{\sigma_h + \sigma_t} & \frac{(\sigma_h - \sigma_t) \Omega_{hh}}{\sigma_h + \sigma_t} & \frac{(\sigma_l - \sigma_t) \Omega_{hl}}{\sigma_h + \sigma_t} \\ \frac{\sigma_t \Omega_{lt}}{\sigma_l + \sigma_t} & \frac{(\sigma_h - \sigma_t) \Omega_{lh}}{\sigma_l + \sigma_t} & \frac{(\sigma_l - \sigma_t) \Omega_{ll}}{\sigma_l + \sigma_t} \end{bmatrix} \begin{bmatrix} V_t \\ V_h \\ V_l \end{bmatrix} \\ &= -\frac{1}{2\pi} \begin{bmatrix} \frac{\sigma_h}{\sigma_t} \\ \frac{\sigma_h}{\sigma_h + \sigma_t} \\ \frac{\sigma_h}{\sigma_l + \sigma_t} \end{bmatrix} \bullet \begin{bmatrix} \Omega_{th} \\ \Omega_{hh} \\ \Omega_{lh} \end{bmatrix} [\Phi_m] \\ &\quad - \frac{1}{2\pi} \begin{bmatrix} 1 & \frac{\sigma_h - \sigma_t}{\sigma_t} & \frac{\sigma_l - \sigma_t}{\sigma_t} \\ \frac{\sigma_t}{\sigma_h + \sigma_t} & \frac{\sigma_h - \sigma_t}{\sigma_h + \sigma_t} & \frac{\sigma_l - \sigma_t}{\sigma_h + \sigma_t} \\ \frac{\sigma_t}{\sigma_l + \sigma_t} & \frac{\sigma_h - \sigma_t}{\sigma_l + \sigma_t} & \frac{\sigma_l - \sigma_t}{\sigma_l + \sigma_t} \end{bmatrix} \bullet \begin{bmatrix} \Omega_{tt} & \Omega_{th} & \Omega_{tl} \\ \Omega_{ht} & \Omega_{hh} & \Omega_{hl} \\ \Omega_{lt} & \Omega_{lh} & \Omega_{ll} \end{bmatrix} \begin{bmatrix} V_t \\ V_h \\ V_l \end{bmatrix} \end{aligned} \quad (3.20)$$

where  $\bullet$  indicates array multiplication.

In the above equation,  $V_t$ ,  $V_h$  and  $V_l$  represent potentials on three closed surfaces (the boundaries surrounding torso, heart, and lung). The conductivities inside these surfaces are  $\sigma_t$ ,  $\sigma_h$ , and  $\sigma_l$ . More inhomogeneities can be easily imported into Equation (3.20), by adding additional rows and columns into solid angle matrices, without affecting existing solid angles.

To simplify the expression of Equation (3.20), we make

$$\mathbf{B} = -\frac{1}{2\pi} \begin{bmatrix} 1 & \frac{\sigma_h - \sigma_t}{\sigma_t} & \frac{\sigma_l - \sigma_t}{\sigma_t} \\ \frac{\sigma_t}{\sigma_h + \sigma_t} & \frac{\sigma_h - \sigma_t}{\sigma_h + \sigma_t} & \frac{\sigma_l - \sigma_t}{\sigma_h + \sigma_t} \\ \frac{\sigma_t}{\sigma_l + \sigma_t} & \frac{\sigma_h - \sigma_t}{\sigma_l + \sigma_t} & \frac{\sigma_l - \sigma_t}{\sigma_l + \sigma_t} \end{bmatrix} \bullet \begin{bmatrix} \Omega_{tt} & \Omega_{th} & \Omega_{tl} \\ \Omega_{ht} & \Omega_{hh} & \Omega_{hl} \\ \Omega_{lt} & \Omega_{lh} & \Omega_{ll} \end{bmatrix} \quad (3.21)$$

Then, Equation (3.20) becomes

$$\begin{bmatrix} V_t \\ V_h \\ V_l \end{bmatrix} = -\frac{1}{2\pi} \begin{bmatrix} \frac{\sigma_h \Omega_{th}}{\sigma_t} \\ \frac{\sigma_h \Omega_{hh}}{\sigma_h + \sigma_t} \\ \frac{\sigma_h \Omega_{lh}}{\sigma_l + \sigma_t} \end{bmatrix} [\Phi_m] + \mathbf{B} \begin{bmatrix} V_t \\ V_h \\ V_l \end{bmatrix} . \quad (3.22)$$

In this equation, by moving the second term on the right to the left side, we get

$$(\mathbf{I} - \mathbf{B}) \begin{bmatrix} V_t \\ V_h \\ V_l \end{bmatrix} = -\frac{1}{2\pi} \begin{bmatrix} \frac{\sigma_h \Omega_{th}}{\sigma_t} \\ \frac{\sigma_h \Omega_{hh}}{\sigma_h + \sigma_t} \\ \frac{\sigma_h \Omega_{lh}}{\sigma_l + \sigma_t} \end{bmatrix} [\Phi_m] , \quad (3.23)$$

where,  $\mathbf{I}$  is the identity matrix sharing the same size with  $\mathbf{B}$ .

It seems that surface potentials  $V_t$ ,  $V_h$  and  $V_l$  can be estimated by multiplying the inverse of  $(\mathbf{I} - \mathbf{B})$  to the primary source potentials in Equation (3.23). Based on the definition of the solid angle, however, the summation of each row of matrix  $\mathbf{B}$  equals one, i.e. it has a unit eigenvalue. Consequently,  $(\mathbf{I} - \mathbf{B})$  will have a zero eigenvalue. It is inappropriate to invert this matrix because it is singular. In this study, we used multiple deflations to solve this problem. The deflated matrix  $\mathbf{C}$  will be used to replace  $\mathbf{B}$  in Equation (3.23). For implementation details of deflation, see Appendix B. After deflation, surface potentials can be calculated with the following equation:

$$\begin{bmatrix} V_t \\ V_h \\ V_l \end{bmatrix} = -\frac{1}{2\pi} (\mathbf{I} - \mathbf{C})^{-1} \begin{bmatrix} \frac{\sigma_h \Omega_{th}}{\sigma_t} \\ \frac{\sigma_h \Omega_{hh}}{\sigma_h + \sigma_t} \\ \frac{\sigma_h \Omega_{lh}}{\sigma_l + \sigma_t} \end{bmatrix} [\Phi_m] . \quad (3.24)$$

With transfer matrix  $\mathbf{A}$  as

$$\mathbf{A} = -\frac{1}{2\pi} (\mathbf{I} - \mathbf{C})^{-1} \begin{bmatrix} \frac{\sigma_h \Omega_{th}}{\sigma_t} \\ \frac{\sigma_h \Omega_{hh}}{\sigma_h + \sigma_t} \\ \frac{\sigma_h \Omega_{lh}}{\sigma_l + \sigma_t} \end{bmatrix} , \quad (3.25)$$

the bidomain forward-problem solution becomes

$$\mathbf{V} = \mathbf{A} \Phi_m . \quad (3.26)$$

In this work, Equation (3.24) is implemented in the *Bidomain Forward-Problem Module*. Transfer matrix  $\mathbf{A}$  is the output of our forward-problem module. It contains all applicable anatomical information (geometries and conductivities) of the torso. By multiplying  $\mathbf{A}$  by the myocyte TMPs  $\Phi_m$ , we find the potentials on the body, heart or other organ surfaces. Furthermore, equation (3.26) can be used to estimate  $\Phi_m$  from the observed body surface potentials by solving the inverse-problem. For details of the inverse operation, see Chapter 4.

### 3.3 Bidomain Forward Problem Numerical Implementation

#### 3.3.1 Numerical Representation of Transmembrane Potentials

Two methods are typically used to construct a TMP: 1) characterization based based on its biophysical model [61, 92, 48]; and 2) characterization from a parameterized function [71, 35, 109, 103, 26, 106, 110]. In this study, the latter approach was used due to its simplicity. During the implementation, this approach was broken into two steps: 1) characterize the general shape of TMP waveform with a template that is represented with parameterized functions, and 2) find the corresponding function parameters for each spatial location on the heart. This portion of work was implemented in the *Bidomain Source Module*, as shown in Figure 1.1.

#### Transmembrane Potential (TMP) Template

In previous studies, several functions and their combinations have been used to generate the TMP template. The depolarization waveform has been approximated with a step function from  $-90mV$  to  $10mV$  [71], a ramp function [109], or an inverse tangent function [103]. The repolarization waveform of  $\phi_m$  has been approximated with six linear segments [71], an exponential function [26, 110], and an integral of dominant T wave [106]. The notch of  $\phi_m$  has been approximated from logistic function [110].

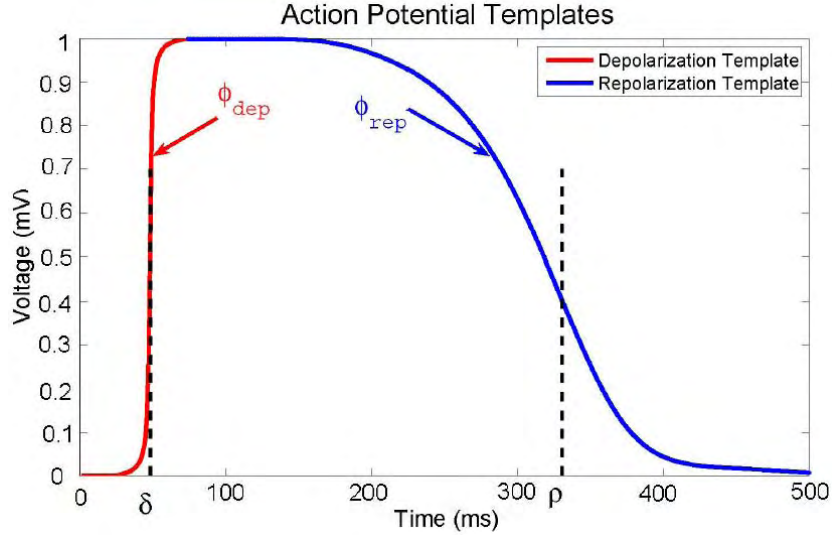


Figure 3.2: Transmembrane potential template composed of depolarization and repolarization waveforms. Parameters  $\delta$  and  $\rho$  identify the time instants when the steepest potential increase and decrease occur in the depolarization and the repolarization phase.

The shape and coordinates of these functions has been controlled by several parameters. For example, depolarization and repolarization timing variables have been used to indicate the instants when depolarization and repolarization occur [106, 103, 35]. These variables may vary from location to location over the heart surface. They can be estimated from body surface ECGs by solving the inverse problem.

A TMP template,  $\phi_m$ , was constructed for this study as shown in Figure 3.2. This template is composed of two segments, as  $\phi_m = [\phi_{dep}, \phi_{rep}]$ . Here,  $\phi_{dep}$  represents TMP during the depolarization phase. The template mainly decides BSPs during the QRS complex.  $\phi_{rep}$  presents TMP during the plateau, repolarization and part of resting phases (TMP notch waveform is ignored for now), and it contributes to BSPs during the ST segment and T wave. Similar approaches have been used by van Oosterom [107].

Based on its waveform,  $\phi_{dep}$  was characterized with an inverse tangent function

$$\phi_{dep}(t; k, \delta) = \left(\frac{2}{\pi}\right) \arctan(k(t - \delta)) \quad , \quad (3.27)$$

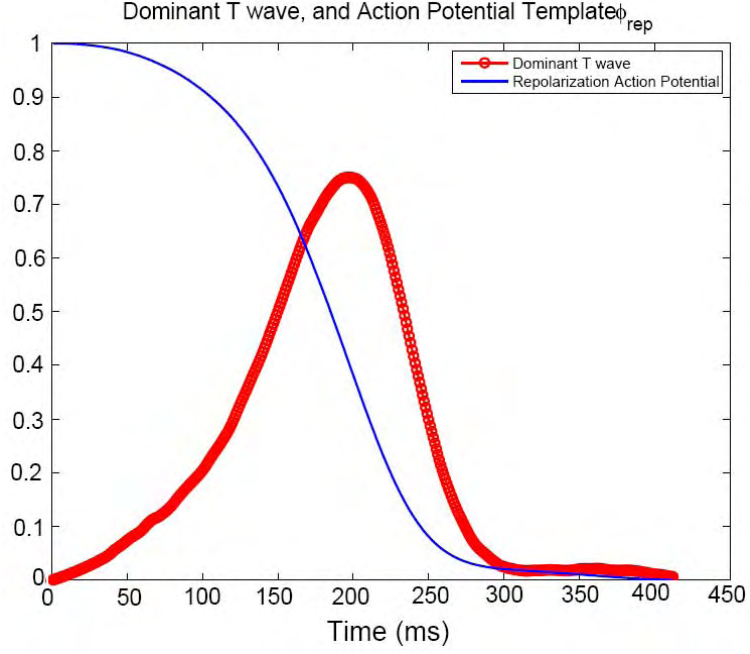


Figure 3.3: Dominant T wave and the transmembrane potential repolarization template.

where  $t$  indicates time instant,  $k$  is the parameter controlling the depolarization curve shape, and  $\delta$  is called depolarization timing, which is the time instant corresponding to the maximum TMP gradient.

$\phi_{rep}$  was generated by the integrating the dominant T wave [106]:

$$\phi_{rep}(t; \rho) \propto - \int (T_{dom}(t - \rho)) dt \quad , \quad (3.28)$$

where  $\rho$  is the depolarization timing, which is the time instant corresponding to the minimum gradient of transmembrane potential during  $\phi_{rep}$ . By combining  $\phi_{dep}(t; \delta)$  and  $\phi_{rep}(t; \rho)$ , we get the overall ventricular transmembrane potential template  $\phi_m(t; k, \delta, \rho)$ , as shown in Figure 3.2.

The dominant T wave function  $T_{dom}()$  is defined as the negative of the spatial derivative of the repolarization potential  $\phi_{rep}$ .

$$T_{dom}(t) = -\phi'_{rep}(t - \bar{\rho}) \quad , \quad (3.29)$$

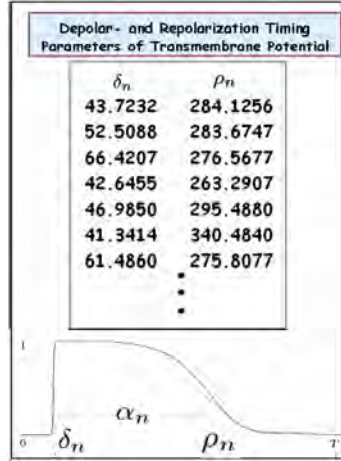


Figure 3.4: TMP timing parameters from ECGSIM [111].

where  $\bar{\rho}$  is the average repolarization timing parameter. Its integral can be used to construct  $\phi_{rep}$ , as shown in Equation (3.28). This approach has been first used by van Oosterom [106]. In his work, the dominant T wave was shown to be proportional to the square of  $\mathbf{V}^{tw}$ , which are BSPs during the T wave.

$$T_{dom} \propto \mathbf{1}^T (\mathbf{V}^{tw})^T \mathbf{V}^{tw} \quad (3.30)$$

where  $\mathbf{1}$  is the unit vector. Based on Equation (3.30), we calculated a dominant T wave,  $T_{dom}$ , from a set of normal BSPs. With this  $T_{dom}$ , the repolarization template was estimated, as shown in Figure 3.3. The BSPs employed here were exported from ECGSIM, which is a freeware electrophysiology simulation program developed by van Oosterom's group [111].

### The Transmembrane Potential Parameters

To generate TMPs on the heart surface, we need a set of parameters  $(k_n, \delta_n, \rho_n)$  for each location  $n$ . To simplify the problem, we set all  $k_n$  equal to 1 initially. Depolarization  $\{\delta_n\}$  and repolarization parameters  $\{\rho_n\}$  from ECGSIM, as shown in Figure 3.4 were used to adjust the template (Figure 3.2). With these parameters, we get TMPs,  $\Phi_m(t)$ , over the whole ventricular surface as shown in Figure 3.5. The  $\Phi_m(t)$  were be used as the normal TMPs for the simulation part of this study.



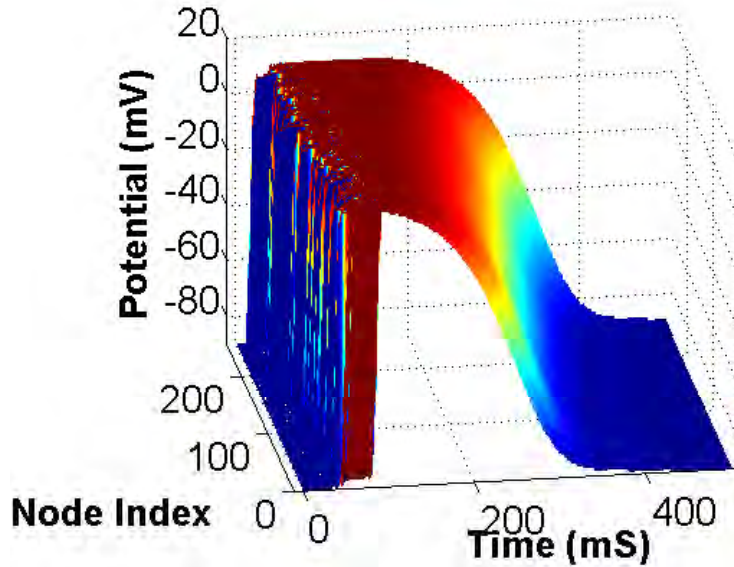


Figure 3.5: Transmembrane potentials at the 257 nodes on the ECGSIM ventricular model. The waveform template is composed of two parts: arctangent depolarization waveform and dominant T wave repolarization waveform.

Prolongation of TMP duration, or the length of the so-called action potential, is seen in many diabetic animal experiments [77, 21, 122, 14]. Based on the reference  $\Phi_m(t)$ , we can approximate diabetic TMPs by increasing the interval between  $\delta$  and  $\rho$  in certain patterns. The resulting heart- and body-surface potentials were calculated with the *Bidomain Forward-Problem Module*, and analyzed with the *Body Surface Mapping Module* in Figure 1.1. The source TMPs can be estimated from BSPs by solving the inverse problem. Details of this operation will be introduced in Chapter 4.

### 3.3.2 Numerical Representation of Torso Anatomy

To set up the simulation experiment, we used the heart-torso geometries exported from the ECGSIM platform [111], which included a 275-node ventricular model and a 300-node torso model, as shown on the left of the Figure 3.6. For more details, see the Appendix A. In the inhomogeneous forward problem simulation, we also employed lungs models previously used by Arthur [5], by scaling and fitting them into the ventricles-torso geometries as shown on the right of Figure 3.6. In addition,

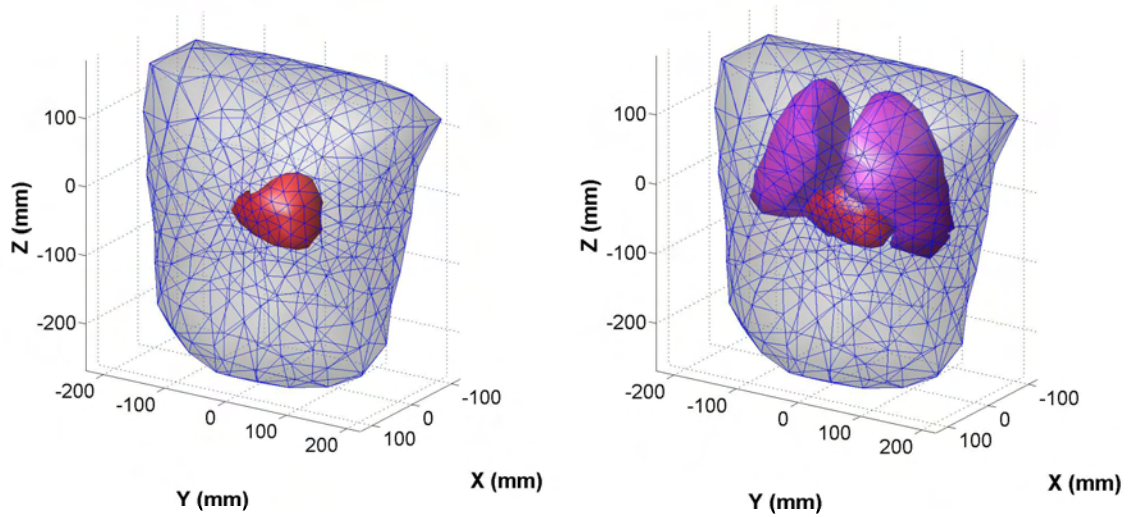


Figure 3.6: Left) ECGSIM heart-torso geometries; Right) Adding additional lung models to the ECGSIM geometries.

two blood-mass surfaces were generated to fit into the ECGSIM ventricle cavities, as shown in Figure 3.7.

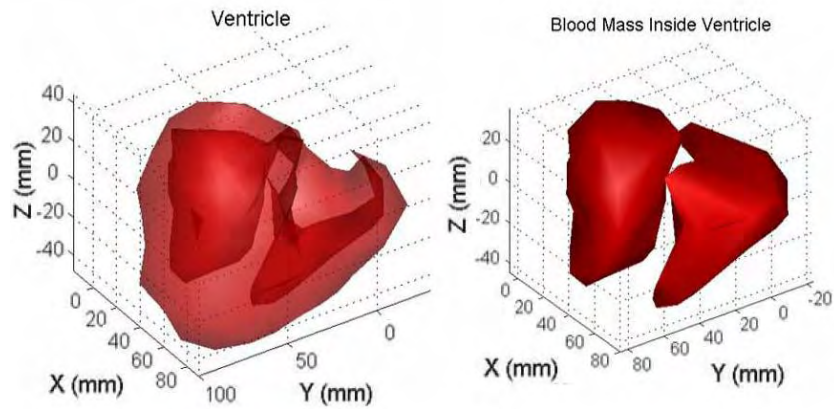


Figure 3.7: The ventricle model from ECGSIM with derived blood mass surfaces.

A series of simulation experiments was based on the above anatomic structures, especially the heart-torso geometries. They were used to test the forward problem, to evaluate the inverse problem approach, and to approximate certain BSP effects of an obese habitus. In addition to the geometries, organ conductivities are also needed

to establish the transfer matrix in the forward problem. The conductivities of heart, torso, blood and lung are approximated with 0.3, 0.2, 0.6, 0.05 S/m [68].

### 3.4 Bidomain Forward Problem Verification

The bidomain forward problem model is the foundation for the remaining work of this study, including solving the inverse problem, evaluating the anatomic effects of obesity, and estimating the electrical phenotype of diabetes. Therefore, it is important to make sure the forward problem solution is reliable. The previous section introduced an approach to solve the forward problem based on bidomain and double-layer models. In this section, we concentrate on verifying this approach.

The forward problem approach can be tested either by employing certain analytic methods [10, 6, 102], or by comparing simulation results with experimental recordings [86, 100, 107, 108]. Here a series of analytic procedures were developed and applied to verify the forward-problem routines.

Specifically, the verification was performed in three steps: 1) fundamental tests, 2) a homogeneous-volume test, and 3) an inhomogeneous-volume test. In the first step, the test contained two parts: 1) to verify solid-angle calculations based on its definition [112], 2) to test whether or not field potentials outside a closed uniform strength double-layer source equaled zero. After the fundamental test, dipole sources in a realistic homogeneous torso were employed to calculate BSPs. The simulated BSPs were integrated over the torso surface to see if the original dipole sources could be recovered [6]. Finally, the bidomain forward-problem routine was tested in an inhomogeneous volume conductor. In this test, surface potentials were calculated based on a set of eccentric-sphere conductors that surrounded a spherical double-layer source [89, 91]. Simulated potentials were compared to analytic results in the eccentric-spheres model.

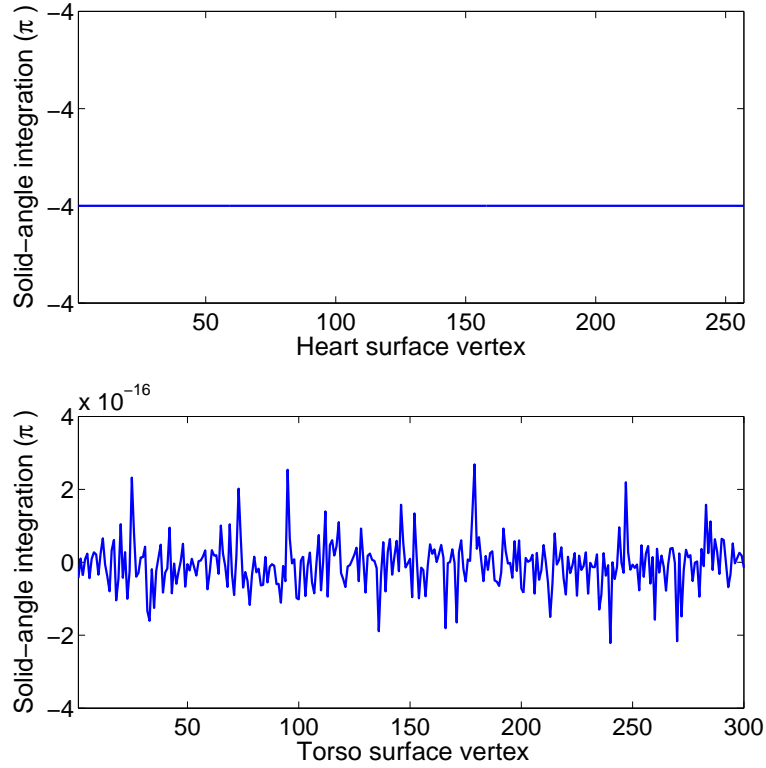


Figure 3.8: Solid angle verifications. Upper) the solid-angle divided by  $\pi$  subtended by the torso surface at the heart nodes, which are located inside of the torso surface. The plot indicates the value is precisely four. Lower) the solid-angle subtended by the heart surface at the torso nodes, which are located outside of the heart surface.

### 3.4.1 Fundamental Tests

As shown in Equation (3.26), surface potentials  $\mathbf{V}$  can be calculated by multiplying the transfer matrix  $\mathbf{A}$  by the cardiac surface TMPs  $\Phi_m$ . As the output of the bidomain forward problem,  $\mathbf{A}$  contains information on torso geometries and corresponding conductivities (see Equation (3.25)). Specifically, both primary and secondary potentials depend on solid-angles. In the first part of this test, we verified the solid-angle routine based on its definition. In addition, the transfer matrix  $\mathbf{A}$  was tested based on the fact that field potentials outside a closed uniform-strength, double-layer sources are zero.

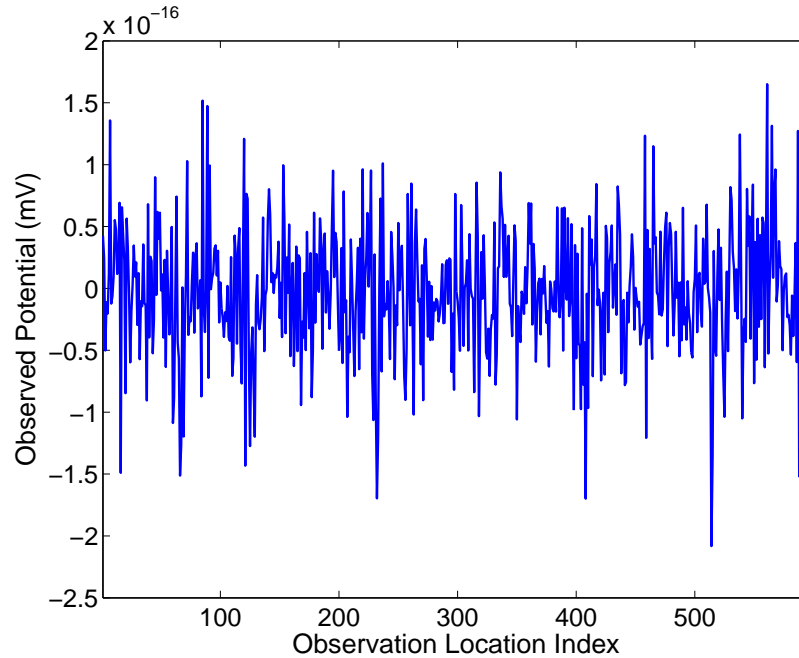


Figure 3.9: Body surface potentials observed outside a uniform strength double-layer source on a heart surface.

### Part 1: Verifying the Solid Angle

The solid-angle is defined as the surface’s projection onto the unit sphere centered at the observer [112]. It demonstrates how big a source object appears to an observation point. By its definition, the following two criteria should be met:

- Solid-angle equals  $\pm 4\pi$ , when it is subtended by a closed surface at an observation node inside the surface;
- Solid-angle equals 0, when it is subtended by a closed surface at an observation node outside the surface;

Corresponding to these criteria, two experiments were conducted to verify the solid-angle routine. First, we calculated the solid-angles subtended by the torso surface at nodes inside torso, such as nodes on the heart, to see if they all equaled  $\pm 4\pi$ . The result is shown in the upper section of Figure 3.8. We also calculated the solid-angle subtended by the heart surface at any nodes outside the heart surface, such as nodes

on the torso, to see if they all equal 0. The result is demonstrated in the lower section of Figure 3.8. Based on these results, we see that our solid-angle routine satisfies these fundamental criteria.

**Part 2: Verifying the transfer matrix  $\mathbf{A}$  with a closed uniform-strength, double-layer source.**

In this study, the double-layer model was used to represent source potentials. Based on the feature of source model, uniform-strength, double-layer sources will not produce an external field [106, 68]. This feature can be used to test the transfer matrix  $\mathbf{A}$ . By multiplying  $\mathbf{A}$  with a unit vector  $\mathbf{e}$  (representing a set of uniform strength sources), we expect to see that the resulting outside potentials are all zero, i.e.  $\mathbf{A}\mathbf{1} = 0$ . This result is shown in Figure (3.9), in which simulated body surface potentials from a uniform-strength, double-layer source over heart surface are close to zero. Clearly, the bidomain transfer matrix  $\mathbf{A}$  passed these tests.

### 3.4.2 Homogeneous Volume Test

In addition to the verification based on the features of the solid angle, the bidomain forward-problem approach was tested using unit dipole sources in a homogeneous volume conductor. In the next sub-section, we will discuss the more complicated situation of an inhomogeneous conductor.

As introduced in Chapter 2, BEM source models include: *dipole*, *multipole*, *distributed dipole* and *epicardial potentials* [68]. In the dipole model, the source is a single, fixed current moment per unit volume. The double-layer model is a distributed dipole source in which dipoles are uniformly distributed over a surface with enough density so that the distribution of dipoles can be well approximated with a continuous function. Verification based on a unit dipole sources can be used to test the bidomain forward problem approach developed for double-layer potential source because a unit dipole can be taken as a double-layer source with only one location being "turned on". In addition, both source models can be transformed into the impressed current density  $\mathbf{J}^i$ , and can be incorporated into the primary source term in the general BEM forward

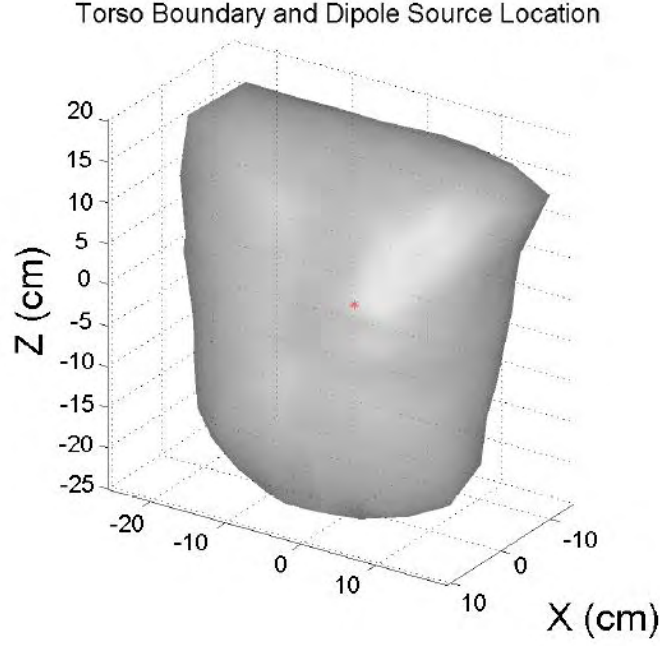


Figure 3.10: A dipole source (marked in red) locates at the origin, which inside a homogeneous torso.

problem formulation, Equation (3.3). Specifically, over a small area, a current dipole source  $\vec{p}$  can be represented as a function of the bidomain double-layer source  $\phi_m$  [36]:

$$\vec{p} = \int \mathbf{J}^i dv = - \int \sigma_i \nabla \phi_m dv = - \int \sigma_i \phi_m dS \quad , \quad (3.31)$$

Furthermore, the secondary source term in Equation (3.3) is only determined by boundaries. This term will not be affected by the choice of the source model. Therefore, the verification of the forward problem approach based on the unit dipole source in a homogeneous conductor is also valid for the case of a double-layer source in the same conductor.

## Methods and Results

According to the multipole model developed by Geselowitz and Arthur [33, 3, 6], the magnitude, orientation and location of a dipole source can be recovered from the surface potentials on a closed boundary surrounding the dipole. Specifically,  $a_{10}$ ,  $a_{11}$

and  $b_{11}$  represent  $z$ ,  $x$  and  $y$  components of the source dipole.  $a_{20}$ ,  $a_{21}$ ,  $b_{21}$ ,  $a_{22}$ , and  $b_{22}$  are quadrupole coefficients that contain information on the location of the dipole. These multipole coefficients can be calculated from surface potentials  $V$  as:

$$\begin{aligned}
a_{10} &= \int \sigma V dS_z \\
a_{11} &= \int \sigma V dS_x \\
b_{11} &= \int \sigma V dS_y \\
a_{20} &= \int \sigma V (2z dS_z - x dS_x - y dS_y) \\
a_{21} &= \int \sigma V (z dS_x + x dS_z) \\
b_{21} &= \int \sigma V (z dS_y + y dS_z) \\
a_{22} &= 1/2 \int \sigma V (x dS_x - y dS_y) \\
b_{22} &= 1/2 \int \sigma V (y dS_x + x dS_y)
\end{aligned} \tag{3.32}$$

Note that all of the quadrupole coefficients equal zero for a dipole source if the origin is at the dipole location.

For this verification, we selected three dipole sources (unit vector along X-, Y- and Z-axis) located at the origin surrounded by a homogeneous torso, as shown in Figure 3.11. Correspondingly, body surface potentials (BSPs) were calculated from these sources with our bidomain forward problem approach, as shown in Figure 3.10. By integrating BSPs using Equation (3.32), we obtained the recovered source coefficients. Table 3.1 and Figure 3.12 show these recovered coefficients along with the original coefficients. From these results, we can tell that the dipole source can be recovered from BSPs with a root mean square (RMS) error equaling to 0.303%, indicating the bidomain forward-problem approach is reliable for the case of the double-layer source within an homogeneous torso.

Table 3.1: Multipole coefficients recovered from BSP integration.

Original Source	Recovered Source Coefficients							
	$a_{11}$	$b_{11}$	$a_{10}$	$a_{20}$	$a_{21}$	$b_{21}$	$a_{22}$	$b_{22}$
$a_{11}$	0.9918	-0.0009	-0.0008	0.0569	-0.0108	0.0047	-0.0153	-0.0045
$b_{11}$	-0.0004	0.9967	-0.0002	0.0320	0.0041	0.0085	-0.0056	-0.0064
$a_{10}$	-0.0002	0.0000	0.9980	-0.0059	-0.0032	-0.0056	-0.0037	-0.0009



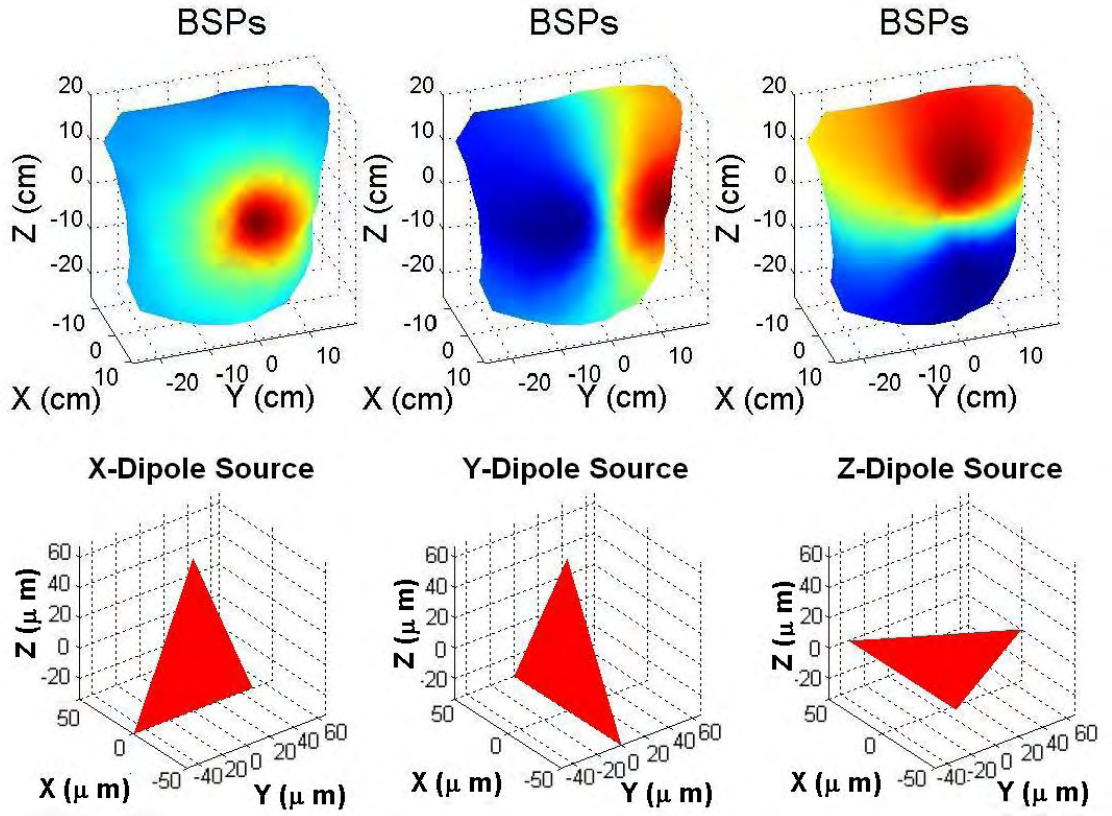


Figure 3.11: The point like dipole sources along X-, Y- and Z-axis, and the resulting body surface potentials.

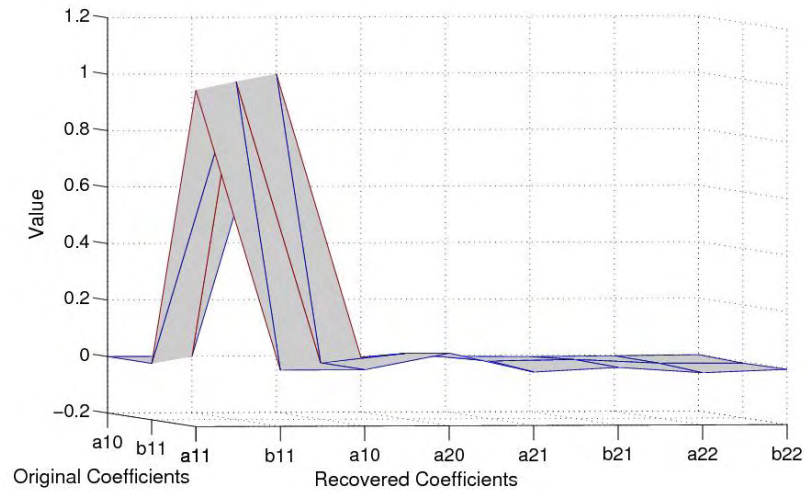


Figure 3.12: Multipole coefficients recovery.

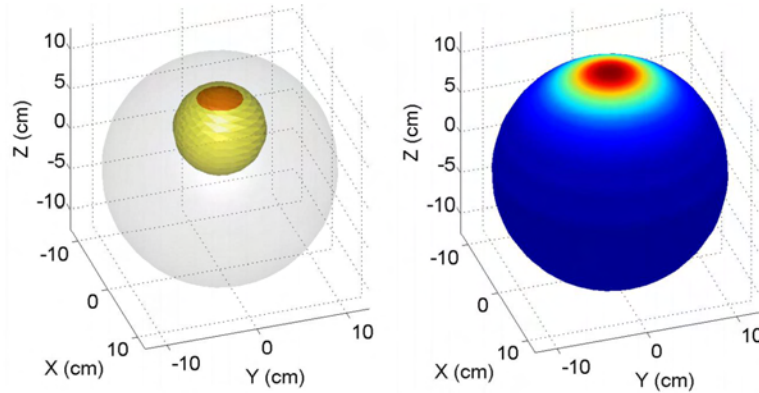


Figure 3.13: Left) Eccentric spheres (ESS) model geometry, including torso shell (in grey), heart shell (in yellow) and source cap (in red). Right) Simulated surface potentials on torso shell.

### 3.4.3 Inhomogeneous Volume Test

In the previous two sub-sections, the bidomain forward problem approach has been verified with the fundamental test and the homogeneous volume test. In this sub-section, the forward problem approach will be tested for the case of the double-layer source within an inhomogeneous volume conductor. To accomplish this test, we employed an eccentric spheres model (ESM), which was first constructed by Rudy [89, 91].

Similar to the model used in [89, 91], a reference eccentric spheres model was built based on which surface potentials were calculated with the bidomain forward problem approach. Simulated potentials were compared to their corresponding analytic results. The model consisted of 2 regions of homogeneous conductivity: a heart with a radius of 5 cm and a conductivity of 0.6 S/m and a torso with a radius of 12.5 cm and a conductivity of 0.2 S/m.

The heart was located at an eccentricity of 5 cm from the center of the torso [89, 91]. The source was a uniform dipole layer in the shape of a spherical cap, ranging from  $5^\circ$  to  $36^\circ$ . The ESM geometry and resulting simulated torso surface potentials are shown in Figure 3.13. Potentials were calculated on the heart and torso surfaces using a 50-term Legendre polynomial expansion [89, 91]. Analytic results were calculated with the routine provided by Beetner and Arthur [11, 12].

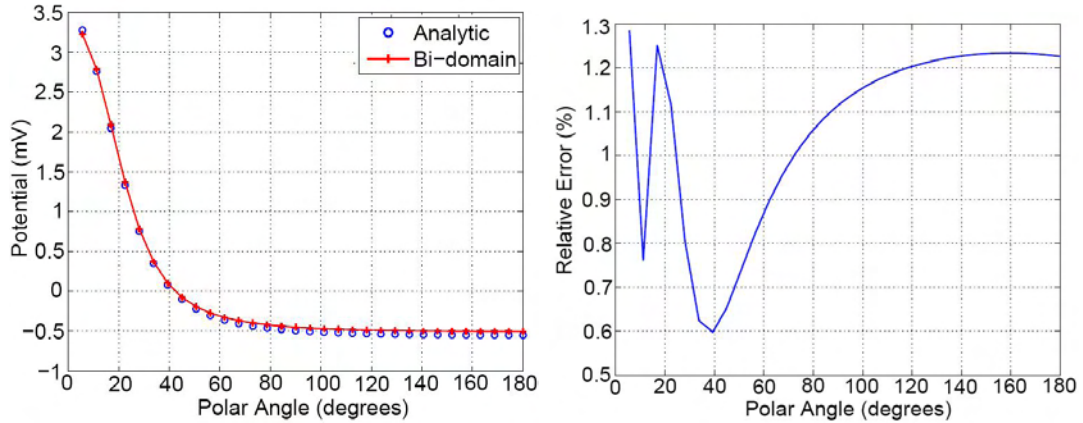


Figure 3.14: Left) Simulated (solid line) and Analytic (circle) surface potentials for polar angle from  $0^\circ$  to  $180^\circ$ . Right) Relative error of simulated surface potentials for polar angle from  $0^\circ$  to  $180^\circ$ .

Because the ESM is azimuthally symmetric, potentials along one longitude line (from  $0^\circ$  to  $180^\circ$ ) can be used to demonstrate the potential distribution over the whole sphere surface. Simulated and analytic surface potentials along the longitude line on the torso sphere are shown on the left side of Figure 3.14. The relative differences between them are small, ranging from 0.60% to 1.29%, as shown on the right side of the figure. These results indicate that the bidomain forward-problem approach is valid for the inhomogeneous case. During the simulation, the average numerical error was reduced from (3% to 1.1%) by increasing the torso resolution from  $(16 \times 16)$  to  $32 \times 32$ .

In this section, the bidomain forward problem approach has been verified in three ways: the fundamental test, the homogeneous volume test, and the inhomogeneous volume test. Based on these tests, we showed that our forward problem approach is reliable for environments with the double-layer sources inside either homogeneous or inhomogeneous volume conductors. In the following chapters, this bidomain approach will be used to estimate body surface potentials from the diabetic heart TMPs, considering torso variations in the anatomy of obese subjects.

Furthermore, based on the output of the bidomain forward problem, the inverse problem will be formulated and solved. Precise reconstruction of the source potentials

from BSPs is another verification of the forward-problem formulation. For details, see Section 4.3.

# Chapter 4

## Bidomain Inverse Problem

### 4.1 Problem Statement

Diseases such as Type II diabetes may lead to abnormalities in the transmembrane potentials (TMPs) of cardiac myocytes that are manifest as changes in body-surface potentials (BSPs), such as long QT syndrome. Direct inference of TMPs from body surface potentials for use in clinical practice, however, remains a challenge. Several groups have been working on the reconstruction of TMPs from BSPs [70, 103, 107]. Nevertheless, limited accuracy and sensitivity to noise are problems that have not been resolved. In this chapter, a new inverse approach called regularized waveform identification (RWI) is developed. RWI combines spatial regularization with temporal optimization to estimate TMPs from BSPs with greater accuracy than conventional regularization alone.

The inverse problem is formulated based on the bidomain model developed in the previous chapter. In that model, BSPs,  $\mathbf{V}$ , are determined from cardiac TMPs,  $\Phi_{\mathbf{m}}$ , by multiplying them by the transfer matrix  $\mathbf{A}$ ,

$$\mathbf{V} = \mathbf{A}\Phi_{\mathbf{m}} \quad . \quad (4.1)$$

With the bidomain model, the inverse approach was developed to reconstruct  $\Phi_{\mathbf{m}}$  from the observed  $\mathbf{V}$ , given the transfer matrix  $\mathbf{A}$  established from the forward problem.

Many diabetes and obesity associated ECG features have been found during S-T segment and T wave. In this chapter, we focus on the repolarization TMPs. Due to the quasi-static features of the inverse problem, repolarization potentials can be reconstructed from the T wave measured on the body surface. During the S-T segment and T wave, the repolarization  $\Phi_{\mathbf{m}}$  is a function of the repolarization timing parameter  $\vec{\rho}$ , that is  $\Phi_{\mathbf{m}}(t; \vec{\rho})$ .

The parameter  $\vec{\rho}$  is used to indicate the instant at which the steepest decrease in the TMP occurs. It varies from location to location. After selecting a waveform template (such as the integral of dominant-T wave or the logistic function), we can determine the  $\Phi_{\mathbf{m}}$  and its  $\vec{\rho}$  from each other.

The inverse approach developed in this chapter was implemented in MATLAB. These corresponding implementations were incorporated into the bidomain simulation platform (Figure 1.1) as the *Cardio-myocyte transmembrane potential Estimation Module*, or the so called the inverse-problem module.

## 4.2 Theoretical Framework

### 4.2.1 Least Squares Estimation (LSE)

In general, the least-squares approach is optimal if the errors are zero-mean, uncorrelated, and have equal variances [53, 118]. For the linear model in Equation (4.1), the objective is to find the  $\Phi_{\mathbf{m}}$ , which minimize the body-surface residual error, as

$$J = \sum_{t=1}^T \|\mathbf{V} - \mathbf{A}\Phi_{\mathbf{m}}\|^2 \quad (4.2)$$

in which  $T$  is the time span, such as the QRS-complex or the T wave. The least-squares solution for the above equation is:

$$\Phi_{\mathbf{m}} = (\mathbf{A}^T \mathbf{A})^{-1} \mathbf{A}^T \mathbf{V} \quad . \quad (4.3)$$

This estimation problem, however, is ill-conditioned, i.e. matrix  $\mathbf{A}$  has a large condition number. Under this situation, any small changes in the measured BSPs will have drastic effects on the estimated  $\Phi_{\mathbf{m}}$ . Therefore, Equation (4.3) is usually not useful. To solve this problem, regularization has often been introduced to smooth or to set a bound on the inverse problem solution.

## 4.2.2 Regularization

Typically, regularization is achieved by adding one or more penalty terms to the residual function. These penalty terms act as constraints incorporating prior information into the inverse model [66]. Several regularization techniques have been adopted to solve the inverse-problem, such as: Tikhonov regularization (considering amplitude or spatial constraints) [69, 90], truncated singular value decomposition (TSVD) [95, 44, 47], Twomey regularization (considering temporal constraints) [69, 82], and multiple constraint methods [15, 16, 66]. In this study, we selected two well-developed, widely used regularization approaches, TSVD and Tikhonov, to handle the ill-conditioned situation. These two methods demonstrate the limits of regularization for the bidomain inverse problem.

### TSVD Regularization

From the numerical point of view, the transfer matrix  $\mathbf{A}$  has one or more near-to-zero singular values, which contribute to its ill-conditioned property. TSVD solves this problem by removing the small singular values from  $\mathbf{A}$ , resulting in a rank-deficient matrix  $\mathbf{A}_{\mathbf{k}}$ . Source potentials can be estimated with the pseudo-inverse of  $\mathbf{A}_{\mathbf{k}}$ . This approach contains the following steps:

1. Decompose  $\mathbf{A}$  with SVD, as  $\mathbf{A} = U\Sigma V^T$ ;
2. Remove the  $k$  smallest singular values from diagonal matrix  $\Sigma$ , by setting them to zero, the resulted matrix becomes  $\Sigma_{\mathbf{k}}$ ;
3. Construct  $\mathbf{A}_{\mathbf{k}}$  from  $\Sigma_{\mathbf{k}}$ , as  $\mathbf{A}_{\mathbf{k}} = U\Sigma_{\mathbf{k}} V^T$ ;

4. Calculate the pseudo inverse of  $\mathbf{A}_k$  as  $\mathbf{A}_k^\dagger = V\Sigma_k^{-1}U^T$ .

In the above steps,  $U$  and  $V$  are unitary matrices, containing orthonormal basis vectors. The regularized estimate of the TMPs thus becomes

$$\Phi_{\text{TSVD}} = \mathbf{A}_k^\dagger \mathbf{V} = V\Sigma_k^{-1}U^T\mathbf{V}. \quad (4.4)$$

The above solution is the minimum-norm least-squares solution for  $\Phi_m$  [44], that is it finds the

$$\min \|\Phi_m\|^2 \text{ subject to } \min \|\mathbf{A}_k\Phi_m - \mathbf{V}\|^2 \quad .$$

### Tikhonov Regularization

In Tikhonov regularization a constraint term is added to the residual term to obtain spatial smoothness and thereby reduce the amplitude of estimates of the TMPs. There are three commonly used Tikhonov approaches: zero, first- and second-order regularization. They all share a common objective function

$$\|J\|^2 = \|\mathbf{V} - \mathbf{A}\Phi_m\|^2 + \lambda\|\mathbf{R}\Phi_m\|^2 \quad . \quad (4.5)$$

In the zero-order Tikhonov,  $\mathbf{R}$  is an identity matrix. In the first-order and second-order Tikhonov methods,  $\mathbf{R}$  is the surface gradient operator or the surface Laplacian operator, respectively.

The Tikhonov regularization solution is [69, 90]

$$\Phi_{\text{Tikh}} = (\mathbf{A}^T\mathbf{A} - \lambda\mathbf{R}^T\mathbf{R})^{-1}\mathbf{A}^T\mathbf{V} \quad , \quad (4.6)$$

where  $\lambda$  is a weighting parameter, known as the "regularization parameter". It is used to control the tradeoff between the residual error and regularization term. The regularization weighting parameter can be found with a variety of techniques, such as the CRESO (Composite Residual Smoothing Operator) or L-curve and the zero-crossing techniques [3, 11, 49, 114]. The value of this parameter is crucial to the accuracy of results. There is often only a small range of values that work well [69].



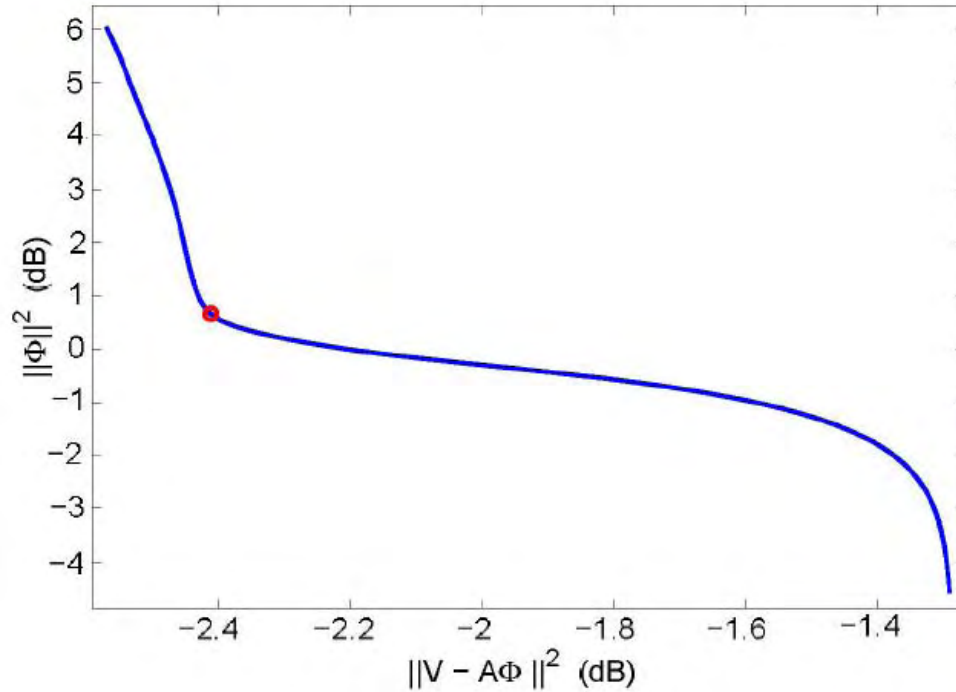


Figure 4.1: Regularization parameter  $\lambda$  is determined by means of the maximum curvature of the L-curve.

In this study, we use the L-curve, as shown in Figure 4.1 to find effective values for  $\lambda$ . In Equation (4.5), the regularization term is a function of the TMP. This constraint was used to achieve spatial smoothness of TMPs. For similar reasons the timing parameters,  $\vec{\delta}$  and  $\vec{\rho}$ , have been employed to calculate the regularization term in other bidomain inverse studies [103, 107].

### 4.2.3 Regularized Waveform Identification (RWI)

Spatial regularization can be achieved with the above TSVD or Tikhonov approaches. The corresponding TMP estimates are then calculated with Equations (4.4) or (4.5). If these regularization methods do not provide adequate estimation accuracy, is there a better way to reconstruct the source potentials? These questions are addressed in this section.

## Rank-deficient Problem

Given the property of the source model, the bidomain inverse problem is a rank-deficient one, i.e. the transfer matrix  $\mathbf{A}$  is not a numerically full-rank matrix [44]. For example, it is known that the uniform strength double-layer source will not produce an external field [106], i.e.

$$\mathbf{A}\mathbf{1} = \mathbf{A} \begin{bmatrix} 1 \\ 1 \\ \cdot \\ 1 \end{bmatrix} = \mathbf{0} \quad , \quad (4.7)$$

where,  $\mathbf{1}$  is a unit vector, and  $\mathbf{0}$  is a zero vector. In other words, the unit vector belongs to the null space of  $\mathbf{A}$ , represented as  $N(\mathbf{A})$ ,

$$\mathbf{1} \in N(\mathbf{A}) = \{\vec{v} | \mathbf{A}\vec{v} = \mathbf{0}\} \quad . \quad (4.8)$$

By defining a matrix  $\mathbf{W}$ , which has identical rows, we will also get a zero matrix by multiplying  $\mathbf{A}$  by  $\mathbf{W}$ .

$$\mathbf{AW} = \mathbf{A} \begin{bmatrix} n_1 & n_2 & \dots & n_k \\ n_1 & n_2 & \dots & n_k \\ \cdot & \cdot & \cdot & \cdot \\ n_1 & n_2 & \dots & n_k \end{bmatrix} = [\mathbf{0}] \quad , \quad (4.9)$$

where  $n_1, n_2, \dots, n_k$  are any real values. If  $n_1 = n_2 = \dots = n_k$ ,  $\mathbf{W}$  becomes a unit matrix  $\mathbf{U}$ , then

$$\frac{1}{m}\mathbf{AU}\Phi_{\text{esti}} = \mathbf{A}\left(\frac{1}{m}\mathbf{U}\Phi_{\text{esti}}\right) = \mathbf{A} \begin{bmatrix} \phi_{\text{ave}} \\ \phi_{\text{ave}} \\ \dots \\ \phi_{\text{ave}} \end{bmatrix} = [\mathbf{0}] \quad .$$

In the above equation,  $\mathbf{U}$  is an  $n \times m$  matrix with all of its elements equal to 1,  $n$  and  $m$  are numbers of nodes on body- and heart-surface models, respectively.

In particular,

$$\mathbf{A}\Phi_{\text{ave}} = \mathbf{A} \begin{bmatrix} \phi_{\text{ave}} \\ \phi_{\text{ave}} \\ \dots \\ \phi_{\text{ave}} \end{bmatrix} \quad (4.10)$$

The matrix  $\Phi_{\text{ave}}$  has identical vectors,  $\phi_{\text{ave}}$ , which represent the spatial average of the ideal TMP estimate  $\Phi_{\text{esti}}$ , and contains the temporal information of the TMPs. Thus  $\phi_{\text{ave}}$  is called the averaged waveform, and  $\Phi_{\text{ave}}$  is called the averaged waveform matrix.

Because the ideal estimate  $\Phi_{\text{esti}}$  should satisfy Equation (4.1), it follows that

$$\begin{aligned} \mathbf{V} &= \mathbf{A}\Phi_{\text{esti}} \\ &= \mathbf{A}\Phi_{\text{esti}} - \frac{1}{m}\mathbf{A}\mathbf{U}\Phi_{\text{esti}} \\ &= \mathbf{A}[\Phi_{\text{esti}} - \frac{1}{m}\mathbf{U}\Phi_{\text{esti}}] \end{aligned} \quad (4.11)$$

Based on Equation (4.10), the above equation can be re-written as

$$\mathbf{V} = \mathbf{A}[\Phi_{\text{esti}} - \Phi_{\text{ave}}] = \mathbf{A}\Phi_{\mathbf{m}} \quad (4.12)$$

There are an infinite number of estimates of  $\Phi_{\mathbf{m}}$  that satisfy this expression. Among them,  $\Phi_{\text{TSVD}}$  and  $\Phi_{\text{Tikh}}$  are two approximations that employ similar criteria: they try to minimize the residual error on the body-surface, as well as minimize the energy level of estimated sources, measured by  $\|\Phi_{\mathbf{m}}\|^2$  [44]. Based on the current knowledge of ventricular myocyte TMPs, we know that during the early plateau stage, instead of equaling to zero, the TMPs are all positive values. This phenomenon indicates the true TMPs set is not the one with small  $\|\Phi_{\mathbf{m}}\|^2$ , as both  $\Phi_{\text{TSVD}}$  or  $\Phi_{\text{Tikh}}$  yield.

By subtracting  $\Phi_{\text{ave}}$  from the ideal estimate  $\Phi_{\text{esti}}$  in Equation (4.12), we get an estimate with a small signal energy level, which can be approximated by  $\Phi_{\text{TSVD}}$  or  $\Phi_{\text{Tikh}}$ .  $\Phi_{\text{esti}}$  can therefore be approximated as the summation of  $\Phi_{\text{ave}}$  and a regularization result,

$$\Phi_{\text{esti}} = \Phi_{\text{ave}} + \Phi_{\text{TSVD}}, \quad (4.13)$$

or

$$\Phi_{\text{esti}} = \Phi_{\text{ave}} + \Phi_{\text{Tikh}}. \quad (4.14)$$

In the above equations, the regularization terms are calculated based on the transfer matrix  $\mathbf{A}$ , BSPs and the spatial constraints. The averaged waveform term allows inclusion of temporal constraints into the final TMP estimate. The new inverse approach introduced here is called regularized waveform identification (RWI), because it incorporates both spatial and temporal information by summing the regularization results and the averaged TMP waveform. In this study, the averaged TMP waveform was found with a non-linear optimization technique.

### Optimization

To determine the average waveform,  $\phi_{\text{ave}}$ , we used the general TMP waveform as a reference. In other studies, several functions and their combinations have been used to approximate the general TMP shape. Specifically, the repolarization waveform has been approximated with six linear segments [71], an exponential function [26], a logistic function [110], or an integral of dominant T wave [106]. In this study, an integral of dominant T wave was chosen to represent the shape of the repolarization TMP waveform, as shown in Figure 3.2.

Consequently, in this study, the averaged wave  $\phi_{\text{ave}}$  has the form,

$$\phi_{\text{ave}}(t, \rho_{\text{ave}}) \propto - \int \mathbf{T}_{\text{dom}}(t - \rho_{\text{ave}}) dt \quad . \quad (4.15)$$

An alternate that was explored was to use a logistic function to represent the TMP wave shape,

$$\phi_{\text{ave}}(t, \rho_{\text{ave}}) \propto \frac{1}{1 + e^{-\alpha(t - \rho_{\text{ave}})}} \quad . \quad (4.16)$$

In the above equations,  $\rho_{\text{ave}}$  is the timing parameter for the averaged repolarization waveform, indicating the instant when the steepest potential descending occurs. To match TMP waveforms,  $\phi_{\text{ave}}$  was shifted in time and scaled in amplitude to the range of -90 to +10 mV.

Given a shape for the averaged waveform, we determined the 'optimal' choice for  $\rho_{ave}$ . To accomplish this task, an optimization method based on the Levenberg-Marquardt algorithm (LMA) was employed. The optimization procedure is described in the following steps:

1. Estimate the regularized TMPs, with for example TSVD, as  $\Phi_{TSVD}$ .
2. Initialize  $\rho_{ave}$ , as  $\rho_{ave}^0$ , and calculate the corresponding  $\phi_{ave}$  and  $\Phi_{ave}$ .
3. Calculate the estimated TMPs  $\hat{\Phi}_{esti}$ , as  $\hat{\Phi}_{esti} = \Phi_{ave} + \Phi_{TSVD}$ .
4. Calculate the corresponding BSPs  $\hat{V}$  from  $\hat{\Phi}_{esti}$ , and evaluate the BSP residue error.
5. Calculate the cost value with the optimization objective function using the results of steps 3 and 4.
6. Test for convergence of the independent variable  $\rho_{ave}$ . If so, quit; if not, update  $\rho_{ave}^k$  and go to step 3.

At each optimization iteration,  $\Phi_{esti}$  was estimated as the sum of  $\Phi_{ave}$  and the regularization result from either Equation (4.13) or (4.14). Based on the TMP repolarization waveform, the following three criteria were used to formulate the optimization objective function.

- $\Phi_{esti} \leq 10\text{mV}$ , (TMP voltage is less than 10mV);
- $\Phi_{esti} \geq -90\text{mV}$ , (TMP voltage is greater than  $-90\text{mV}$ );
- $\Phi_{esti}(t_i) \geq \Phi_{esti}(t_j)$  ( $t_i \leq t_j$ ), (TMP is monotonically decreasing during repolarization).

In addition to the above constraints the BSP residue was minimized during the optimization. The overall objective function was:

$$\begin{aligned}
f(\rho_{ave}) = & \sum \{ \sum \max(0, \Phi_{\text{esti}} - 10) \\
& + \gamma_1 \sum \max(0, -90 - \Phi_{\text{esti}}) \\
& + \gamma_2 \sum | \max(0, \Phi_{\text{esti}}(t_2 : t_l) - \Phi_{\text{esti}}(t_1 : t_{l-1})) | \} \\
& + \gamma_3 \| \mathbf{V} - \mathbf{A} \Phi_{\text{esti}} \|,
\end{aligned} \tag{4.17}$$

where,  $\{t_1, t_2, \dots, t_l\}$  are time coordinates of  $\Phi_{\text{esti}}$ .  $\gamma_1$ ,  $\gamma_2$  and  $\gamma_3$  are weighting parameters for the penalty terms. In Equation (4.17), the first term describes the estimated TMPs that extend over the upper bound of the actual TMP waveform, 10 mV. For any TMPs equal or less than 10 mV, this penalty term is zero. Similarly, the second term includes all TMPs that are less than the lower bound, -90 mV. The last term in Equation (4.17) is used to make sure that the TMPs are monotonically decreasing for any of these time instants.

In the next section, we evaluate the RWI technique in simulation. For the zero-noise case, it takes 200 iterations to find the global optimization result. The effect of initial value is negligible. For the case with measurement noise, it takes more than 1000 steps to converge. In this case, the initial value matters because multiple local optimal solutions may exist.

### 4.3 Methods and Results

To solve the bidomain inverse problem, we developed an innovative approach, regularized waveform identification (RWI). In the approach, spatial constraints were applied with the regularization techniques, such as the truncated SVD (TSVD) and the Tikhonov. Temporal constraints were incorporated by introducing the actual waveform of the TMPs. This new method combines spatial and temporal constraints by summing the regularization results with the averaged TMP waveform. Parameters of the waveform were determined with a non-linear optimization technique.

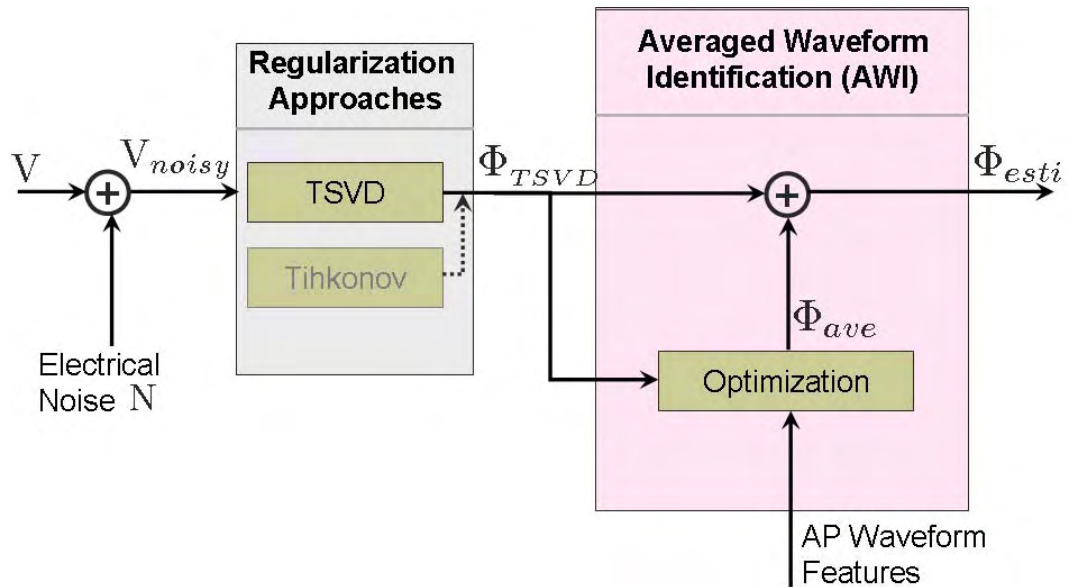


Figure 4.2: The regularized waveform identification (RWI) scheme is developed to solve the bidomain inverse problem. It contains two parts: the regularization for the spatial regularization, and the averaged waveform identification (AWI) used to find the optimal averaged waveform, which contains the temporal information.

The flow chart of the inverse problem approach is shown in Figure 4.2. From body-surface ECGs, we calculated the regularized estimates of the TMPs. Both the regularization results and the general waveform template are fed into the optimization procedure to find the optimal estimation of source potentials.

The proposed inverse approach was tested with heart-torso models and source potential parameters exported from ECGSIM [111]. With the transfer matrix  $\mathbf{A}$  and the reference source potentials  $\Phi_{ref}$  the reference BSPs,  $\mathbf{V}_{ref}$ , were found during the T wave as shown in Figure 4.3.

From the reference BSPs, regularized TMPs estimates were determined with the TSVD and Tikhonov techniques. As demonstrated in Figure 4.4, the RWI method estimated the TMP sources from the sum of the regularization result and the averaged TMP waveform.

In this study, we used three regularization methods: TSVD, zero-order Tikhonov and Laplacian (second-order Tikhonov). The regularization weighting parameter was

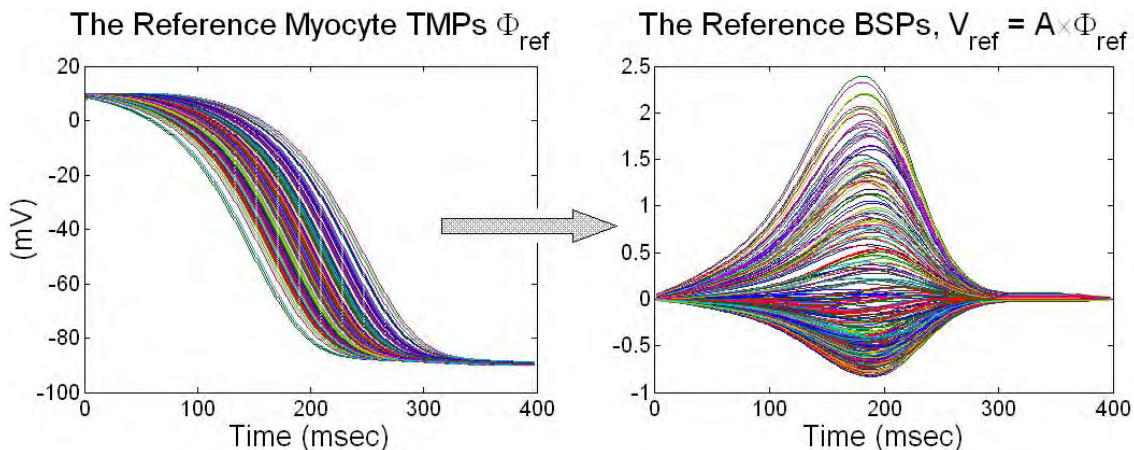


Figure 4.3: The reference repolarization TMPs and corresponding BSPs during the T wave.

found for the Tikhonov approaches from the maximum curvature of the L-curve. For the TSVD method, the truncation rank was determined from estimated noise levels. Noise levels were found by subtracting low-pass filtered signals from the raw signals using the approach introduced previously to study artifacts in ECGs [4]. In Figure 4.5, the three regularization results,  $\Phi_{\text{Tikh}}$ ,  $\Phi_{\text{TSVD}}$  and  $\Phi_{\text{Laplacian}}$ , are compared with the RWI estimates.

$\Phi_{\text{TSVD}}$  is more successful at reducing noise effects without loss of signal energy than  $\Phi_{\text{Tikh}}$  and  $\Phi_{\text{Laplacian}}$  regularization. None of the regularization results, however, accurately represents the basic waveform of the reference TMPs. To solve this problem, we incorporated temporal constraints by adding the averaged waveform  $\phi_{ave}$  to the regularization results, as shown in Figure 4.4. The shape of  $\phi_{ave}$  is based on the general TMP waveform. The repolarization parameter for  $\phi_{ave}$ ,  $\rho_{ave}$ , was determined with a unconstrained nonlinear optimization approach. It was performed with the LMA algorithm provided by MATLAB<sup>®</sup>. A logistic function was used to approximate the averaged waveform, during optimization iterations.

The timing parameters  $\vec{\rho}_{esti}$  can be extracted from the reconstructed TMPs  $\Phi_{esti}$ . Figure 4.6 suggests that the new inverse approach can be used to reconstruct the repolarization TMPs and  $\rho$ , with improved accuracy, at least in a noise-free environment.



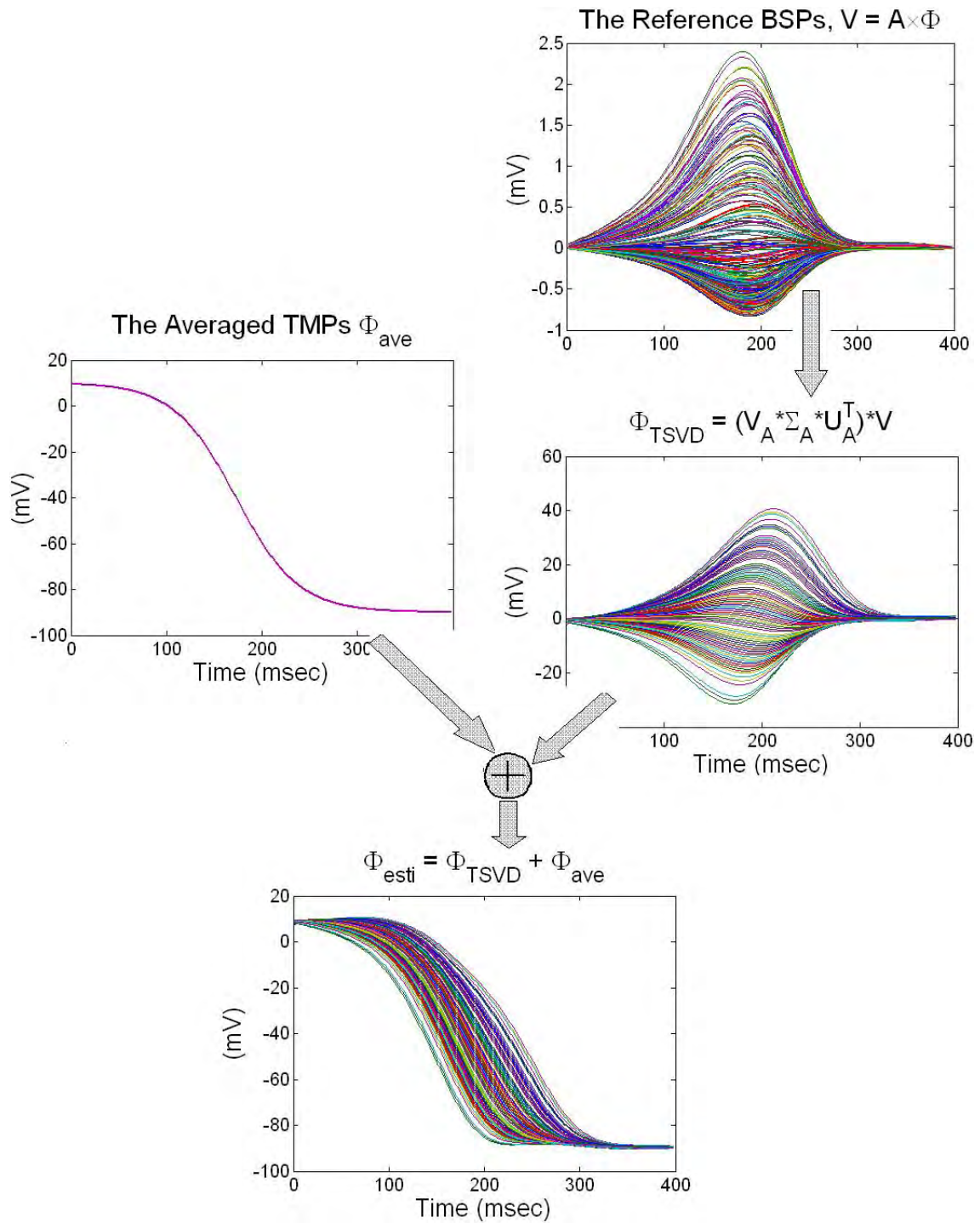


Figure 4.4: The final reconstruction is achieved by adding regularization results with averaged waveform.

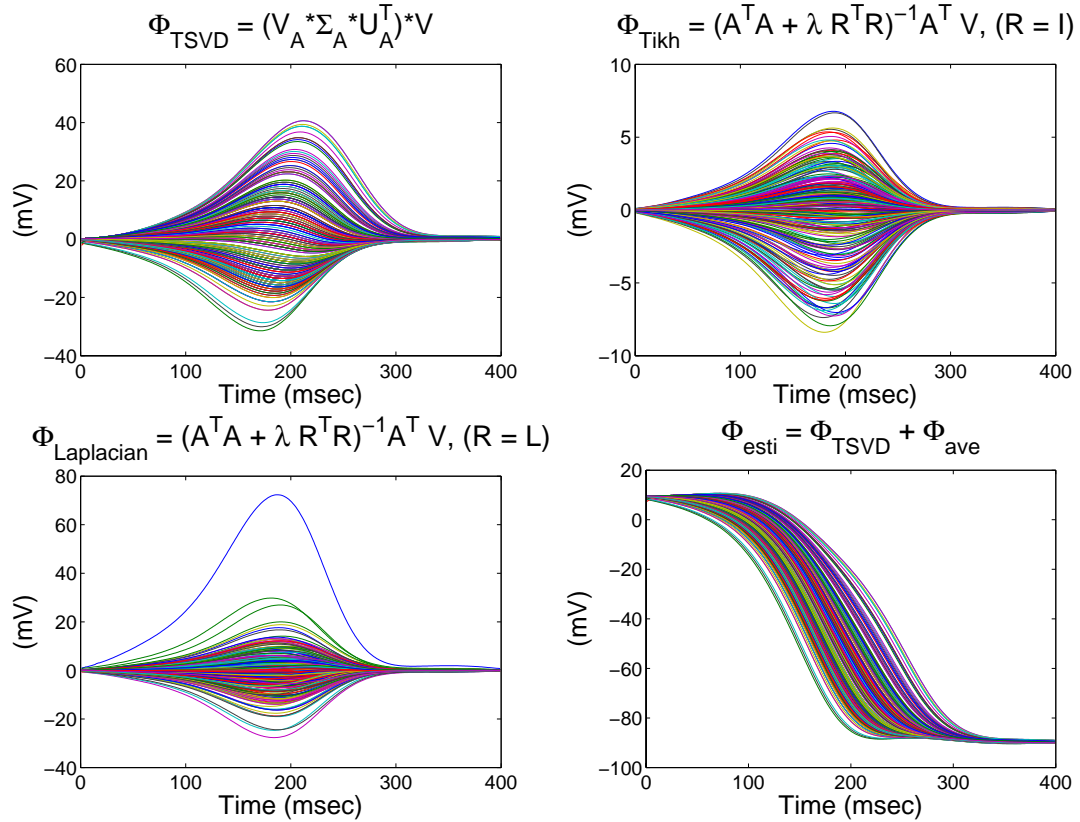


Figure 4.5: TMPs reconstructed from BSPs without noise. Upper Left, The truncated SVD (TSVD) regularized TMPs  $\Phi_{TSVD}$ . Upper Right, The zero-order Tikhonov regularized TMPs  $\Phi_{TSVD}$ . Lower Left, The Laplacian regularized TMPs  $\Phi_{Laplacian}$ . Lower Right, the TMPs estimated with the new developed approach.

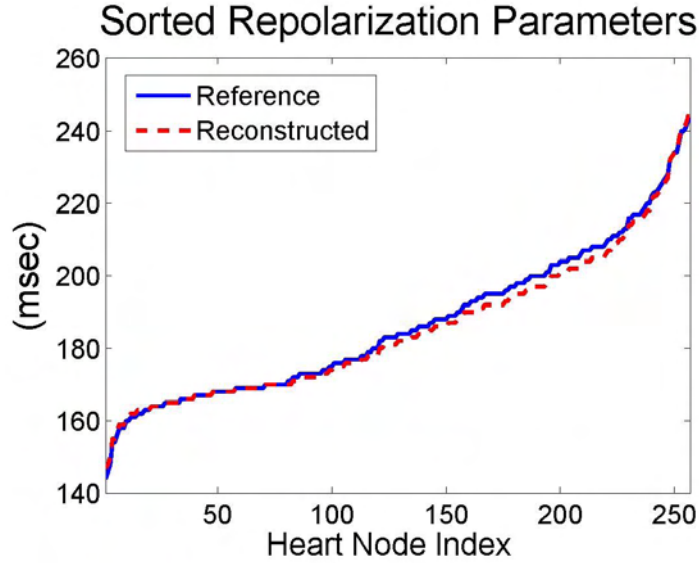


Figure 4.6: Without electrical or geometric noises, the new RWI reconstructs the repolarization timing parameters precisely (RE=0.0657; CC=0.9984).

Additional tests were made, however, on the RWI method. Specifically, two types of disturbance were simulated to approximate the real circumstance. They were: (1) the addition of electrical noise to the body surface ECG measurements; (2) the introduction of geometrical error in heart shape and position. The sensitivity of RMI to the electrical noise and to the geometric errors was evaluated with the simulation experiments.

### 4.3.1 Sensitivity of RWI to Electrical Noise

Electrical noise in ECG recordings is a critical issue in the inverse problem. Small amounts of noise can cause large errors in the result of the inverse problem. Therefore, it is important to evaluate the sensitivity of the proposed approach to the electrical noise. In this study, the electrical noise was simulated with additive white noise with 1%, 2%, 5%, and 10% noise-to-signal ratios (NSR).

Figure 4.7 shows the effects of 1% noise on the regularization results  $\Phi_{\text{TSVD}}$  and  $\Phi_{\text{Tikh}}$  estimated from the noisy BSPs. Similar to the noise-free case, the TSVD technique was better. It was more efficient at noise compression than zero-order

Tikhonov regularization. The corresponding RWI estimates of TMPs are depicted in Figure 4.8. The reconstructed signals are clearly much closer to the reference TMPs than regularization alone. This phenomenon is due to the information loss during regularization.

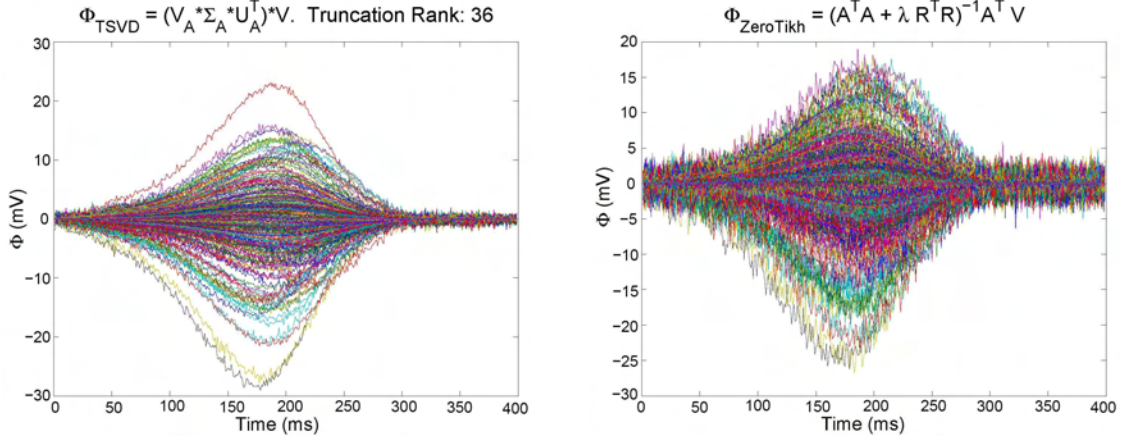


Figure 4.7: Regularization TMP estimated under 1% white noise. Left)  $\Phi_{\text{TSVD}}$  estimated from truncated SVD regularization approach. Right)  $\Phi_{\text{Tikh}}$  estimated from zero-order Tikhonov regularization approach.

Figure 4.9 shows the comparison between reconstructed and reference TMPs. To provide a full view of repolarization, six snap shots were taken during the T wave, which is the consequence of the ventricular repolarization. The results indicate that new inverse approach is able to reconstruct the TMP distribution pattern during the repolarization.

Relative error (RE) and the correlation coefficient (CC) were used to quantify the similarity between the reconstructed and reference source potentials. They were calculated with the following expressions:

$$RE = \frac{\|X_{ref} - X\|}{\|X_{ref}\|} \quad (4.18)$$

$$CC = \frac{(X_{ref} - \bar{X}_{ref})^\dagger (X - \bar{X})}{\|X_{ref} - \bar{X}_{ref}\|^2 \|X - \bar{X}\|^2} \quad (4.19)$$

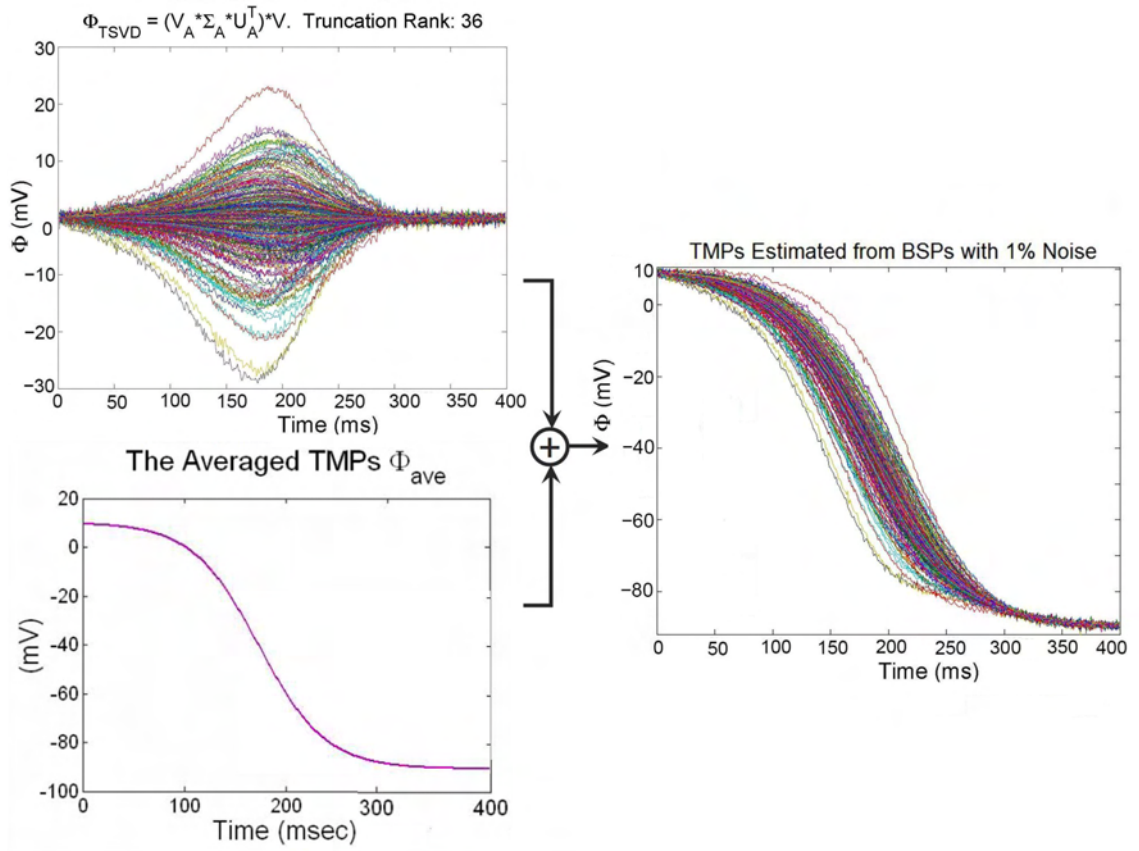


Figure 4.8: TMP waveforms reconstructed under 1% white noise. The reconstruction is achieved by adding regularization results to the averaged waveform.

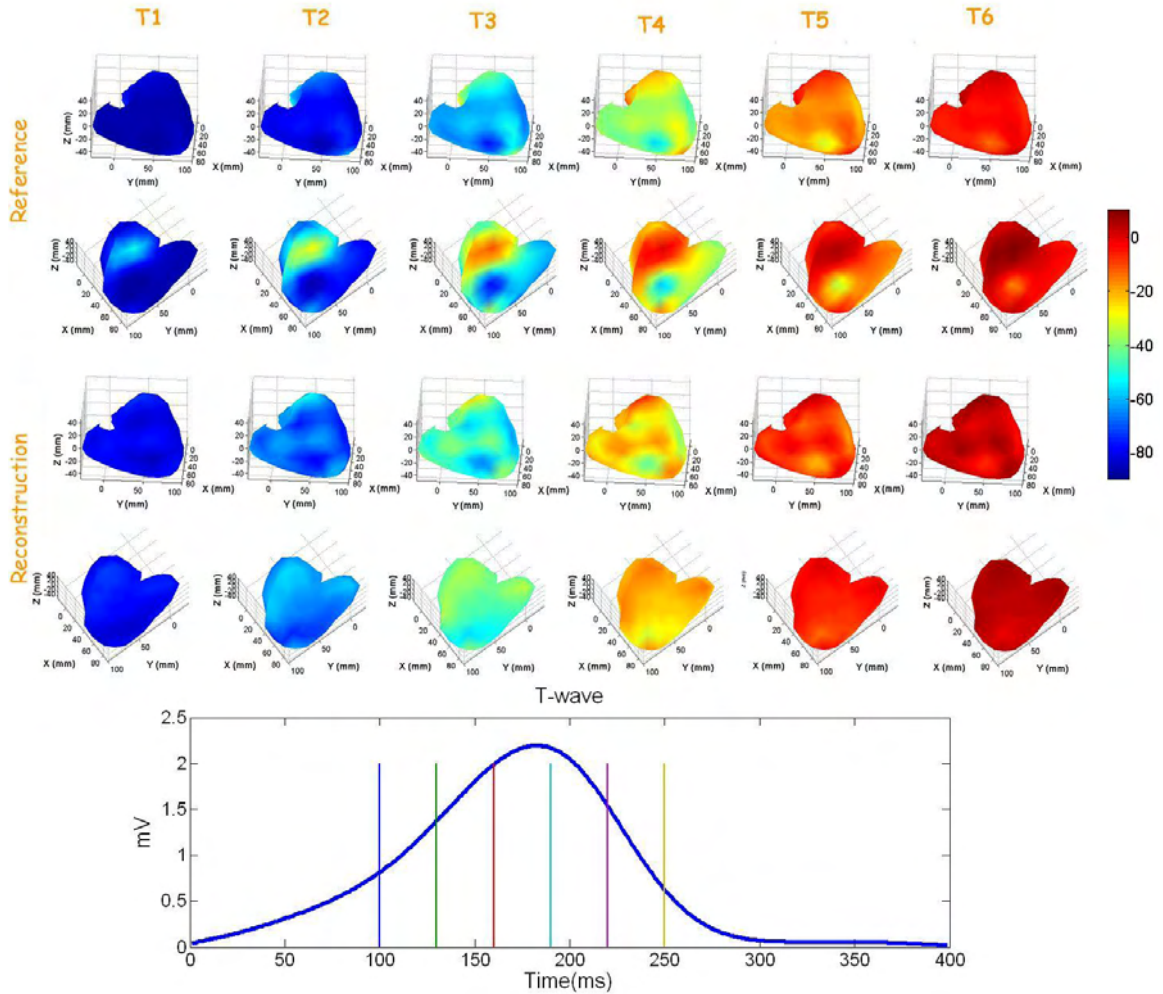


Figure 4.9: With 1% measurement noise, the TMPs are reconstructed by the new approach with 0.119 relative error (RE) and 0.98 correlation coefficient (CC). By taking the snapshots of TMPs at six time instants (T1, T2, T3, T4, T5, T6), we could find that the reference and reconstructed TMPs share the similar pattern during the T wave.

TMPs were reconstructed from noisy BSPs. The corresponding  $\rho$  values were calculated as well. Both the TMPs and  $\rho$  are compared with the references. The resulting RE and CC are listed in the following tables. The RE of TMPs ranges from 3 to 15%; the CC between the reference and reconstructed TMPs are higher than 98%. These results show the advantage in TMP reconstruction with the RWI method compared to the other TMP reconstruction methods. For example, Tilg and coworkers found 31% RE and 91% CC on body surface [70].

In addition to BSPs, epicardial potentials (EPs) were also used as inputs to test the RWI inverse method results. The results suggest that the myocyte TMPs could be reconstructed accurately from EPs ( $RE < 7.3\%$ ;  $CC > 99\%$ ).

Table 4.1: Relative errors (RE) of estimated transmembrane potentials (in percent). TMPs were reconstructed from two sources: BSPs and EPs.

Known	0%	1%	2%	5%	10%
BSPs	$2.7 \pm 0$	$11.94 \pm 0.08$	$13.45 \pm 0.16$	$13.33 \pm 0.17$	$14.76 \pm 0.37$
EPs	$1.45 \pm 0$	$1.91 \pm 0.05$	$2.45 \pm 0.04$	$4.22 \pm 0.07$	$7.09 \pm 0.1$

Table 4.2: Correlation coefficients (CC) of estimated transmembrane potentials (in percent). TMPs were reconstructed from two sources: BSPs and EPs.

Known	0%	1%	2%	5%	10%
BSPs	$99.94 \pm 0$	$98.48 \pm 0.01$	$98.26 \pm 0.02$	$98.26 \pm 0.02$	$98.03 \pm 0.06$
EPs	$99.98 \pm 0$	$99.97 \pm 0$	$99.94 \pm 0$	$99.83 \pm 2e - 3$	$99.53 \pm 7e - 3$

The repolarization timing parameters  $\rho$  were also reconstructed and compared with the reference. The RE and CC of  $\rho$  are listed in the Table 4.3 and 4.4.

Table 4.3: Relative errors (RE) of the repolarization parameter  $\rho$  (in percent). TMPs were reconstructed from two sources: BSPs and EPs.

	0%	1%	2%	5%	10%
BSPs	$6.57 \pm 0$	$10.49 \pm 0.06$	$10.48 \pm 0.02$	$10.59 \pm 0.01$	$11.02 \pm 0.11$
EPs	$5.04 \pm 0$	$4.14 \pm 0.02$	$4.26 \pm 0.03$	$3.57 \pm 0.04$	$4.17 \pm 0.15$



Table 4.4: Correlation coefficients (CC) of the repolarization parameter  $\rho$  (in percent). TMPs were reconstructed from two sources: BSPs and EPs.

	0%	1%	2%	5%	10%
BSPs	$99.84 \pm 0$	$38.14 \pm 0.17$	$34.15 \pm 0.19$	$30.23 \pm 0.24$	$24.80 \pm 0.24$
EPs	$99.93 \pm 0$	$99.84 \pm 0.02$	$99.64 \pm 0.03$	$99.03 \pm 0.06$	$93.62 \pm 0.54$

For the  $\rho$  estimated from the BSPs, the estimation results have low CC with the reference, except for the non-noisy situation. This phenomenon is linked to the spatial regularization applied to the TMP estimates. On the other hand, from the EPs, the  $\rho$  are estimated with significantly lower error because regularization did not require removing nearly as many singular values.

Furthermore, based on the reconstructed TMPs, the epicardial potentials (EPs) were also estimated. The transfer matrix from TMPs to EPs was calculated with the bidomain forward approach. For details, see Chapter 3. The RE and CC of estimated EPs are listed in the following tables.

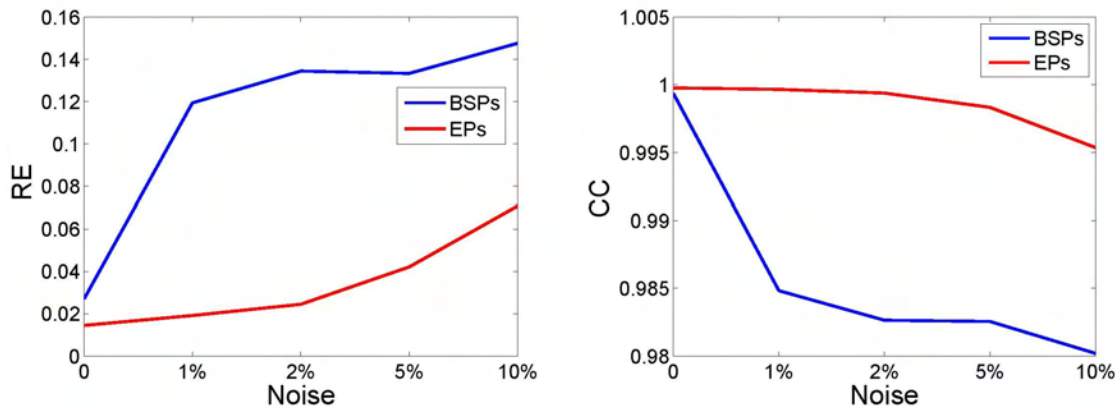


Figure 4.10: The RE and CC between the reconstructed TMP and the reference. Left 1) RE. Right 2) CC.

Tables 4.1, 4.2 and Figure 4.10 present the RE and CC between the reconstructed source potentials and the reference TMPs. These results indicate that, without measurement noise, TMP could be reconstructed with high accuracy, from both the BSPs and EPs. As the noise percentage increased from 1% to 10%, the RE increased slightly



and the CC was reduced slightly. By substituting the EPs for the BSPs as the input of the inverse problem, the RE of TMP reconstruction were dramatically decreased, and the corresponding CC are noticeably increased.

Table 4.5: The relative error (RE) and the correlation coefficient (CC) of the epicardial potentials (EPs) (in percentage). The TMPs are reconstructed from BSPs.

	0%	1%	2%	5%	10%
RE	$0.01 \pm 0$	$93.79 \pm 0.008$	$93.88 \pm 0.006$	$96.18 \pm 0.011$	$98.75 \pm 0.007$
CC	$100 \pm 0$	$36.7 \pm 0.014$	$35.5 \pm 0.013$	$30.3 \pm 0.025$	$22.2 \pm 0.016$

### 4.3.2 Sensitivity of RWI to Geometric Errors

In addition to electrical noise, changes in the heart-torso geometry is another factor that may influence the performance of the inverse approach. Therefore, we used typical changes in heart shape and location to test the RWI method. We extended the heart size by 10% and shifted the heart location  $\pm 1\text{cm}$  along the X-, Y- and Z-axis. These errors are labeled EH10, X1,Y1 and Z1, respectively.

After calculating BSPs  $\mathbf{V}_{\text{ref}}$  in simulation from the reference TMPs  $\Phi_{\text{ref}}$  (Figure 4.3), heart-torso geometry was adjusted and the corresponding transfer matrices calculated. RWI was applied to these transfer matrices and  $\mathbf{V}_{\text{ref}}$  to reconstruct the source TMPs. RE and CC between the reconstructed and the reference TMPs are listed in the Table 4.6. Results suggest that RWI is robust in the presence of geometric error.

Table 4.6: Relative error (RE) and correlation coefficient (CC) of the TMPs estimates (in percent) for errors in heart geometry: An increase in size by 10% (EH10) and shifts in location of X( $\pm 1\text{cm}$ ), Y( $\pm 1\text{cm}$ ) and Z( $\pm 1\text{cm}$ ).

Parameters	EH10	X		Y		Z	
		1	-1	1	-1	1	-1
RE	12.47	13.08	11.71	11.31	11.60	11.15	15.19
CC	98.24	98.28	98.44	98.55	98.50	98.59	97.41

## 4.4 Conclusions

In this study, a new inverse approach called regularized waveform identification (RWI) was developed that combines spatial regularization with temporal optimization to estimate TMPs from BSPs with greater accuracy than conventional regularization alone. TMPs were estimated throughout the T wave, using the realistic ventricle-torso model and heart-surface TMPs of the ECGSIM simulation package. We evaluated the sensitivity of our RWI approach to 1, 2, 5 and 10% electrical noise on the body surface. Relative errors (RE) of <15% and correlation coefficients (CC) >0.98 were found. A 10% enlargement of the heart and position errors of  $\pm 1cm$  in all directions yielded REs of <15% and CCs >0.97. Simulation results showed that this approach performed much better than traditional regularization methods alone and is robust in the presence of noise and geometric error. By incorporating temporal information, in the form of the basic TMP wave shape, estimation accuracy was enhanced while maintaining computational simplicity.

# Chapter 5

## Obese Anatomical Remodeling

### 5.1 Introduction

Myocardial disease is common in Type II diabetics, including elevated risk for myocardial infarction, heart failure, and sudden cardiac death. Both diabetes and obesity, which are widespread among diabetics, contribute to deleterious changes to the heart. Among obese diabetics, obesity itself plays an important role in the heart disease development and clinical diagnosis. To separate the consequences of geometric changes from the consequences of electrophysiological ones, we investigated how changes in cardiac and torso geometry, associated with obesity, affected body-surface electrocardiograms.

Although it is well known that the standard 12-lead set is not specific for diabetes, several previous studies indicate that ECGs recorded among the obese group tend to be different from ones measured from normal subjects. For example, obesity was suspected of causing a significant increase in P-wave and QTc dispersion in a 12-lead ECGs study [94]; obese patients were shown to have significantly more abnormalities on signal-averaged electrocardiograms [54]. Among obese subjects, ECG abnormalities could be caused by either anatomical or electrophysiological remodeling. This chapter is focused on obese anatomical, or so called geometric, remodeling and its effects.

In this study, we are particularly interested in apple-shaped obesity (body fat stored around the abdomen, chest and surrounding internal organs) because people with this body shape tend to have a higher risk of diabetes and heart disease [116, 20]. Several

important changes, in heart and torso anatomical structure associated with obesity include increased thickness of the left ventricular walls, change in the position and orientation of the heart, and enlargement of the abdominal volume. Based on these observations, three obesity associated anatomical features were characterized: 1) left ventricular hypertrophy (LVH), 2) heart displacement, and 3) abdomen enlargement, measured with the waist circumference (WC) [17, 43].

Simulation experiments were devised to evaluate the effect of these three anatomical variations on the body surface potentials (BSPs). Simulations were carried out with the bidomain platform. Our bidomain forward-problem model was used to calculate body-surface ECGs,  $\mathbf{V}$ , from cardiac transmembrane potentials,  $\Phi_{\mathbf{m}}$  using the forward-problem solution  $\mathbf{A}$  (see Chapter 3). As shown in Figure 1.1, the normal cardiac source potentials are generated with the *Bidomain Source Module*; transfer matrices from the source potentials to BSPs were calculated with the *Bidomain Forward-Problem Module* based on normal and obese anatomies.

Obese habitus was characterized by modifying normal heart-torso geometry based on the three obese anatomical characteristics. Specifically, four heart-torso models were generated: 1) a normal heart and in a normal torso, 2) an hypertrophied heart in a normal torso, 3) a displaced heart in a normal torso, and 4) a normal heart in a torso with an extended abdomen. These anatomical models were used as the volume conductors to calculate body surface ECGs with the forward problem module, while the cardiac sources remain unchanged. In other words, the normal source TMPs were common to both normal and obese geometrical models.

From body surface ECGs simulated from both the normal and obese anatomies, we evaluated obese anatomical effects on BSPs. We investigated variations in both the conventional 12-lead system and body surface ECGs during the Q-T interval due to obese habitus. BSP maps provide a comprehensive view of cardiac activity in the 12-lead system. Several analysis methods were used to characterize the BSPs, including the standard deviation, power spectral density, principal component analysis, isopotential and iso-integral mapping. These features were compared on normal and obese torsos. Conclusions drawn from these simulations were tested on measurements made on normal and obese diabetic subjects as described in Chapter 7.

## 5.2 Obese Anatomical Features

In this study, three obese habitus features were considered separately, namely: 1) left ventricular hypertrophy (LVH), 2) heart displacement, and 3) increased abdominal size. Obese heart-torso models were generated by modifying the realistic heart and torso models of the simulation package ECGSIM (see A [111]). A set of MATLAB codes was developed to modify the left ventricular wall thickness, the heart's orientation and position, as well as the torso abdominal size.

### 5.2.1 Left Ventricular Hypertrophy (LVH)

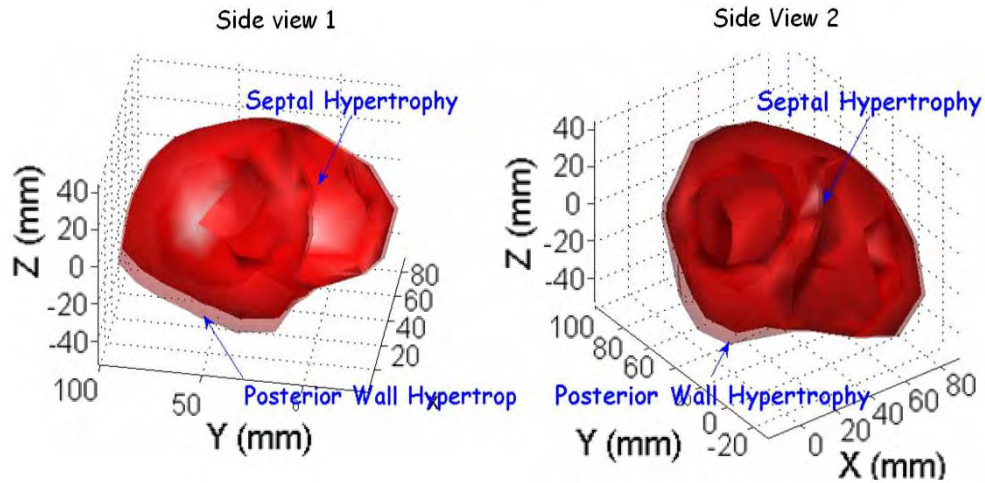


Figure 5.1: Normal ventricle model (opaque red) and 20% left ventricular hypertrophy (LVH) model (transparent red) that encloses the normal one.

Echocardiography measurements show that the obese subjects are vulnerable to left ventricular hypertrophy (LVH). The symptoms include larger left ventricular wall thickness and mass [32, 84, 8, 120]. In addition, compared to non-obese subjects, obese patients have on average 15% to 25% thicker inter-ventricular septums (IVS) and posterior walls (PW). This percentage is even higher among the severely obese group [8, 120].

To simulate obesity-associated LVH effects, algorithms were developed to thicken the IVS and the PW of the given normal ventricle by a set amount. Here, the 3D ventricular model exported from ECGSIM was used as the normal reference. In Figure 5.1, the dark red model presents the shape of the normal reference ventricle, which was exported from ECGSIM; whereas the shadow outside represents the simulated LVH ventricle shell, in which both IVS and PW are thickened 20%. The resulting model is labeled LVH20 heart. The corresponding 12-lead ECGs (see Figure 5.10) and BSPs (see Figure 5.7) were calculated with the *Bidomain Forward-Problem Module* in Figure 1.1.

## 5.2.2 Heart Displacement in Obesity

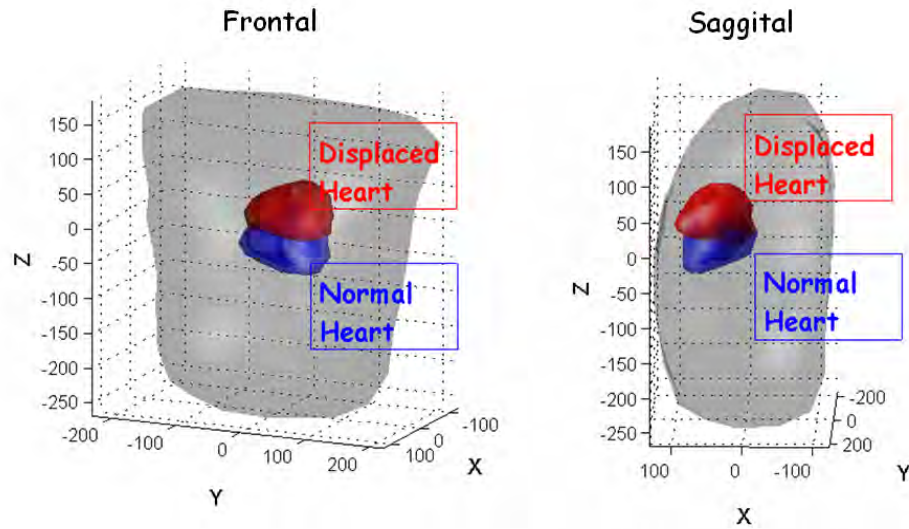


Figure 5.2: Heart displacement caused by obesity. The blue heart model presents the normal heart position. The red one demonstrates the position after displacement.

In addition to LVH, heart position and orientation variation is another important outcome of apple-shaped obesity because the dramatically increased abdominal fat can push the heart up and turn it to a relatively "flat" position. This phenomenon has been observed in our experiment on an obese subject, whose heart was shifted

by 8% of the torso height and rotated by 6, 4.5 and 28 degrees in the coronal, frontal and sagittal planes, respectively, compared to a normal subject. Details of the human subject measurements are given in Chapter 7. Figure 5.2 shows the heart-torso structure variation due to obesity-associated heart displacement (HD).

### 5.2.3 Abdominal Size Enlargement

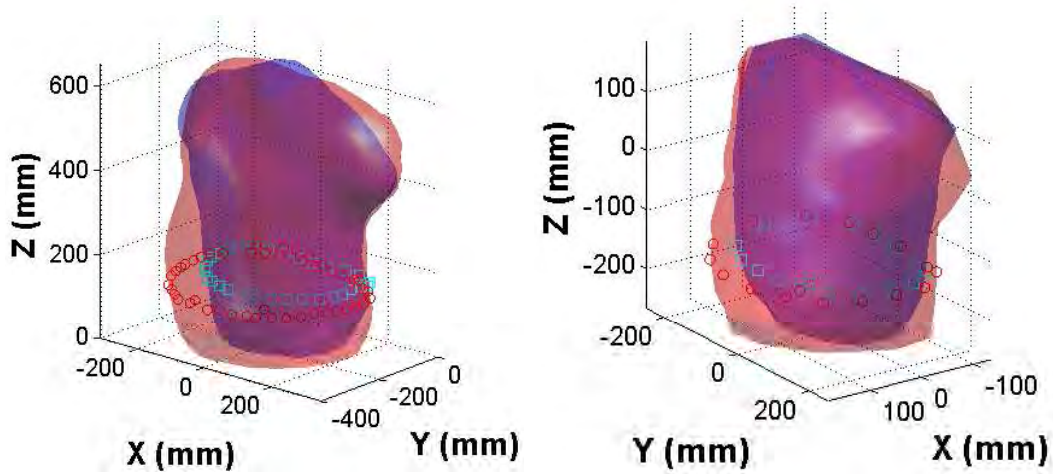


Figure 5.3: Left) normal and obese torsos measured from real adult male subjects. Right) ECGSIM torso and corresponding simulated obese torso (with 16% WC increase). In the figures, the normal and obese waist lines were marked with blue squares and red circles, respectively.

An extended abdomen (EA) is another obese habitus feature considered in this work. Waist circumference (WC) was used to quantify abdominal size. It is a parameter that is easy to measure and compare, and more importantly, it has been used as an indicator for the risk of diabetes and heart disease [17, 43]. We evaluated the WC difference between a normal and an obese subjects. Their torso shapes are shown in the left of Figure 5.3. Based on the WC difference, we increased the normal ECGSIM torso WC by 16%, from 98 cm to 114 cm, to generate the obese ECGSIM torso in the simulation. The resultant torsos are shown in the right of Figure 5.3.

To modify a normal torso into an obese one, in addition to WC, we need a realistic obese torso shape to provide enough detailed information to characterize torso shape.

A set of MATLAB algorithms was designed to simulate the torso enlargement. For details, see Appendix C.

From the anatomical models associated with obesity we calculated their body surface ECGs. By comparing BSPs on these obese model with ECGs from a normal model, we evaluated effects on body surface ECGs of the anatomical changes that occur with obesity.

### 5.3 Effects of Obese Anatomy on BSPs

Effects of anatomical remodeling due to obese habitus are expected to be observed in body surface potentials, even when cardiac sources remain unchanged. Obese anatomy was characterized with three features: left-ventricular hypertrophy, heart displacement and abdominal enlargement. Consequently, comparisons were made among the BSPs simulated under four circumstances: normal heart and torso, 20% LVH heart (LVH20) in a normal torso, displaced heart (DH) in a normal torso, and a normal heart in a torso with 16% enlargement of the abdomen (EA).

We employed several signal processing tools to reveal the spatial and temporal features of the simulated BSPs during QRS complex and T wave. These features from the three obese models were compared to those from the normal one. The spatial standard deviation (SD) gave the effective values of the BSPs as a function of time. Principal components analysis (PCA) was used to decompose the BSPs. The components represent the ranked dynamic. The corresponding analysis was focused on the diagnostic frequency band  $0.05 \sim 100Hz$ , which was specified by the American Heart Association [9]. In addition, isopotential and iso-integral maps were used to present the spatial dispersion of the BSPs. Standard 12-lead ECGs were also simulated for the three forms of obese habitus and compared to simulated 12-lead ECGs on the normal torso with a normal heart. Results of the 12-lead comparisons may help explain why 12-lead ECGs are not specific to diabetes, especially in the presence of obesity.



## Spatial Standard Deviation (SD)

The spatial standard deviations (SD) of BSPs were calculated for the four simulated cases. The SD describes the spatial variation of the BSPs during a time interval. The amplitude of SD represents the effective value of BSPs. To compare SDs from the three obese habitus torsos with the normal reference, we subtracted the normal SD from all cases, the results are shown in Figure 5.4. As expected, the absolute SD differences between normal- and obese-torso BSPs were largest around the peaks of R wave and T wave.

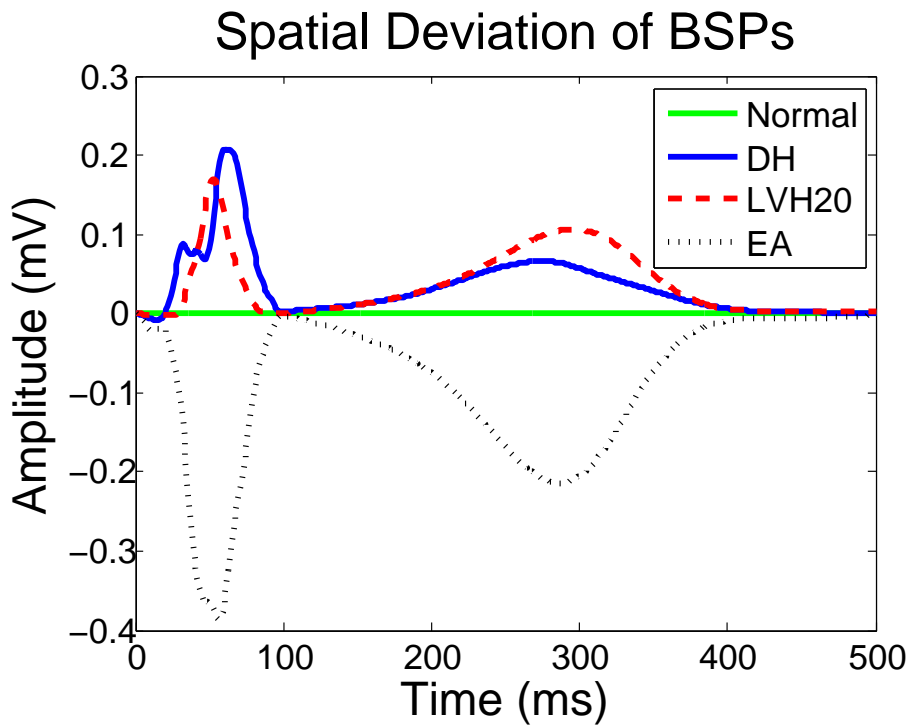


Figure 5.4: Based on the BSPs during QRS-complex and T wave, the differences of spatial standard deviation (STD) between the obese cases and the normal. The normal STD is used as zero reference. The similar demonstration approach appeared in an earlier study [18].

Among the three obese habitus features, the LVH and DH hearts increased the spatial SD; while the EA remodeling decreased the SD. The increases in SD may be associated with anatomical changes that moved cardiac sources closer to the body surface.

EA remodeling moved the body surface farther from the sources, which presumably reduced the amplitude of the resulting ECGs.

### Power Spectra Density (PSD)

BSPs are spatial-temporal signals, which present the electrical signal distribution over the torso surface during the cardiac cycle. To capture the periodicity of the BSP energy distribution, spectrum analysis was used to translate the BSPs into the frequency domain. Means of the spectral magnitudes of the Fourier transforms of the Q-T potentials over the body surface in the three altered geometries were compared to spectra on the normal torso with a normal heart, as shown in Figure 5.5.

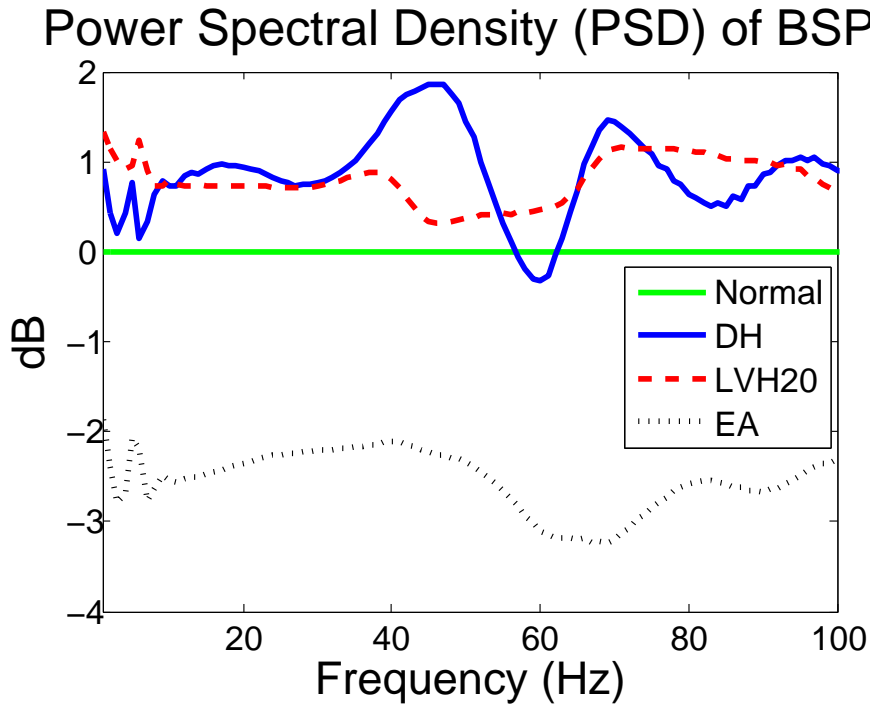


Figure 5.5: The power spectra density (PSD) difference between the obese and normal BSPs during Q-T interval. The normal PSD is used as reference.

In the figure, the power spectral density (PSD), which describes how the power (or variance) of a time series is distributed with frequency. At each frequency, for display only, the magnitudes were adjusted so that normal was always at 0 dB. The changes

relative to normal are similar for the hypertrophied and displaced hearts. The comparison was made in the low frequency band ( $\leq 100$  Hz), where the most of ECG energy locates[9].

Among the three obese habitus features, the DH and LVH20 slightly increased PSD of BSPs with 1dB on average; while the EA decrease spectral magnitudes with  $2 \sim 3$  dB. Similarly to SD, the changes in PSD may be associated with the anatomical changes: the DH and LVH20 reduce the distance between cardiac source and observation points on body surfaces, while the EA remodeling prolonged this distance. Compared with the DH and LVH, the EA has larger impact on ECGs.

### **Principal Component Analysis (PCA)**

To reduce the data dimension and perhaps reveal hidden structures in the BSPs, we performed principal component analysis (PCA). PCA is a well-known linear, data-decomposition technique. It is based on the assumption that the input data set is the linear combination of its basis vectors [99]. PCA is used to remove data redundancy from BSPs by minimizing covariance among channels, and improve signal-to-noise ratio (SNR) by selecting components corresponding to large variances.

Figure 5.6 depicts the first three principal components of the normal- and the three obese-torso BSPs. These components account for the fundamental dynamic information in the BSPs. In the figure, the first three principal components were not changed by the LVH and EA. On the other hand, the DH flipped the second and third principal components, indicating the underlying energy distribution was dramatically changed by DH. The right side of the figure presents the ratios of the principal component coordinates of the three obese cases compared to normal. The LVH and DH respond for coordinates higher than normal, whereas EA reduced coordinate ratio values ( $< -2dB$ ), which were continually dropping while the order increases.

### **Iso-potential Mapping**

An iso-potential map is a measure of the electrical potential over a surface at a specific instant of time. Figures 5.7 and 5.8 capture the iso-potentials at the peak of

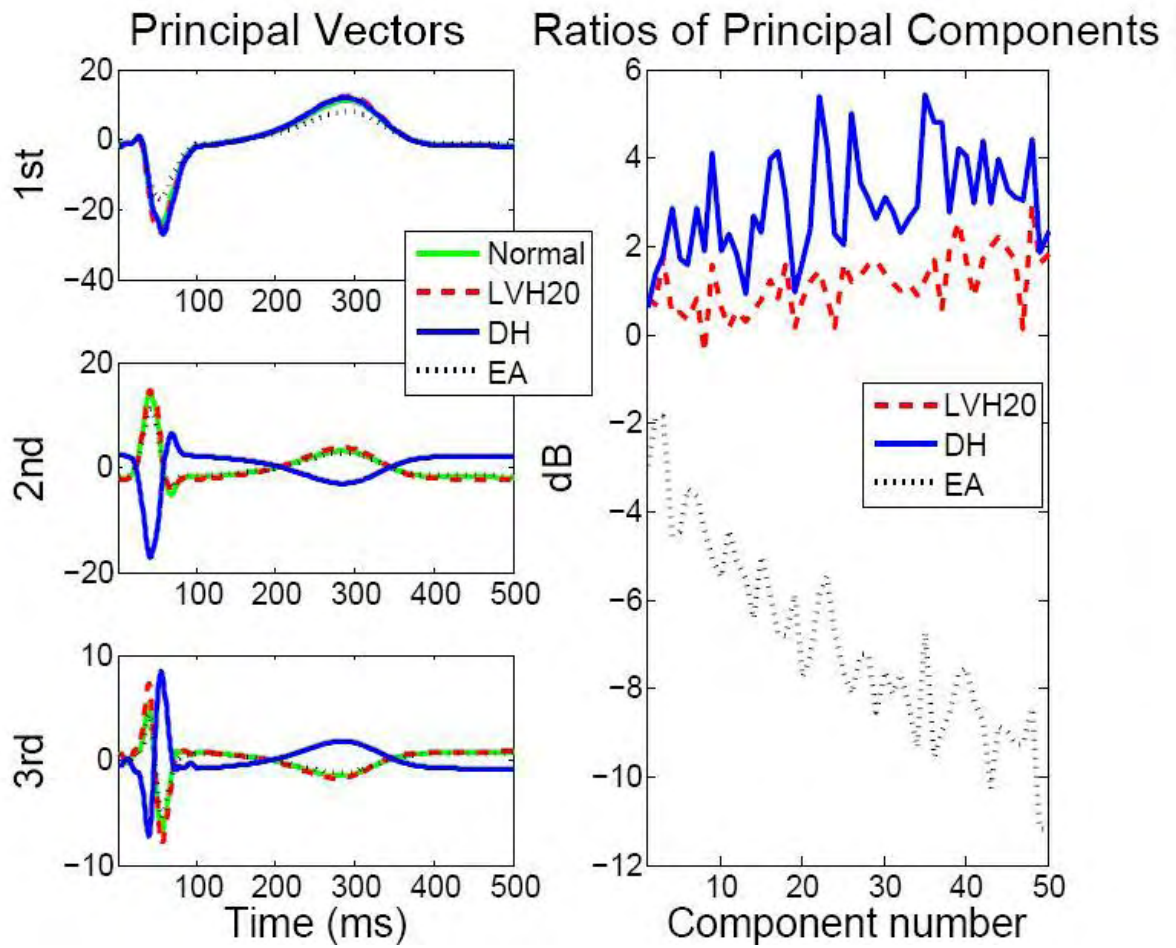


Figure 5.6: Principal component analysis over the cardiac cycle of signal-averaged, BSPs from a normal, LVH20, displaced heart (DH) and extended abdomen (EA) models. Left: the first three principal components. Right) the principal components ratios refer to the normal.

the R-wave and T wave, respectively. These instants account for the highest dynamic energy during depolarization and repolarization of the ventricles. In both figures, the iso-potential maps of the normal, LVH20, DH and EA cases are listed in the clockwise order. From the figures, we could tell the EA reduced the magnitude of BSPs due to the prolonged distance between cardiac source and observation points. At the peak of the R and T waves, there is an area with minimum potential on upper left precordial, and a region with maximum potential on the lower left side of torso. By comparing the locations of minimum and maximum potentials between the DH and normal, we found DH moved BSPs For the case of DH toward upper middle areas of chest, while increased BSP magnitudes on precordial area. This phenomenon represents the shifting and rotation of the cardiac source. Among the three obese habitus, LVH has the least effect on BSPs. The relative errors of the iso-potential maps are summarized in Table 5.1.

### **Iso-integral Mapping**

ECGs during QRS complex are determined by depolarization TMPs; while ECGs during T wave are mainly dominated by repolarization TMPs. In 1934, Wilson used QRST area of body surface ECGs to define the ventricular gradient [29]. In this study, we calculated iso-integral maps over Q-T interval for the four groups: one normal and three obese heart-torso models. The integral maps were obtained by calculating for each lead the algebraic sum of all instantaneous potentials from the wave onset to the wave end multiplied by the sampling interval.

Results are shown in Figure 5.9. For the normal, LVH20 and EA cases, maximum potentials appeared on the center of left anterior chest. Due to the change of distance between heart and torso surface, the overall iso-integral potentials were increased by the LVH20 and decreased by the EA. Due to the movement of the heart inside the torso, the maximum region of iso-integral potential is shifted to the superior central area of the torso for the DH case. The similar phenomenon has appeared in the previous isopotential maps, indicating the effects of obesity habitus on ECGs are relatively consistent during Q-T interval. Relative errors over the body-surface during the Q-T interval are listed in Table 5.1.

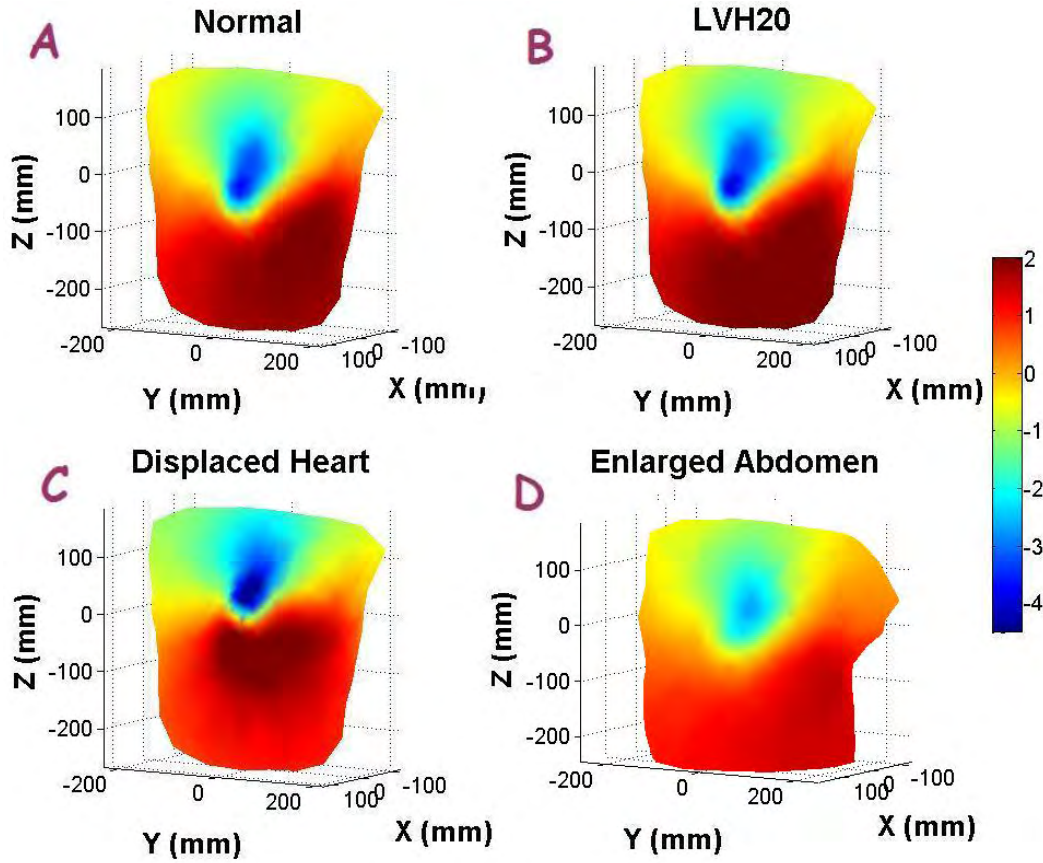


Figure 5.7: Anterior BSP maps at the peak of R-wave. A) with the normal heart, B) with the LVH20 heart, C) with the displaced heart (DH), D) with the extended abdomen (EA) torso.

Table 5.1: The relative error (RE) of BSPs at the peaks of R and T wave and during Q-T interval for the three obese habitus: 20% LVH (LVH20) heart, displaced heart (DH) and extended abdomen (EA) models. The normal BSPs are used as the reference.

Parameters	20%LVH	Displaced Heart	extended Abdomen
R-peak	0.10	0.92	0.32
T-peak	0.13	0.72	0.31
QT-interval	0.12	0.68	0.30

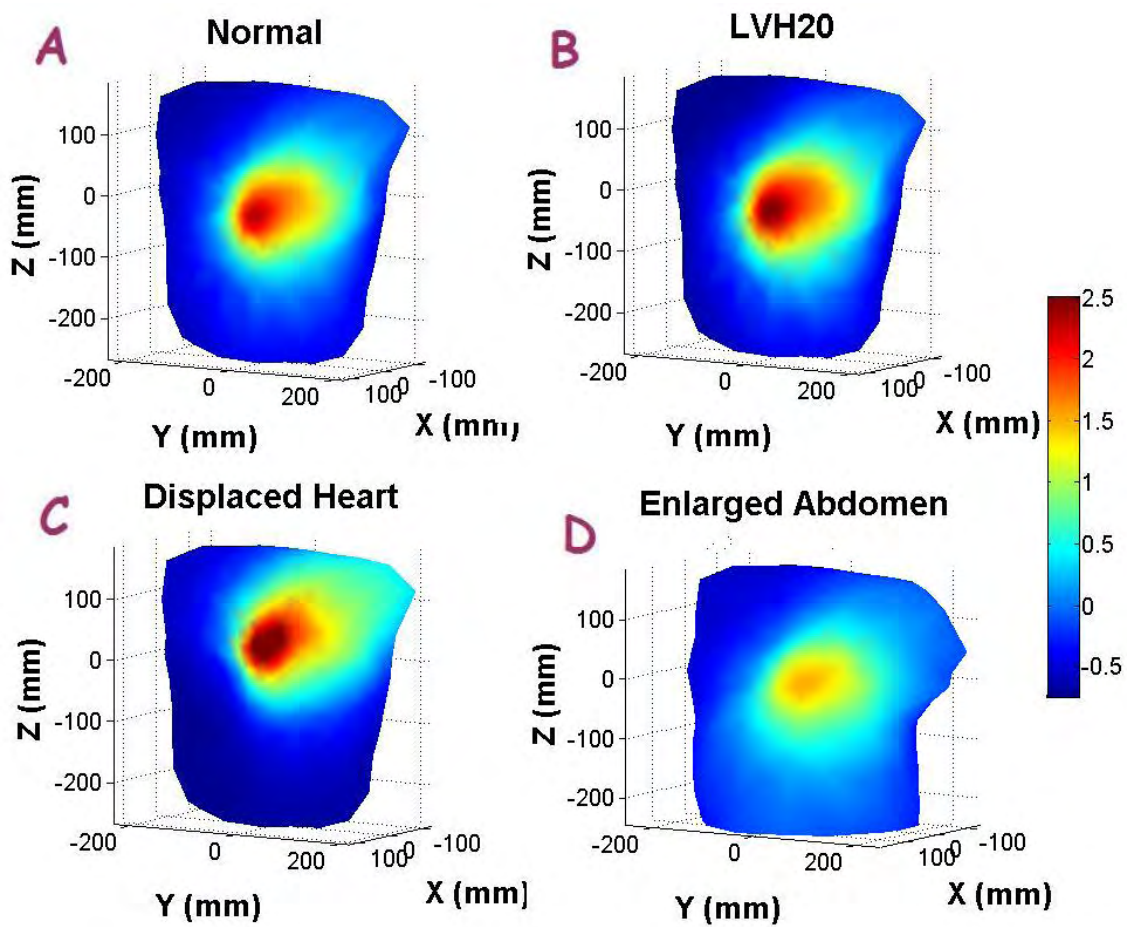


Figure 5.8: Anterior BSP maps at the peak of T wave. A) with the normal heart, B) with the LVH20 heart, C) with the displaced heart (DH), D) with the extended abdomen (EA) torso.



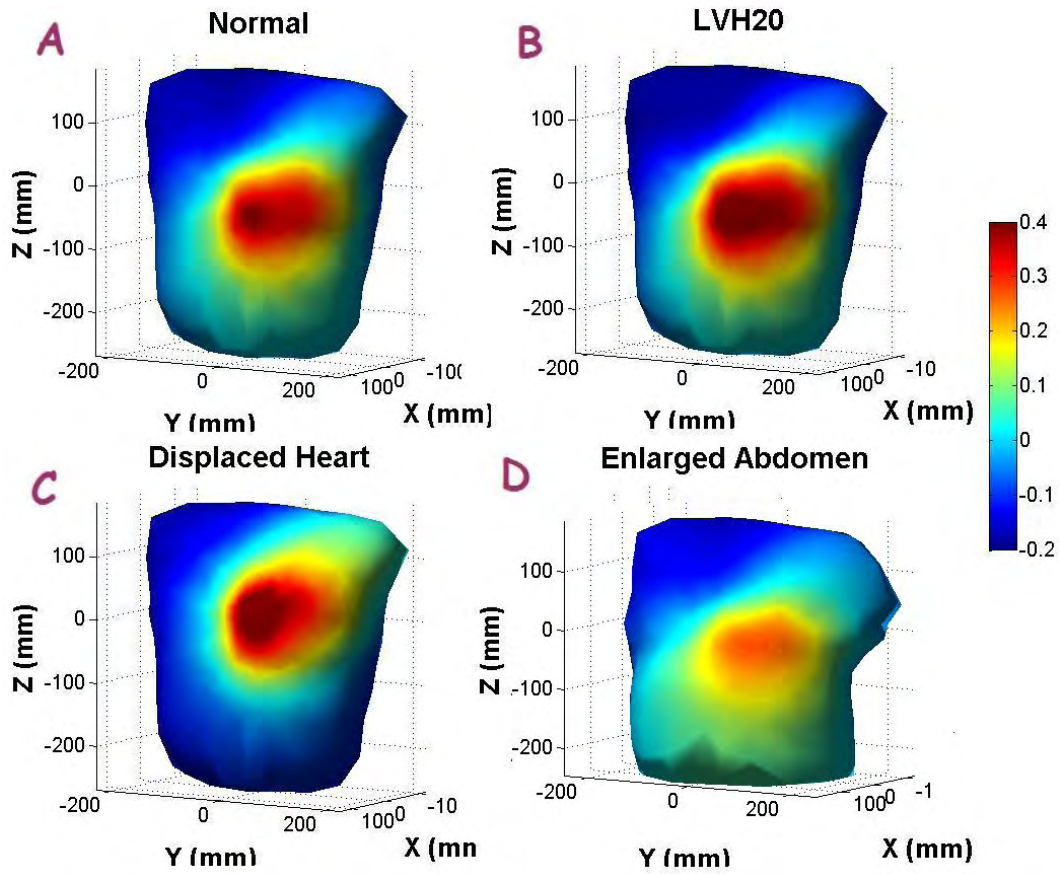


Figure 5.9: Anterior iso-integral maps over the Q-T interval on the body surface. A) Normal heart, B) LVH20 heart, C) Displaced heart (DH), D) extended abdomen (EA) torso.



## Standard 12-Lead ECGs

In addition to BSPs, the standard 12-lead ECGs are also employed due to their prevalence in clinical diagnosis. Out of the twelve leads, there are only eight independent signals, including any two of the limb leads and the six precordial leads (V1-V6). Waveform changes and pattern shifts of electrocardiographic potentials with obesity is clearly seen in the four precordial leads during T wave, as shown in Figure 5.10. It is especially important to identify effects of obese geometry on the T wave because they may confound T wave changes seen in diabetics [25]. Relative errors with heart displacement over the T wave in the precordial leads V3 to V6 were 117, 98, 74, and 44 %, respectively. The mean relative error was 83%.

In Figure 5.10, the LVH slightly increased the amplitudes of T wave recorded with precordial leads. The EA decreased the T wave amplitudes. The DH dramatically decreased all potentials measured with leads V3-V6, because the cardiac source was shifted away from left precordial area due to heart displacement associated with obesity. For details, see Figure 5.8.

However, we should be very careful with the 12-lead ECG measurements. Both the isopotential and iso-integral maps (Figure 5.7, 5.8 and 5.9) suggested the obese-related geometrical changes of heart and torso could lead to big distortions of potentials over precordial area. These distortions may raise some difficulty into 12-lead ECG interpolation.

## Relative errors and correlation coefficients

Finally RE and CC were calculated to quantify both temporal and spatial differences in BSPs caused by the three obese habitus features. The results are recorded in Table 5.2. Taking the normal as the reference, the DH model shows the highest RE and lowest CC, followed by the EA model. Both LVH20 and EA BSPs demonstrate fairly high CC with the normal.

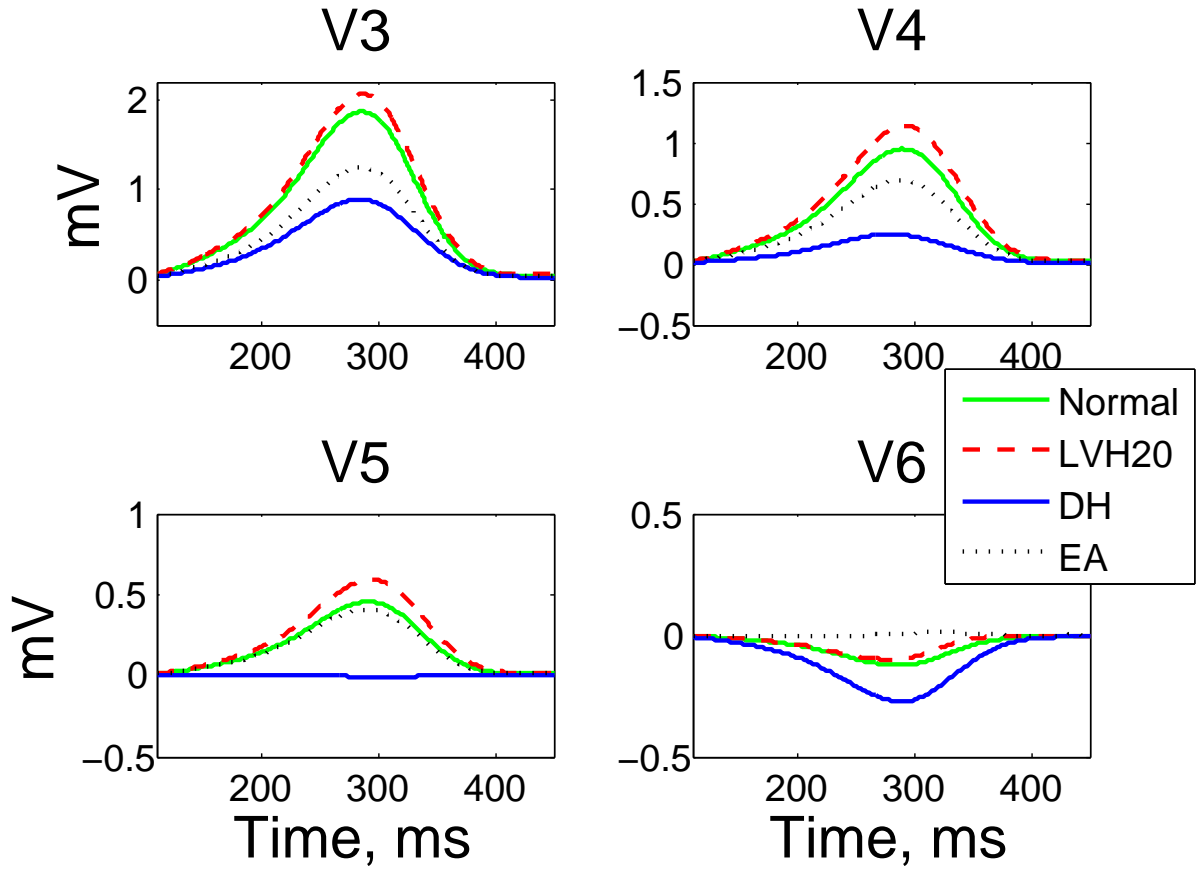


Figure 5.10: Independent measurements in the standard 12-lead ECG set during T wave from the Normal (green solid), LVH20 heart, Displaced heart (DH), and extended abdomen torso (EA).

Table 5.2: The relative error (RE) and correlation coefficient (CC) of BSPs for the three obese habitus: 20% LVH (LVH20) heart, displaced heart (DH) and extended abdomen (EA) models. The normal BSPs are used as the reference.

Parameters	20%LVH	Displaced Heart	extended Abdomen
Relative error	0.1261	0.8157	0.3189
correlation coef.	0.9980	0.7018	0.9785

## 5.4 Discussions and Conclusions

For this study, we modified the realistic heart and torso models of the simulation package ECGSIM. Body-surface potentials were calculated from transmembrane potentials on the heart surface and studied using spectral and principal-component analysis and iso-potential and iso-integral maps. We found relative errors over the body-surface during the Q-T interval of 12, 32, and 82% for hypertrophy of the heart, extension of the abdomen, and heart displacement with obesity, respectively.

In addition to BSPs, standard 12-lead ECGs were simulated for the normal and three obese anatomies. The major change to the standard 12-lead set occurred with heart displacement. The mean relative error over the T wave in the precordial leads V3 to V6 was 83% with heart displacement. These results demonstrate the limitations of using standard lead sets to characterize electrocardiographic changes in obese subjects and point to the need for more comprehensive measures, such as body-surface mapping and inverse electrocardiography, to describe electrical remodeling in obesity and diabetes.

Our results suggest that geometric changes accompanying obesity may have a significant effect on electrocardiograms that may be confused with electrophysiologic changes due to diabetes. An understanding of the geometric effects is essential to distinguishing changes that occur due to obesity from those due to diabetes.

Electrocardiographic features among diabetic and obese cohorts are only beginning to be studied. Further investigative effort is necessary. During these simulation studies, the increase of fat tissue has not been fully characterized. Fat resistivity is higher than the regular muscle's, and it may lead to an additional potential reduction on the anterior surface. Although some nuance may be lost with this simulation study, it allows us to detect the effects of obese habitus and get the initial ideas on ECG patterns in obesity. The approach and results used here can be used as reference for future work. In addition, the simulation platform can be applied to other electrophysiology studies.

# Chapter 6

## Diabetic Electrical Remodeling

Type II diabetes is a major elevator of the risk of heart diseases, including myocardial infarction, heart failure, and sudden cardiac death. Although the value of electrocardiogram (ECG) in investigating effects of diabetes on the heart has been realized, the prognostic value of ECG abnormalities in diabetics has not been fully studied and characterized. In this Chapter, we focus on the electrical phenotype of diabetes, represented as body-surface potentials (BSPs) and cardiac myocyte transmembrane potentials (TMPs).

TMPs are the differences between intra- and extra-cellular potentials. Changes have been found in the ion channel currents across myocyte membranes in several diabetic animal studies [77, 21, 122, 14, 46]. Results suggest that, in diabetic rats, ion currents  $I_{to}$ ,  $I_{ss}$ , and  $I_{Kr}$  were reduced during repolarization, which leads to action potential duration (APD) prolongation. The action potential (AP) signals the depolarization and repolarization of the transmembrane potential (TMP) of a cell. In this study, we used TMP changes in myocytes to characterize electrical remodeling due to diabetes.

Based on results from diabetic animals, diabetic TMPs in humans were simulated by prolonging the duration of normal source potentials. Normal potentials were constructed from the dominant T wave [106] and timing parameters exported from ECGSIM [111]. For details, see Section 3.3.1. From these normal and diabetic source potentials, we calculated the corresponding normal and diabetic BSPs with the *Bidomain Forward-Problem Module* developed in Chapter 3. By comparing diabetic BSPs with the normal one, we explored the sensitivity of body-surface ECGs to diabetic electrical remodeling.

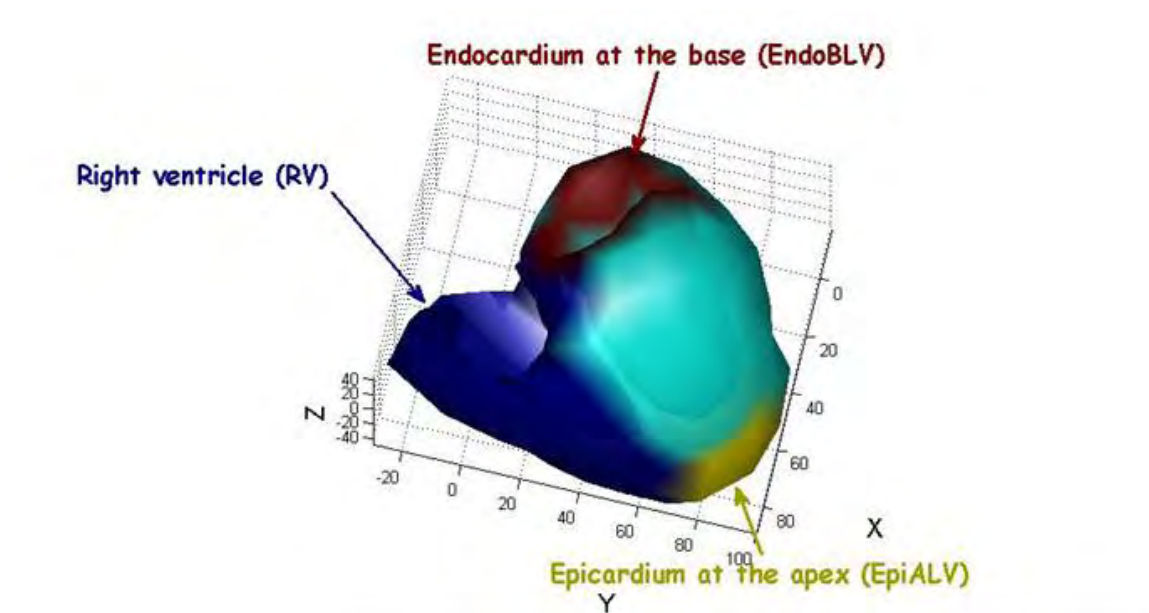


Figure 6.1: ECGSIM ventricle model, marked at three regions: the whole wall of the right ventricle (RV) (in blue), the subepicardium at the apex (EpiALV) (in yellow), and the subendocardium at the base (EndoBLV) (in red). In these regions, unproportionate APD increase was found in a diabetic rat study [21].

As high-dimension signals, the BSPs provide a comprehensive view of cardiac activity with higher spatial resolution than the standard 12-lead set. As in Chapter 5, several analysis methods and features were used to characterize the BSPs, including standard deviation (SD), power spectral density (PSD), principal component analysis (PCA) and isopotential maps. These features were calculated and compared in the normal and diabetic cases. Conclusions drawn from these simulations were tested on measurements made on one normal and one obese diabetic subject as described in Chapter 7.

## 6.1 Diabetic Electrical Remodeling for TMPs

Certain pathological aspects of the diabetic heart have been found to be common to both human and animal models, including electrocardiographic changes such as Q-T and QRS prolongation [23, 88]. In this chapter, we simulated the human diabetic

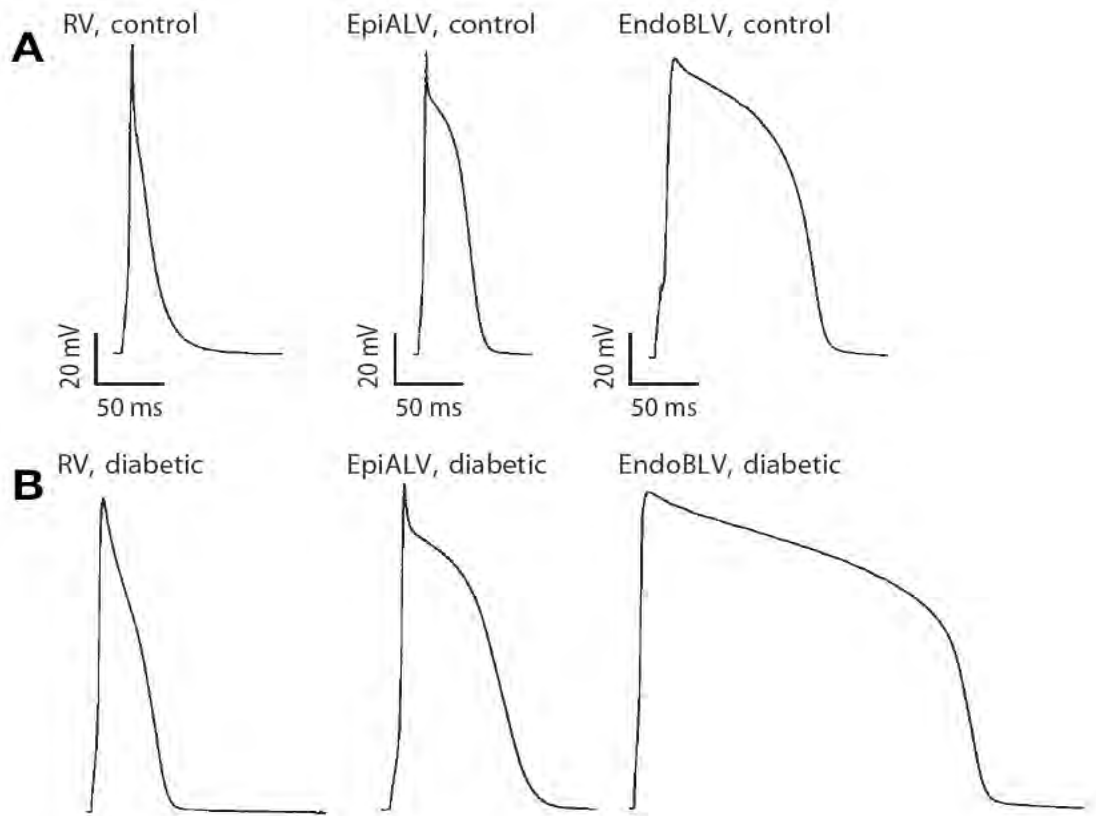


Figure 6.2: Transmembrane potential measured in cells isolated from RV, EpiALV and EndoBLV regions on ventricles of A) normal and B) diabetic rats (Casis and coworkers, 2000 [21]).

heart based on the TMP pattern found in a study on streptozotocin-induced Type 1 diabetic rats, because of the limited availability of animal data for Type 2 diabetes [21].

Among the diabetic rats with Type 1 diabetes, the APD increase differed in three regions of the ventricle. The three regions are: 1) total right ventricle (RV), 2) subepicardium at the apex of the left ventricle (EpiALV), and 3) subendocardium at the base (EndoBLV). We marked these regions on the ventricular model exported from ECGSIM, as shown in Figure 6.1. The APD measured after 90% of repolarization ( $APD_{90}$ ) was found prolonged by 80%, 125% and 148% in the above areas. Figure 6.2 illustrates the TMPs on the above regions in normal and diabetic rats [21].

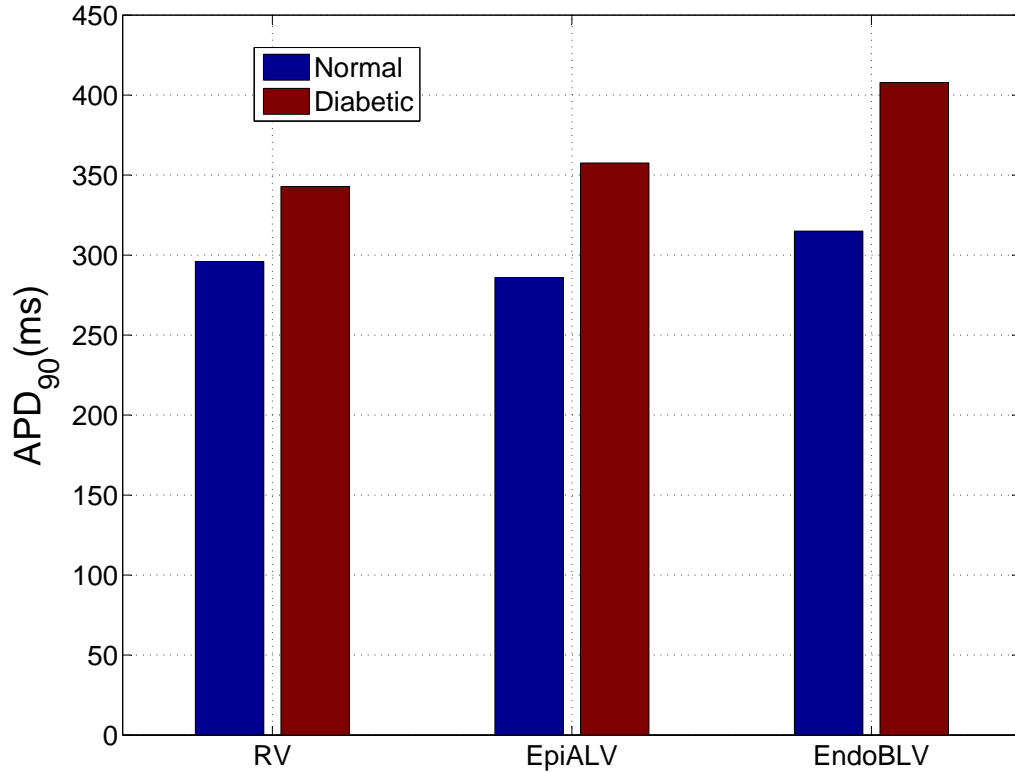


Figure 6.3: In simulation,  $APD_{90}$  of diabetic subject is 15.84%, 25.02% and 29.48% longer than normal, in the areas of RV, EpiALV and EndoBLV.

To apply the findings in diabetic rats to a human study, we multiplied the APD changes in the rat by 0.2. This factor was chosen relative to the normal pulse rates of human and rat. According to American Heart Association (AHA), a normal human heart resting rate is 60 ~ 80 times a minute[115]. Data from Yale Animal Resources Center indicate normal heart rate for rat ranges 330 ~ 480 beats per minute[123]. The resulting 16%, 25% and 29% changes were used as APD prolongation percentages for the RV, EpiALV and EndoBLV areas of a human ventricle, respectively. By adjusting normal AP duration by these percentages, we get diabetic TMPs used in the simulation studies. The normal TMPs were generated with the *Cardio-myocyte Transmembrane Potential Estimation Module* based on ECGSIM TMP timing parameters. For details, see Section 3.3.1. Figure 6.3 compares average  $APD_{90}$  values of the simulated TMPs used to represent normal and diabetic subjects.

In the following section, body surface ECGs generated by normal and diabetic hearts are compared. To evaluate effects of diabetic TMP changes on BSPs, we used the *Bidomain Forward-Problem Module* to calculate the transfer matrix  $\mathbf{A}$ , which maps heart surface TMPs onto body surface. Heart and torso models exported from ECGSIM platform were used as normal anatomy. To separate anatomical effects from electrical ones in order to simplify the problem, the ECGSIM normal heart-torso anatomy was used in both diabetic and normal cases. The only differences between the models were the heart surface TMPs.

## 6.2 Effects of Diabetic Electrical Remodeling on BSPs

Diabetes has been associated with changes in BSPs [23, 88, 21, 46]. In this section, we evaluated the changes in BSPs due to diabetic electrical remodeling, represented as regional APD prolongation on the ventricular surface. The diabetic and normal BSPs were calculated from the corresponding TMPs with the *bidomain forward module*.

We employed several signal processing tools to reveal the spatial and temporal features of the simulated BSPs during QRS complex and T wave. These features were compared in the normal and diabetic cases, as was done in the habitus study of Chapter 5. The spatial standard deviation (SD) was used to evaluate changes in BSP effective values. Principal components analysis (PCA) was used to decompose the BSPs. Power spectral densities (PSD) were found to represent signals in the frequency domain. The corresponding analysis will be focused on the frequency band of  $0.05 \sim 100Hz$ , where most of the ECG energy is located[9]. Iso-integral maps were used to present the depolarization and repolarization differences in BSPs. Several clinical studies have indicated that the Q-T interval of the ECG could be influenced by diabetes. In this section, we also compare Q-T intervals in normal and diabetic cases.



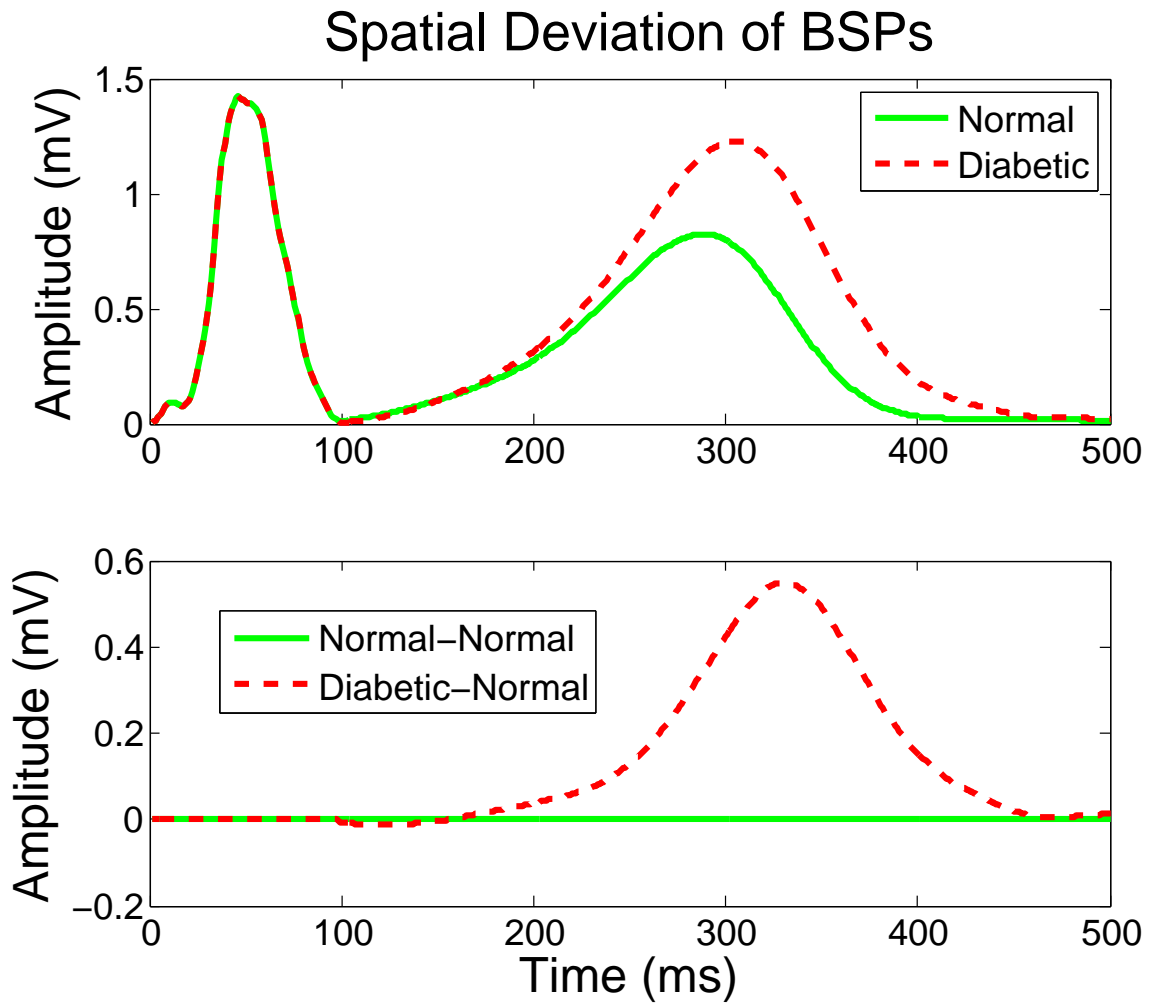


Figure 6.4: The spatial standard deviation (STD) of the normal and diabetic BSPs, during QRS-complex and T wave. The normal STD is used as zero reference. The similar demonstration approach appeared in an earlier study [18].

## Spatial Standard Deviation (SD)

Spatial standard deviations (SDs) of BSPs were calculated for simulated normal and diabetic BSPs. They describe the spatial variation of the BSPs. The amplitude of SD represents the effective value of BSPs at each time instant. To highlight the differences between normal and diabetic BSPs, we subtracted the normal SD from diabetic one, and the results indicate that the effective value during T wave is dramatically raised by APD prolongation in the diabetic case, as shown in Figure 6.4. Based on these results, we may expect diabetic subjects have a different T wave pattern due to the changes of APD related to diabetes. Later, we will test this comment with BSPs from real subjects. For details, see Chapter 7.

## Power Spectra Density (PSD)

BSPs are spatial-temporal signals which represent the electrical distribution over the torso surface during certain periods of time. To capture the harmonic content of the BSP energy distribution, spectrum analysis was used to transfer the BSP signals into the frequency domain. Power spectral density (PSD) describes how the power (or variance) of a time series is distributed in the frequency domain. Means of the spectral magnitudes of the Fourier transforms during the Q-T interval from diabetic BSPs were compared to spectra from normal BSPs.

Figure 6.5 demonstrates the PSD of normal and diabetic BSPs. At each frequency the magnitudes were adjusted so that normal was always at 0 dB. The results suggest that the prolongation of APD cause an increase of the PSD of BSPs in low frequencies (especially  $\leq 10Hz$ ). By putting Figure 6.5 and 6.4 together, we could tell the information they demonstrated are consistent. The major smooth change of SD occurred during T wave, contributing to changes in low frequency range; while fractional changes of SD happened before and after T wave, corresponding to ripples in a relatively high frequency range.

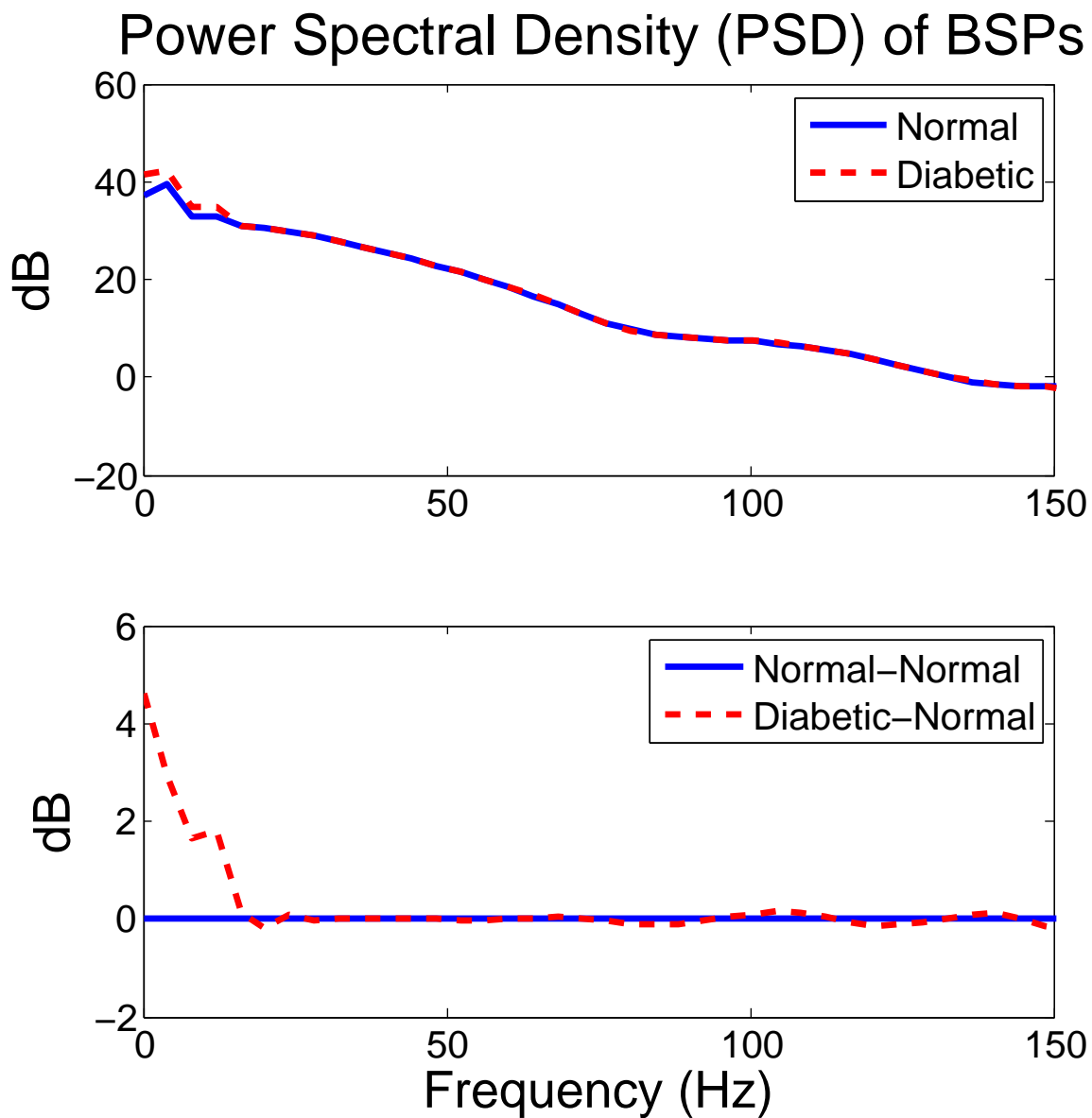


Figure 6.5: The power spectra density (PSD) of the normal and diabetic BSPs during Q-T interval. The normal PSD is used as reference.

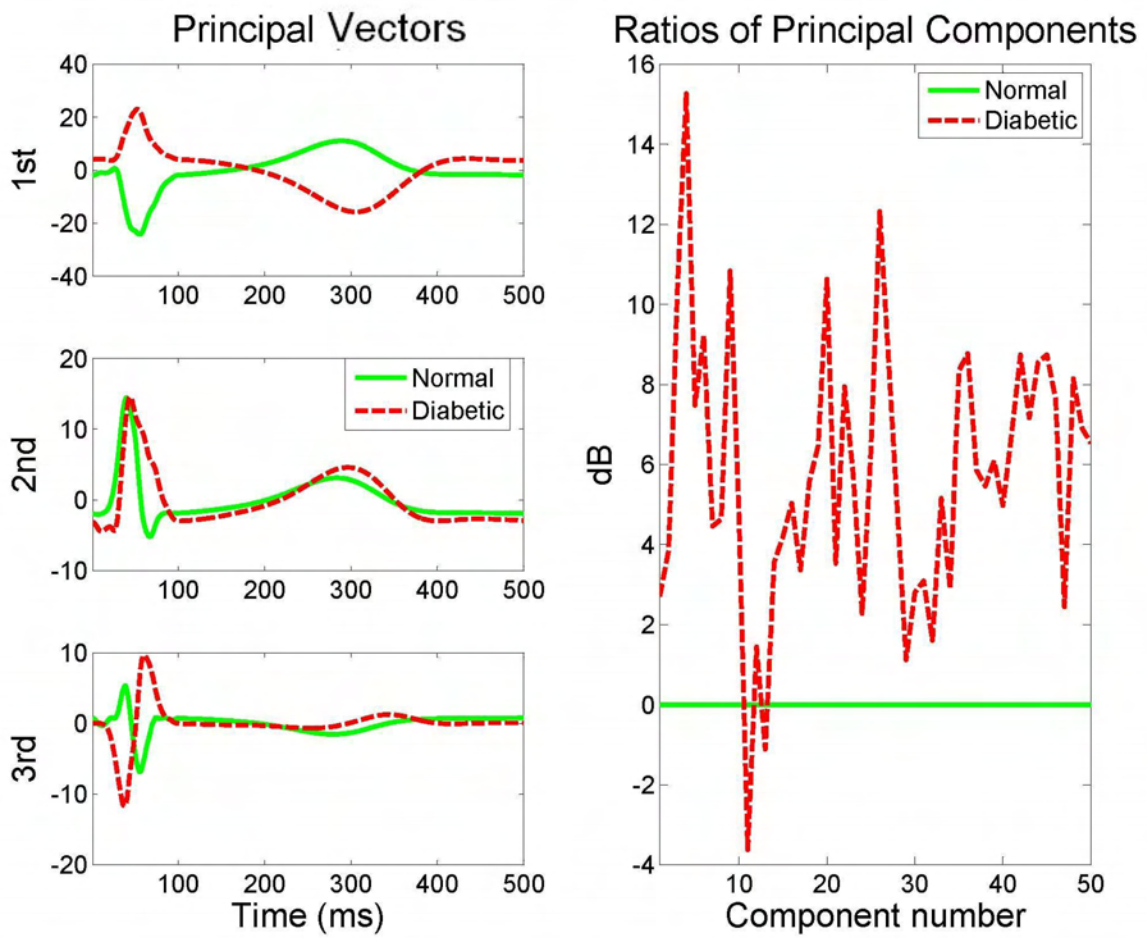


Figure 6.6: Principal component analysis of normal and diabetic BSPs. Left: the first three principal components. Right) the principal components ratios refer to the normal.

## Principal Component Analysis (PCA)

To reduce the data dimension and perhaps reveal hidden structures in the BSPs, we applied principal component analysis (PCA), a well-known linear data decomposition technique. The technique is based on the linear assumption, i.e. the input data set is the linear combination of its basis vectors [79]. PCA was used to remove data redundancy from BSPs by minimizing covariance among channels, and improve signal-to-noise ratio (SNR) by selecting components with large variances.

Figure 6.6 shows that for diabetic BSPs, Q-T interval prolongation occurs in the first three principal components that account for most of the fundamental dynamic information in the BSPs. The change in the ratios of principal components is up to 14 dB in the diabetic compared to the normal. In the left side of Figure 6.6, we can tell that significant changes happened during QRS complex on body surface, which indicates the changes of the TMP shape (associated with APD prolongation) go all the way back to the repolarization phase. On the other hand, these BSPs changes during QRS have not been found in Figure 6.5 and 6.4; this means, unlike during T wave, during QRS complex BSP changes do not involve energy changes.

## Q-T Interval

Q-T interval is another important ECG feature that has been investigated as an indicator for diabetes [38, 85, 24]. Instead of using Q-T itself, we evaluated the corrected Q-T value (QTc) for both subjects. Here, the QTc is calculated from QT with a standard clinical correction, Bazett's formula,

$$QTc = \frac{QT}{\sqrt{RR}}. \quad (6.1)$$

in which,  $RR$  is the interval between the peaks of two R-waves. It represents the heart rate. QTd reflects the underlying heterogeneity of ventricular repolarization. In contrast to most clinical QT studies, we used BSPs rather than the standard 12-lead ECGs to calculate the QTc.

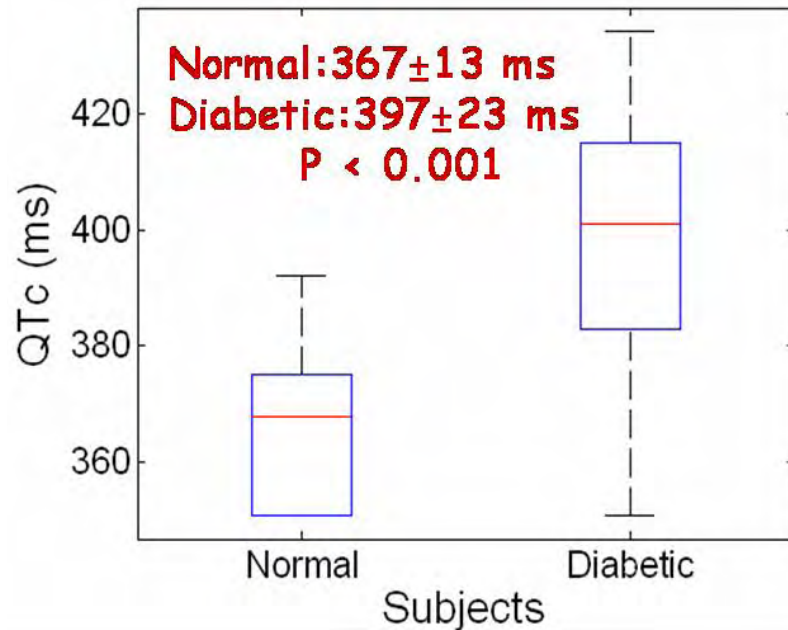


Figure 6.7: The distribution of QT corrections (QTc) on body surface.

Figure 6.7 demonstrates the QTc distributions based on the BSPs of both the normal control and diabetic subjects. The results indicate there is significant difference in QTc between the normal and diabetic subjects, with  $p < 0.001$ .

### Iso-potential Mapping

An iso-potential map is a measure of the electrical potential over a surface at a specified instant in time. This technique uses the ECG data to obtain a map as the projected current image on the torso surface from the heart. The spatial derivatives indicate the contours of the electrostatic field. In this study, we calculated the isopotential at the peak of T wave, which accounts for the largest energy measured on body surface during repolarization, as shown in Figure 6.8.

By comparing the isopotential maps of normal and diabetic subjects side by side, we determined that the uneven temporal changes on the heart surface have a spatial impact on body surface. The correlation coefficient between the normal and diabetic BSPs was 0.43, and the relative error is 125%. In the figure, the diabetic BSPs show a

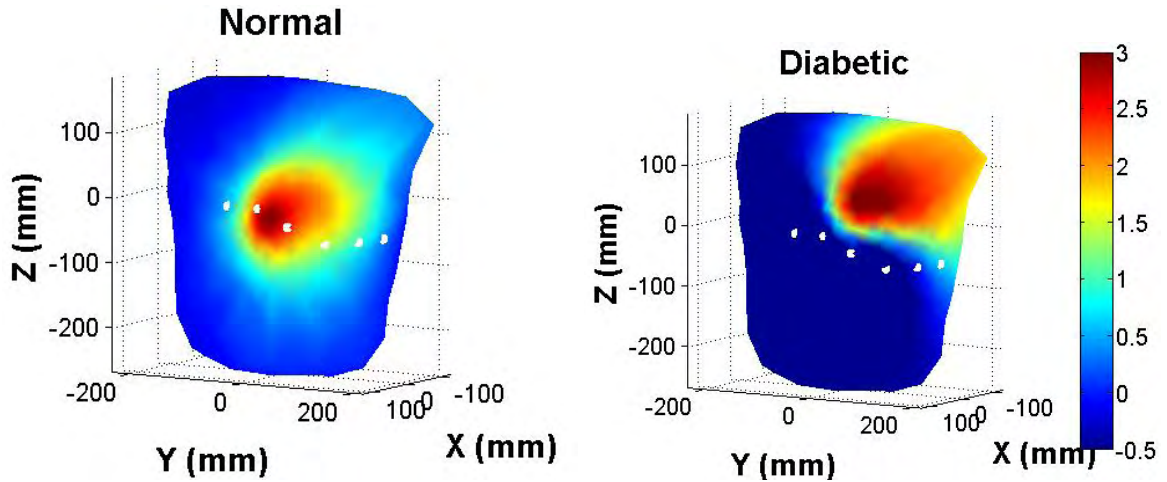


Figure 6.8: Anterior BSP maps at the peak of T wave. The white dots mark the locations of precordial electrode. The correlation coefficient between the normal and diabetic BSPs are 43.12%. The relative error is 124.82%.

higher potential diversity in space. At the same time, the maximum potential region of diabetic BSPs were shifted towards the left shoulder. As we can see, this pattern change will cause dramatic distortion in 12-lead ECG measurement. The white dots in figures represent the locations precordial electrodes in 12-lead ECG system.

### Standard 12-Lead ECGs

In addition to BSPs, the standard 12-lead ECGs were also employed because of their prevalence in clinical diagnosis. Of the twelve leads, only eight are independent. Here, we choose two limb leads (I, II) and six precordial leads (V1-V6), as shown in Figure 6.9. Dramatic changes occurred in 12-lead ECGs due to the APD prolongation associated with diabetes. As expected, an obvious delay of the T wave was found, especially in lead II of diabetic. In addition, compared with normal, precordial leads measurements were inverted in the diabetic case. These results can be explained with Figure 6.8, in which the maximum potential region of diabetic BSPs were shifted towards the left shoulder, the potentials on front chest area were reduced to negative, while the potentials on left side of chest were slight increased to positive.

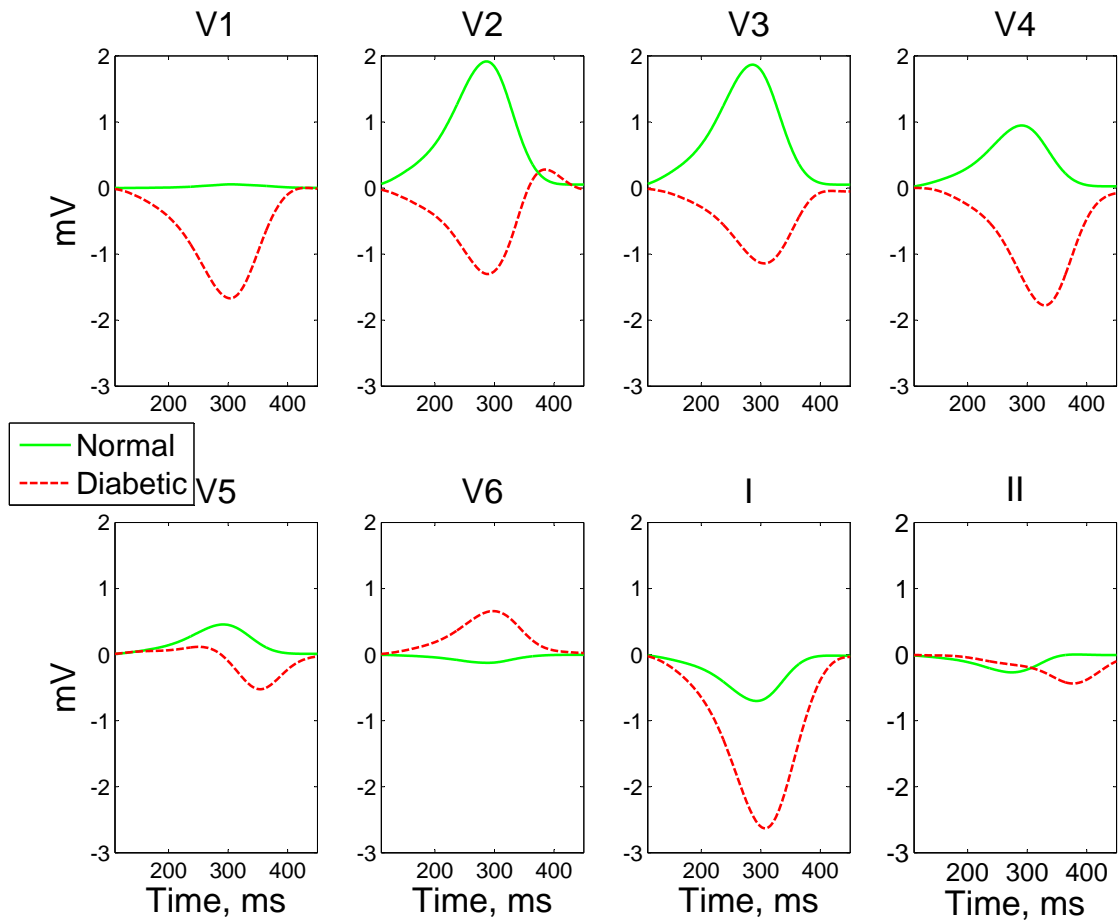


Figure 6.9: Standard 12-lead ECG during T wave of normal and diabetic BSPs.



## 6.3 Discussions and Conclusions

In this work, diabetic electrical remodeling was characterized as regional APD prolongation based on findings in diabetic animal studies. The resulting diabetic BSPs were generated with the *Bidomain Forward Platform* developed in Chapter 3. The influence of diabetic remodeling on BSPs was revealed by comparing normal and diabetic BSPs in simulation.

Results show that APD prolongation that might be associated with diabetes has a large effect on BSPs. By increasing APD by 16, 25 and 29% in three ventricle areas, we can expect about 125% relative error (RE) in ECGs on body surface. At the same time, the Q-T interval increased in both BSPs and lead II ECGs. These results match findings in several earlier studies on diabetic ECGs [23, 88] and support the hypothesis that Q-T interval may increase among diabetics.

Because there is not enough evidence on human subjects yet, the diabetic electrical remodeling of this study was based on the findings in animal experiments. Nevertheless, this study provides a valuable first step in helping to identify what changes to look for in BSPs among human diabetic subjects.

# Chapter 7

## Geometrical and Electrical Remodeling in Human Subjects

Both diabetes and obesity carry strong risks for cardiovascular disease and sudden cardiac death. Although electrocardiogram (ECG) has been used to predict cardiovascular mortality in diabetes, the prognostic value of ECG abnormalities in diabetics has not been fully characterized. We hypothesize that cardiac abnormalities associated with diabetes can be revealed from body surface potentials (BSPs) and cardiac transmembrane potentials (TMPs). In this chapter, we collected body surface ECGs and heart-torso geometries from two adult males (one normal, one obese diabetic). With these measurements, we estimated the corresponding normal and diabetic cardiac TMPs. An initial characterization of the electrical phenotype of diabetes could be formed by analyzing the BSPs and TMPs.

In Chapter 3 and 4, we implemented the bidomain forward problem formula, and solved the inverse problem. By doing so, we were able to build a connection between BSPs and cardiac TMPs. These two electrical representations can be generated from each other based on a given heart-torso anatomy. In Chapter 5 and 6, the effects of obese anatomical and diabetic electrical remodeling were evaluated separately with simulation experiments. In this chapter, we characterize features of BSPs and TMPs, which are associated with diabetes in the presence of obesity, based on the measurements from real subjects.

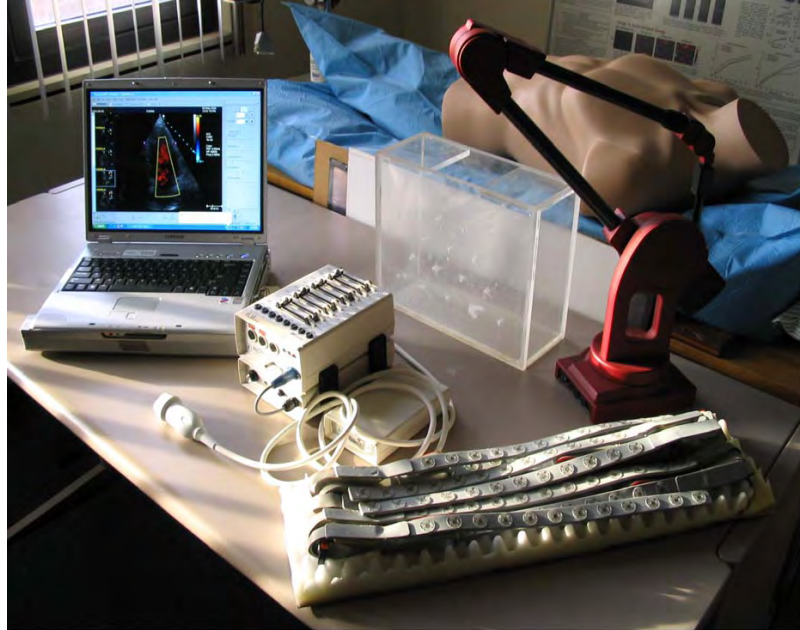


Figure 7.1: Portable Mapping System. Components include a Terason 3000 ultrasonic imaging system, BioSemi ECG mapping system, custom phantom for ultrasonic image registration, and Immersion 3D digitizer.

## 7.1 Clinical Data Acquisition

The clinical data collected from human subjects included their BSPs and heart-torso geometry. During the experiment, we use a Vac-Lok<sup>TM</sup> (Civco Medical Solutions, Kalona, IA ) to immobilize the patients. It contains a cushion filled with polystyrene beads that forms rigidly to the patient when a vacuum is applied. Torso surface geometry was measured with an Immersion 3-D digitizer (Immersion Human Interface Corp., Palo Alto, CA); BSPs were recorded with a BioSemi mapping system (Amsterdam, Netherlands). Heart size, orientation and location were determined with the images taken by a Terason 3000 ultrasonic imaging system (Teratech Corporation, Burlington, MA). Along with a custom image registration phantom, the above equipments comprised a portable mapping system, as shown in Figure 7.1.

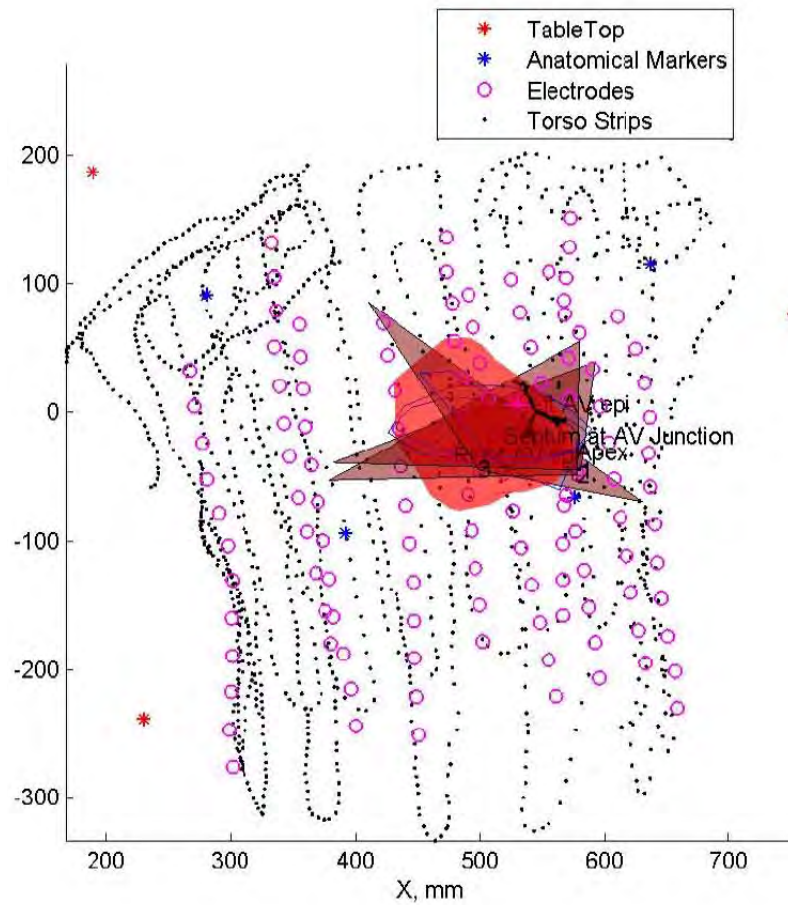


Figure 7.2: Torso surface (black dots) and electrode positions (magenta circles) measured with a 3D digitizer (Immersion 3DL). Red triangles represent the planes on which ultrasound image were taken. The black line on heart surface marks the trace from atrioventricular (AV) node to the apex through AV junction.

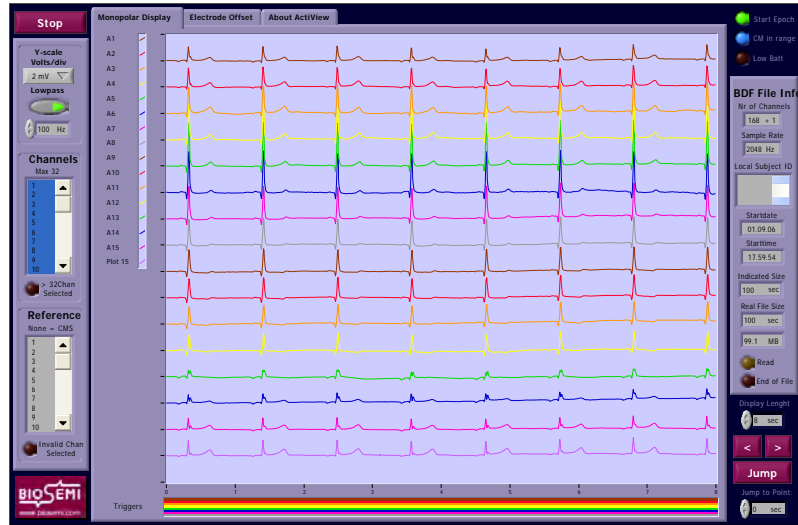


Figure 7.3: Interface of BioSemi ECG Mapping System

### 7.1.1 Protocol

A protocol was developed to control the experimental procedure that consisted of the following steps: 1) Register ultrasonic images of the heart to the coordinate systems of the 3D digitizer [104]. Calibrate the probe by imaging a phantom consisting of multiple N-fiducial and computing a transformation between ultrasound coordinates and Immersion measurements. 2) Measure the torso surface and electrode locations. The anterior surface and electrode was measured by tracing the 3D digitizer directly on subject torso. The posterior surface and electrode locations were recorded on the Vac-Lok, after subject sitting up and getting off it. 3) Record 120-channel body-surface ECG signals with the BioSemi system, which contains the reference electrodes CMS and DRL and ten 12-electrode strips. These electrodes were attached over the front and back of subject torso. 4) Measure the spatial locations of body-surface ECG electrodes with the 3D digitizer. 5) Repeat the above procedures 3 ~ 5 times for data registration consistency. 6) Remove electrodes from the subjects and clean up the equipment. For procedure details, see Appendix D.

### 7.1.2 Heart and Torso Geometry

Figure 7.2 illustrates the geometric measurements for the normal subject. The measured point cloud (black dots) on the torso surface were interpolated into 3D torso models with the Matlab *FastRBF*<sup>TM</sup> Toolbox from FarField Technology Limited (Christchurch, New Zealand). Figure 7.4 demonstrates the resulting normal and obese torsos. A plastic heart model was digitized and used as a template. According to the ultrasound heart images, the template heart was shifted, rotated, scaled, and placed into the torso models [104]. Figure 7.2 also shows the locations of ECG electrodes (magenta circles), which were attached to the front and back of subject torso during experiments. Later in this chapter, these heart-torso geometries are used to solve the inverse problem, and estimate the TMPs for each individual.

### 7.1.3 Electrical Body-Surface Measurements

Body surface ECGs of the subjects were collected with BioSemi ECG system, which contains 123 active electrodes, a receiver, an AD-box, optic cable and a battery box. Figure 7.3 shows the interface of BioSemi. The ECG signals recorded here are raw signals with a sample rate of 2048 Hz. Based on these ECG measurements, we calculated the signal-averaged ECGs (SAECGs). Before the calculation, the raw signals were delimited, de-noised, truncated into ECG cycles. Later in this chapter, heart surface potentials for both subjects are reconstructed from the above SAECGs and geometric models.

## 7.2 Heart and Torso Models

The 3D heart and torso models were built with the Matlab *FastRBF*<sup>TM</sup> Toolbox based on point clouds recorded with the Immersion 3-D digitizer. By comparing the heart-torso models of the two subjects side-by-side in Figure 7.4, we can tell that, in the obese torso, where the abdominal fat is increased, the position and orientation of the heart is changed relative to the torso. These two features have been incorporated

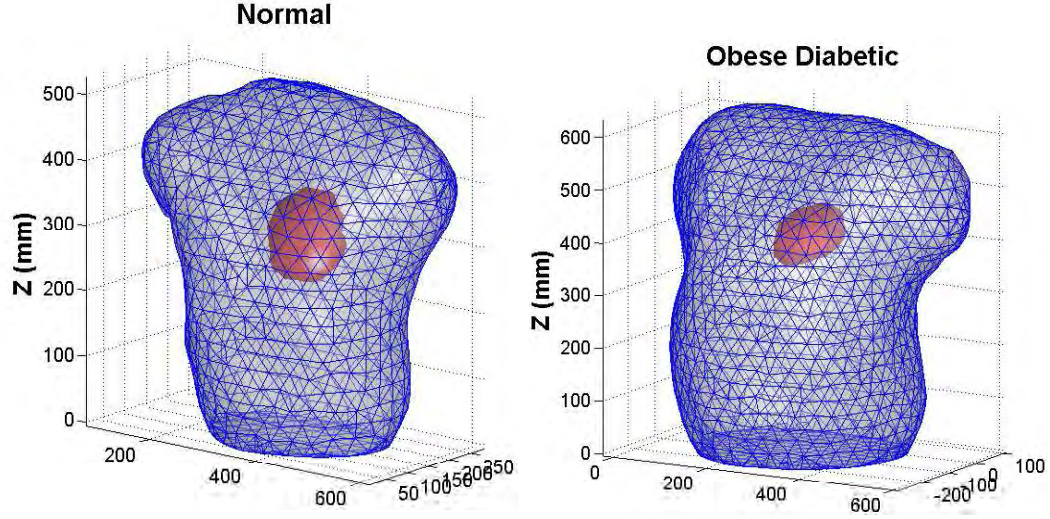


Figure 7.4: The heart-torso geometries. Left) the normal subject. Right) the obese diabetic subject.

in the obese anatomical remodeling in Chapter 5, as extended abdomen (EA) and displaced heart (DH).

In the coming sections, the comparison will first be made between the BSPs directly measured from the two subjects. By doing so, we try to 1) find out which BSPs features, if any, may be useful as potential bio-markers in future diabetic heart studies; and 2) test the conclusions on the sensitivities of BSPs to the obese anatomical and diabetic electrical remodeling, found during the simulations in Chapter 5 and 6. After comparing BSPs, we will reconstruct TMPs for the both subjects, and then compare them to determine if there are TMP changes that may be associated with diabetes.

### 7.3 Body Surface Potentials (BSPs)

A Matlab package was developed to process ECG recordings (100-second, 2048-Hz, 24-bit). With this package, the 120-channel ECGs are low-pass filtered, delimited, cut into cardiac cycles, shifted to base-line, and averaged. One example of the outcoming SAECGs is demonstrated in Figure 7.5, in which the red dash line represents their

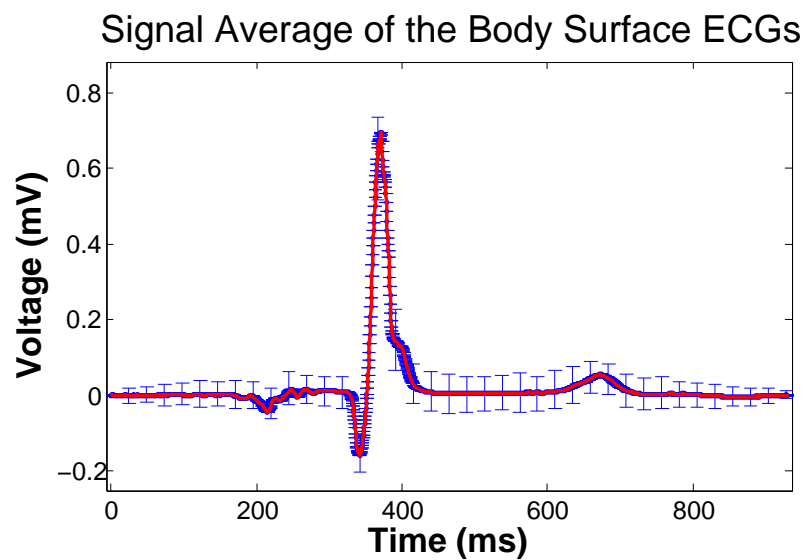


Figure 7.5: ECG signal recorded from the normal subject. After truncating the ECG recording into cycles, certain standard deviations were observed among these cycles (as blue bar). The signal averaged ECG (SAECG) is demonstrated as the red line.

average, while blue bars indicate standard deviation among different cycles recorded with one electrode.

Body surface SAECGs of normal and obese diabetic subjects were compared in Figure 7.6. In the figure, the obese diabetic subject has lower amplitudes of BSPs, especially during R and T wave.

## 7.4 Heart Surface Transmembrane Potentials (TMPs)

The heart surface myocyte TMPs are used to present the cardiac sources, which generate the BSPs. They also play the important role in diabetes associated electrical phenotype. By solving the bidomain inverse problem with an innovative technique, the myocyte TMPs are reconstructed noninvasively from the BSPs measurements of the normal and obese diabetic subjects.

To link BSPs and TMPs together, we developed the *Bidomain Forward Problem Module* in Chapter 3 and the regularized waveform identification (RWI) approach in



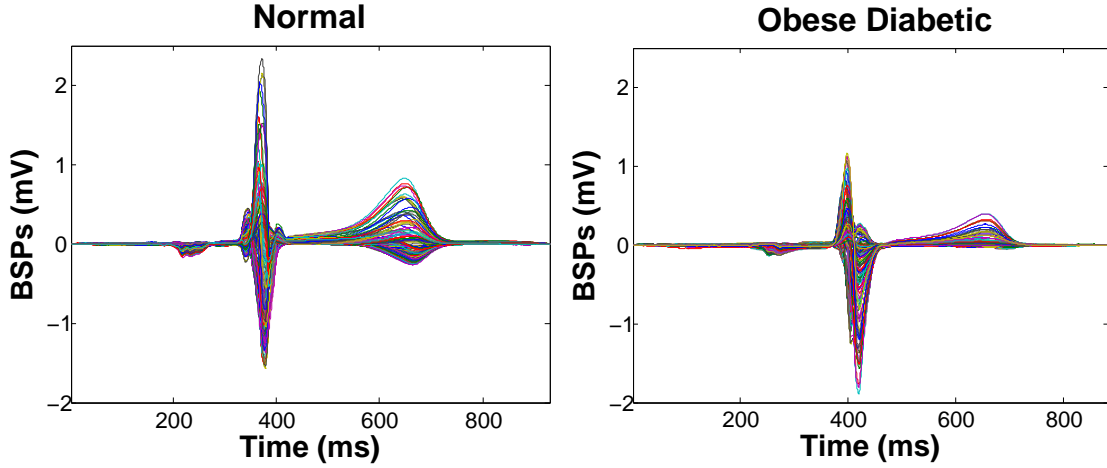


Figure 7.6: BSPs measurements. Left) the normal subject. Right) the obese diabetic subject.

Chapter 4. The forward problem module was used to calculate the transfer matrices for both the normal and diabetic subjects, as  $\mathbf{A}_n$  and  $\mathbf{A}_d$ , based on their torso geometries (in Figure 7.4) and tissue conductivities. During the calculation, the conductivities of the heart and torso equals 0.3 S/m and 0.2 S/m. The outputs of the forward problem module are represented as the following linear equations:

$$\mathbf{V}_n = \mathbf{A}_n \Phi_n \quad , \quad (7.1)$$

$$\mathbf{V}_d = \mathbf{A}_d \Phi_d \quad , \quad (7.2)$$

in which,  $\mathbf{V}_n$  and  $\mathbf{V}_d$  are BSPs for normal and diabetic subjects;  $\Phi_n$  and  $\Phi_d$  are the corresponding TMPs. Here, BSPs during the T wave are fed into the inverse problem to estimate the myocyte TMPs during the repolarization. Figure 7.7 shows the T waves for both individuals, as  $\mathbf{V}_n$  and  $\mathbf{V}_d$ . The signals, measured on the obese diabetic subject, are in a much lower energy level. At the peak of T wave,  $\mathbf{V}_d$  also has less potential divergence in space. This phenomenon does not match the results shown in Figure 6.8, in which diabetic associated APD prolongation increased potential divergence, instead of decreased it.

To estimate TMPs from available BSP measurements, we developed the new approach, called RWI, in which the spatial constraints were accomplished with the

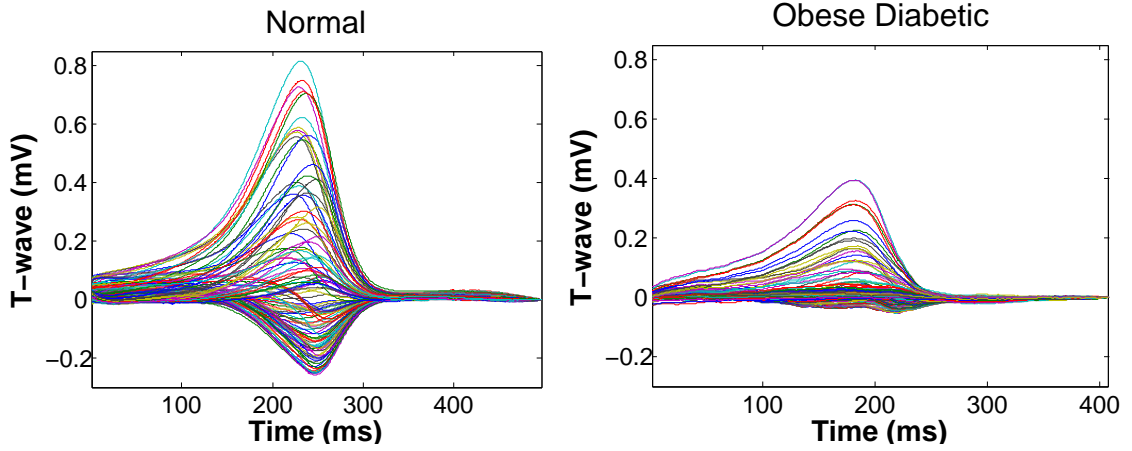


Figure 7.7: BSPs during the T wave. Left) the normal subject. Right) the obese diabetic subject.

regularization approach, such as TSVD or Tikhonov; while the temporal features of TMPs were caught by introducing an averaged waveform.

Specifically, the first step of the inverse approach is to calculate the TMPs with the regularization method. Here, we use truncated singular value decomposition (TSVD). To make the results comparable, the same truncation rank, 20, is set for both regularization cases. The resulting  $\Phi_{\text{TSVD}}$  are shown in Figure 7.9. Similar to the BSPs, the obese diabetic regularization TMPs have, on average, smaller amplitudes and spatial divergence than normal.

As expected, the regularization results do not show the general TMP shape during the repolarization. To solve this problem and to incorporate the temporal information, the averaged waveform identification (AWI) technique is developed. By adding an averaged TMP waveform to the regularization results, the technique recovers the shape information lost during the regularization. Two steps are taken to find the averaged waveform: 1) capture the rough TMPs shape with a parameterized function. Here, we use the logistic function; 2) find the optimal parameter for the selected function. For details, see Chapter 4. Figure 7.9 shows the estimated averaged waveforms for both subjects. We could tell the obese diabetic subject has a much earlier decline on the averaged TMP potential. This result does not match the findings in diabetic animal

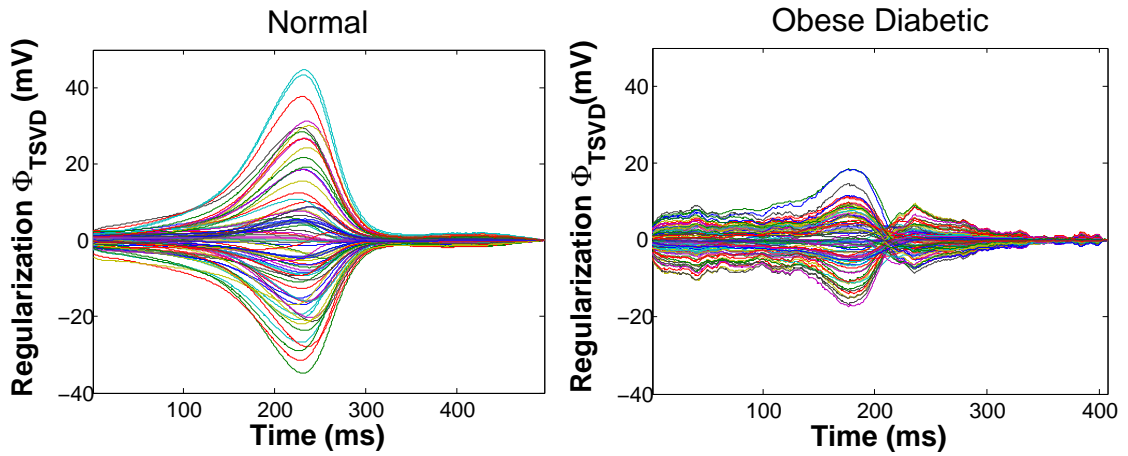


Figure 7.8: Regularization estimation for the repolarization transmembrane potentials. Left) the normal subject. Right) the obese diabetic subject. Regularization rank is 20 for the both cases.

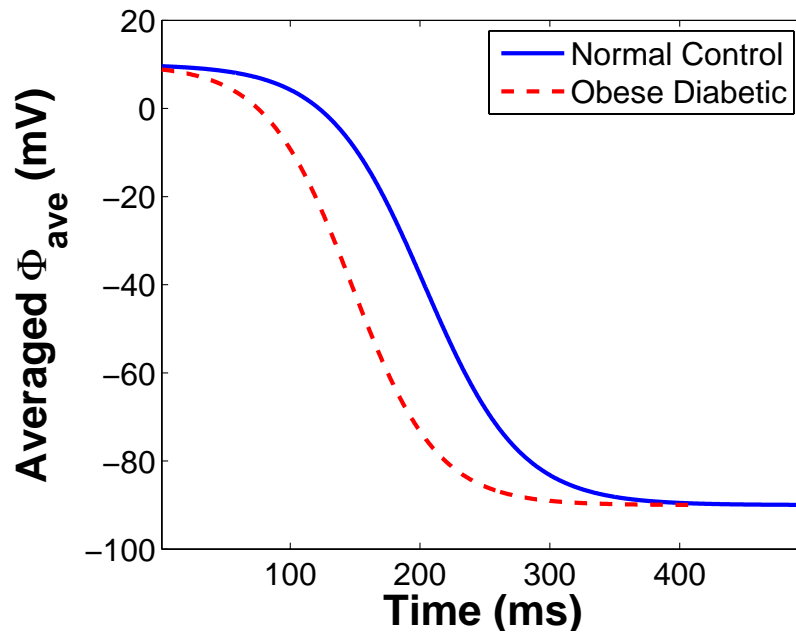


Figure 7.9: The Averaged repolarization transmembrane potentials for the normal subject and obese diabetic subject.

studies, in which APD were found generally prolonged. With the limited number of subjects, we are not able to draw any firm conclusion at this stage.

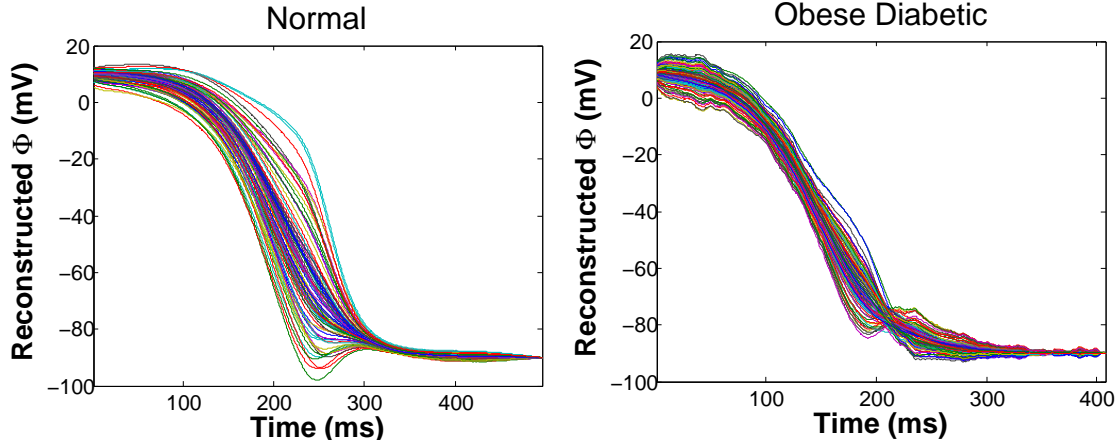


Figure 7.10: Estimated repolarization transmembrane potentials. Left) the normal subject. Right) the obese diabetic subject.

The final TMP estimations are achieved by summing up the regularization results (in Figure 7.8) with the averaged waveform (in Figure 7.9). The results are shown in Figure 7.10. With the same regularization level, the obese diabetic TMPs demonstrate less diversity than the normal one's. In the next section, signal analysis tools will be applied to BSPs and TMPs of the two subjects. Further interpretation will be made based on the analysis results.

## 7.5 Characteristics of BSPs and TMPs

Similar to Chapter 5 and 6, this chapter uses spatial standard deviation (SD), power spectra density (PSD) and principal component analysis (PCA) to extract key features out of BSPs (in Figure 7.6) and repolarization TMPs (in Figure 7.10) of the normal and obese diabetic subjects.

Figure 7.11 shows spatial standard deviation (SD) of the measured BSPs. As we expected from Figure 7.6, the obese diabetic subject has smaller BSP effective values at the peak of R and T wave. Here, the effective value is evaluated with spatial SD. Also, in Figure 7.11, the average cardiac cycle and ST-segment is shorter in the obese

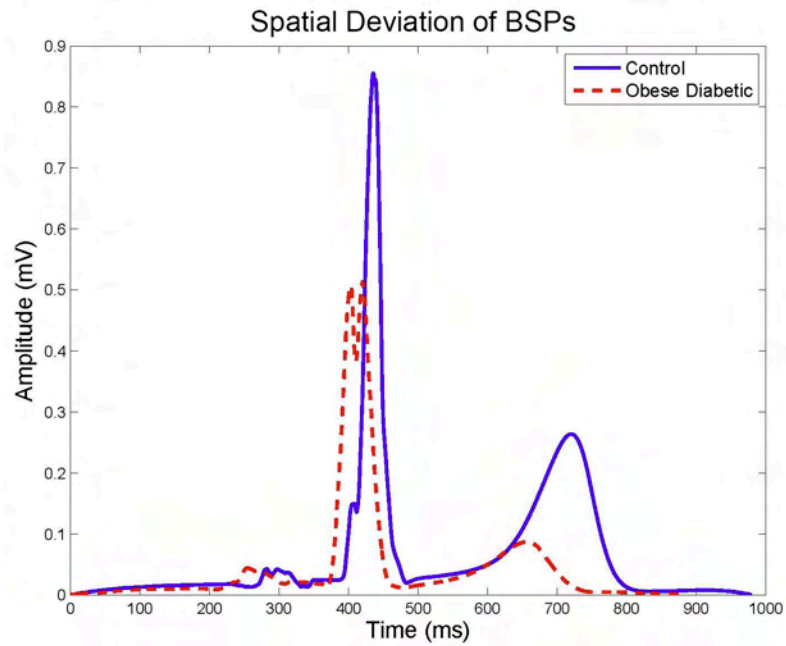


Figure 7.11: Spatial deviation (SD) of BSPs recorded from the normal and obese diabetic subjects.

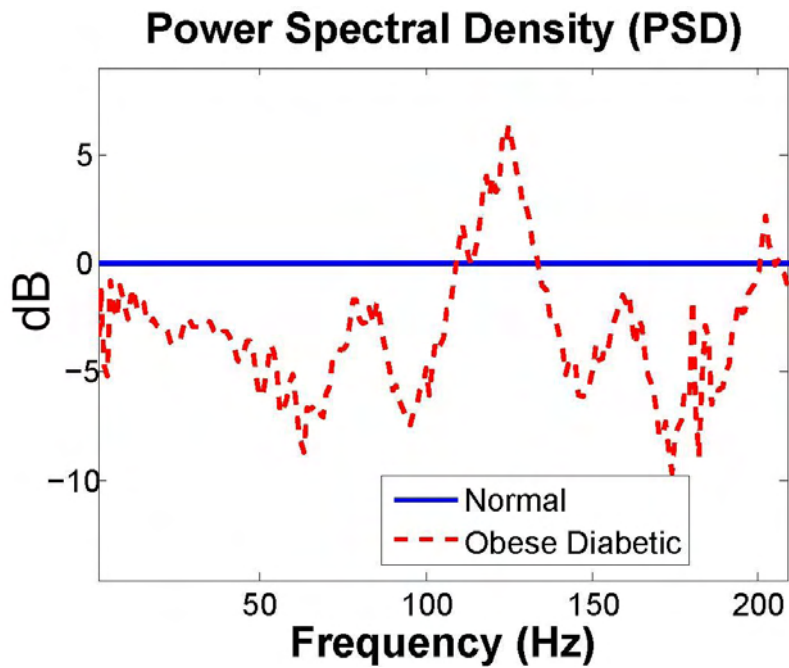


Figure 7.12: Spatial-averaged power spectral density (PSD) of BSPs recorded from the normal and diabetic subjects. Normal PSD is used as zero reference.

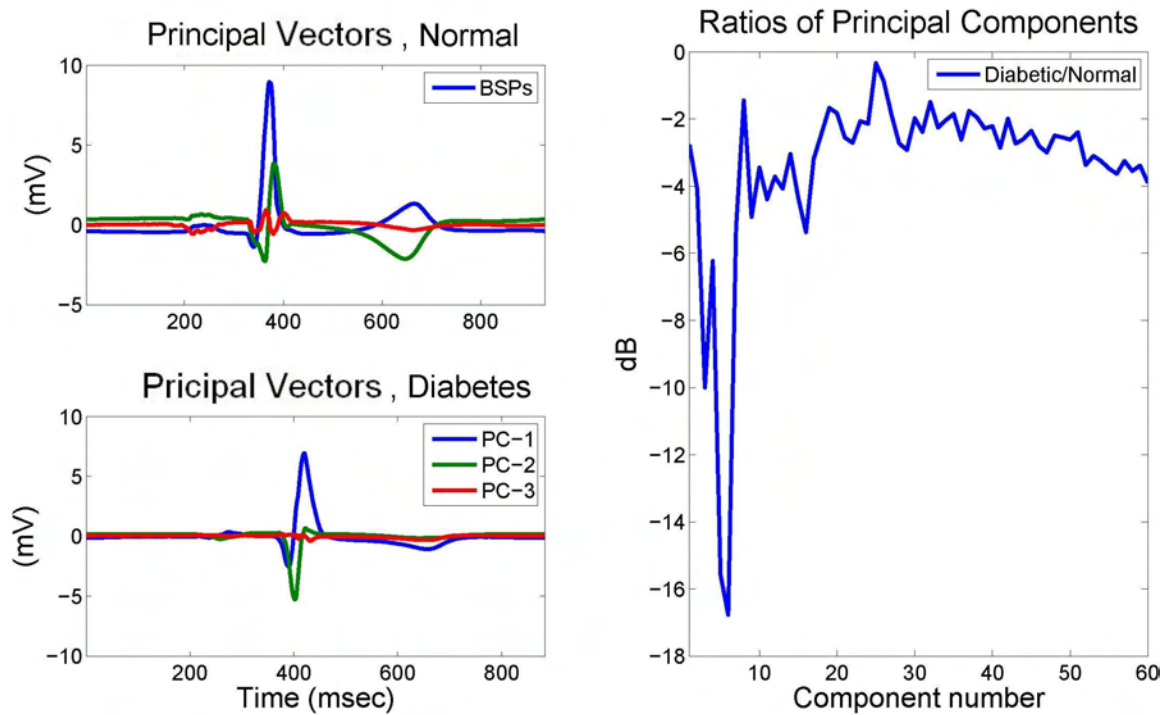


Figure 7.13: Principal component analysis over the cardiac cycle of signal-averaged BSPs from a normal adult male and an obese, diabetic adult male. Left) The first three principal components for the both subjects. Right) The ratio of the principal component coordinates between the obese diabetic subject and the normal. Similar parameters were used by Okin and coworkers. to predicted cardiovascular mortality.[81]

diabetic subject. This phenomenon indicates an earlier repolarization activity on the heart of the diabetic subject. This finding conflicts with the assumption of APD prolongation made in Chapter 6 based on diabetic animal experiments. It suggests the conclusions drawn from diabetic animal studies may not be applicable to diabetic human studies.

Figure 7.12 shows that the obese diabetic BSPs have a lower power spectral density (PSD) than the control's, especially in the diagnostic frequency band  $\leq 100Hz$  specified by the American Heart Association [9]. The result matches what we got in the simulated extended abdomen (EA) obese case in Chapter 5. It indicates the increased fat tissue dilutes the electrical signals on their way traveling to torso surface.

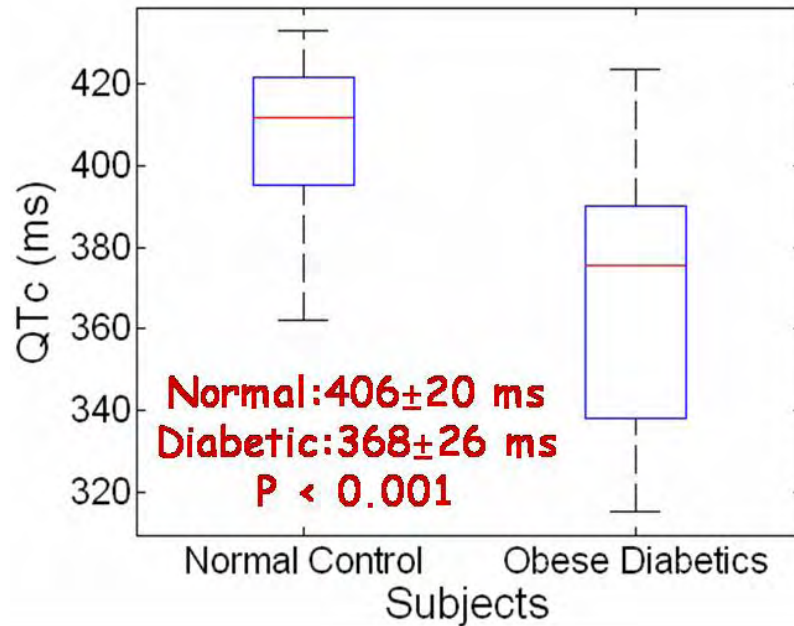


Figure 7.14: The statistical features of QTc intervals for the normal and obese diabetic subject.

The principal components of the obese diabetic BSPs have relatively small amplitudes during T wave compared to those from the normal control, as shown in Figure 7.13. In addition to amplitude changes, for the obese diabetic case, the T wave of the first principal vector is a reverse of the corresponding normal one. The same pattern appeared in Chapter 6, not in Chapter 5. It suggests that the first principal vector could be a potential indicator for diabetic-related cardiac electrical activity changes, and more important, this indicator is not affected by obese habitus.

QT interval is a key ECG feature corresponding to transmembrane potential (TMP) duration, or so-called action potential duration (APD) on the heart. Although, APD prolongation has been found in many diabetic animal experiments [83, 27, 97, 78, 98], there is not enough evidence to show that a similar pattern exists in diabetic human subjects. On the other hand, an abnormal QT interval, especially QT dispersion (QTd), is suggested to be a very useful parameter in the evaluation of cardiovascular risk in participants with Type 2 diabetes, particularly in patients without previous cardiac diseases [38, 85, 19]. It indicates the abnormal QT is related to certain fatal cardiac dysfunction in the presence of diabetes.

In this study, we evaluate the QT correction (QTc) and QTc dispersion for the both subjects. A MATLAB routine was developed to capture the start and end instants of Q wave and T wave respectively. The QTc is calculated from QT with a standard clinical correction, Bazett’s formula, as shown in the following equation,

$$QTc = \frac{QT}{\sqrt{RR}}. \quad (7.3)$$

in which,  $RR$  is the interval between the peaks of two R-waves. It represents the heart rate. Figure 7.14 demonstrates the QTc distributions based on the BSPs of both the normal control and obese diabetic subjects. Unlike what we found in the previous simulation (Figure 6.7), the median QTc value of the obese diabetic subject is shorter than the one of normal subject.

Based on QTc, QTd is calculated as the difference between the maximum and minimum QTc. As a predictor of cardiovascular and cardiac mortality, it is a feature reflecting the underlying heterogeneity of ventricular repolarization. In the previous chapter, QTd of the simulated normal and diabetic BSPs are 41 ms and 83 ms. Here, QTd of the BSPs measured from the normal and obese diabetic subjects are 71 ms and 108 ms. In both simulation and human study, diabetic BSPs demonstrate higher QTd than normal ones do. These results demonstrate significant difference between the two subjects. Further study and a large subject pool is necessary to draw the final conclusion.

In several earlier studies [38, 85, 19], the diabetic patients with a QTd greater than a certain value seemed to have a higher ratio of cardiovascular events and death. The risky value of QTd varies in different studies from 50 to 65 ms. These numbers are not directly comparable to the QTd value in this study, because different from most of the clinical QT studies, we use the BSPs rather than the standard 12-lead ECGs to calculate the QTd.

## 7.6 Conclusions

The goal of this study is to reveal the electrical phenotype of diabetes based on body surface ECG recordings in the presence of obesity. Both the BSP measurements and



the corresponding TMP estimations are characterized and compared between the two available subjects, one normal and one obese diabetic.

Significant differences were found in the BSPs between the two subjects. The BSPs of the obese diabetic subject were shown to have much lower signal effective values during R and T wave. It matches what we found in BSPs of the extended abdomen (EA) case in the obese habitus simulation. An intuitive explanation is that the increased fat tissue weakens the signals observed on body surface. During T wave, the first principal vector of BSPs was reversed in the obese diabetic subject. The same phenomenon was observed in the PCA results of the simulated diabetic ECGs. On the other hand, the three obese habitus did not show such an impact on the first principal vector. These results suggest the first PCA vector could be used as a potential indicator to present certain changes of BSPs due to diabetes electrophysiology, and more important, it is free from obese geometrical effects. Long QT associated with APD prolongation was not observed in the obese diabetic subject. QTd was found increased in both the measured and simulated diabetic BSPs. As a predictor of cardiovascular disfunction, QTd was shown to be associated with the risk of cardiovascular event and even mortality in the presence of diabetes. The discovery here indicates QTd is a valuable feature that may tie up with certain cardiac changes associated with diabetes. Repolarization TMPs were reconstructed from the BSPs measurements of the two subjects with the inverse approach developed in Chapter 4. By comparing their TMPs, we found that the repolarization timing parameters of the obese diabetic TMPs have less spatial variance. Referring to our inverse approach, this phenomenon is associated with the lack of diversity of the amplitudes at the peak of T wave.

This pioneering work will help to reveal electrical biomarkers for diabetes available in a clinical setting. The methods developed here may also be applicable to elucidate electrical features of other cardiac pathology. Differences discovered will represent electrical remodeling in both obesity and diabetes that will serve as a foundation for future studies to identify separate effects of obesity and diabetes. The limitation of the study is the small data set. Measurement from only one subject in each category is obviously inadequate to reach any statistical conclusions. Results and conclusions can be tested by more clinical observations in the future.

# Chapter 8

## Summary, Conclusion and Future Work

Diabetes and obesity are two major risk factors for cardiovascular disease. Obesity is a compounding factor of diabetes. They both have certain electrophysiological and anatomical influences on human body. The goal of this dissertation is to reveal the electrical phenotype of diabetes in the presence of obesity based on the body surface ECGs. Multiple techniques and algorithms were developed to accomplish this goal.

In the study, a bidomain model lays down the foundation for the rest of the work. Based on it, the boundary element method (BEM) was used to solve the forward problem; an approach, named regularized waveform identification (RWI), was innovated to solve the inverse problem. In addition, a collection of MATLAB algorithms was developed to simulate the electrical and anatomical remodeling associated with diabetes and obesity. A set of signal analysis approaches were implemented to process and extract features from the measured or simulated normal, diabetic and obese ECGs. In the rest of this Chapter, we will summarize the contribution and limitations of the above work.

A bidomain simulation platform was constructed to provide a mathematical basis. It contains four modules: 1) *Bidomain Source Module*, 2) *Bidomain Forward-Problem Module*, 3) *Cardio-myocyte transmembrane potential Estimation Module* (also called *Bidomain Inverse-Problem Module*), and 4) *Body-Surface Potential Mapping Module*. The bidomain forward and inverse modules allow us to link transmembrane potentials (TMPs) to body surface potentials (BSPs). TMP represents the electrical activities on a cellular base; while BSPs present comprehensive measurement of heart electrical

activities on body surface. Both TMPs and BSPs are potentially affected by diabetes. By isolating the simulation environment from the practical difficulties associated with actual data, the bidomain platform allows us to investigate the effects of diabetic- and obese-associated remodelings on BSPs as individual factors. The platform provides a feasible means for observing and understanding remodeling and its consequences.

A novel approach, named regularized waveform identification (RWI), was developed to solve the inverse problem based on the bidomain model. In addition to the spatial regularization techniques, our inverse approach brought in the temporal constraints in a simple and straightforward way. The physical model of the double-layer source determines that the unit vector belongs to the null space of the forward transfer matrix. Based on this knowledge, the temporal information of TMP is presented as an averaged TMP waveform. The TMPs are estimated as the summation of the averaged TMP waveform and the regularization results. By incorporating temporal information, in the form of the basic TMP wave shape, estimation accuracy was enhanced while maintaining computational simplicity. We evaluated the sensitivity of our RWI approach to 1, 2, 5 and 10% electrical noise on the body surface. Relative errors (RE) of <15% and correlation coefficients (CC) >0.98 were found. A 10% enlargement of the heart and position errors of  $\pm 1$ cm in all directions yielded REs of <15% and CCs >0.97. Simulation results showed that this approach performed much better than traditional regularization methods alone and is robust in the presence of noise and geometric error.

Obese anatomical remodeling was characterized using three features: left ventricular hypertrophy (LVH), heart displacement and abdomen enlargement. The geometrical variation caused by these obese features were simulated with a set of customized MATLAB routines, which can be applied to future obesity related studies. Based on obese anatomy, body surface ECGs were calculated with the bidomain platform. By comparing the simulated obese and normal ECGs, we evaluated the effects of the three obese features. In the simulation, we found relative errors over the body-surface during the Q-T interval are 12, 30, and 68% for hypertrophy of the heart, extension of the abdomen, and heart displacement with obesity, respectively. The major change to the standard 12-lead set also occurred with heart displacement. The mean relative error over the T wave in the precordial leads V3 to V6 was 83% with heart displacement. The results suggest that geometric changes accompanying obesity have

a significant effect on electrocardiograms that may be confused with electrophysiologic changes due to diabetes. An understanding of the geometric effects is essential to separating changes that occur due to obesity from those due to diabetes. These results also demonstrate the limitations of using the standard 12-lead signals in the presence of hypertrophy, an extended abdomen, and a displaced heart to characterize electrical remodeling with diabetes. On the other hand, body-surface maps can provide a relatively comprehensive view, and help us to have a better understanding on the underlying cause for the changes of potential distribution.

An electrical remodeling associated with diabetes was characterized as regional action potential duration (APD) prolongation. Referring to the discovery made on diabetic rat and the ratio of heart rate between human and rat, diabetic human TMPs were simulated by increasing normal APD with 16, 25 and 29% on three ventricle regions: total right ventricle (RV), subepicardium at the apex of the left ventricle (EpiALV) and subendocardium at the base (EndoBLV) respectively. The corresponding diabetic body surface ECGs were calculated with the bidomain platform. By comparing the simulated diabetic and normal ECGs, we found 125% RE during Q-T interval. Also, both QT interval and QT dispersion (QTd) were found increased due to APD prolongation related to diabetes. In particular, the averaged QT increased from 380 to 419 ms, and QTd increased from 95 to 124 ms. The isopotential maps suggest diabetic associated uneven temporal changes on the heart cause dramatic spatial changes in ECGs on body surface. At the peak of T wave, the maximum potential region of diabetic BSPs were shifted towards the left shoulder. As the result, dramatic distortion was found in 12-lead ECG measurements. Although the insufficient knowledge on diabetic human heart set a limit, the study provides a valuable first step to identify the effects of diabetes on BSPs in human. Based on this work, further study can be carried on.

In the study, we collected BSPs and heart-torso geometric information from two adult males, one normal and one obese diabetic. To collect data, we established a protocol for operating a portable Mapping System, which includes a Terason 3000 ultrasonic imaging system, BioSemi ECG mapping system, custom phantom for ultrasonic image registration, and Immersion 3D digitizer. To process the raw measurements, we also developed a MATLAB signal averaged ECG (SAECG) package. Like the data

collecting system, the package was designed for general ECG related data acquisition. In Chapter 7, the BSP measurements were compared between the two subjects. Referring to the normal, the obese diabetic BSPs show three major changes: 1) the signal effective value was reduced; 2) QT dispersion was increased from 86 to 164 ms 3) during T wave, the first principal vector was flipped. The first phenomenon was also found in the simulated obese case, and it is potentially caused by abdomen enlargement. Unlike the simulated diabetic BSPs, the BSPs measured from the obese diabetic subject did not have increased QT interval. At the same time, QTd was found increased in the both simulated and measured diabetic BSPs. Several studies suggested abnormal QT dispersion (QTd) is an useful predictor of cardiovascular events and mortality in the presence of diabetes. In addition to BSPs, TMPs were reconstructed for the subjects, by using the inverse approach developed in Chapter 4. The results suggest the TMP repolarization of myocyte occurs earlier, and the repolarization timing parameters are less sparse. Obviously, no statistical conclusions can be reached with our limited data set, but the suggestive results call for further clinical observations.

# Appendix A

## ECGSIM Simulation Platform

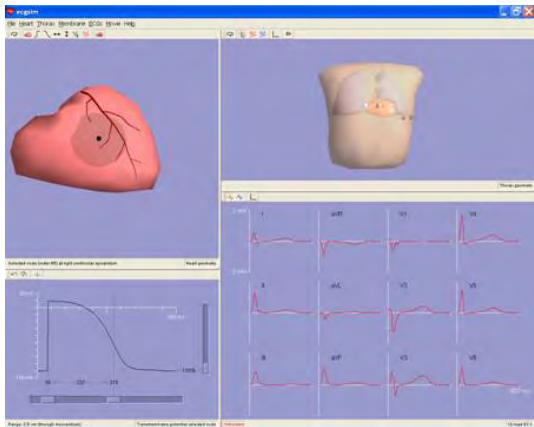


Figure A.1: A snap shot of ECGSIM interface. Upper left) Geometry of and potential distribution on the ventricles. Upper right) Geometry of and potential distribution on the torso. Lower left) Action potential cycle of selected heart-surface location. Lower right) 12-lead ECG signals.

ECGSIM is an interactive simulation program that enables its users to study the relationship between the electric sources of the ventricular myocardium and the resulting potentials on the thorax (QRST waveforms, as well as body surface potential maps) and on the heart surface (electrograms, potential maps, and maps of the local action potential) during both depolarization and repolarization phases of cardiac activity [111]. ECGSIM was designed to serve as a research tool for those interested in testing hypotheses they may have regarding the manifestation of cardiac dysfunction in electrocardiographic waveforms on the thorax. Figure A.1 is a snap shot of ECGSIM interface.

Simulations in this study build on data from ECGSIM (University of Nijmegen, the Netherlands. <http://www.ecgsim.org>). Cardiac AP parameters, body surface potentials, and thorax geometry, including torso and heart models were taken from ECGSIM, as indicated in Figure A.2.

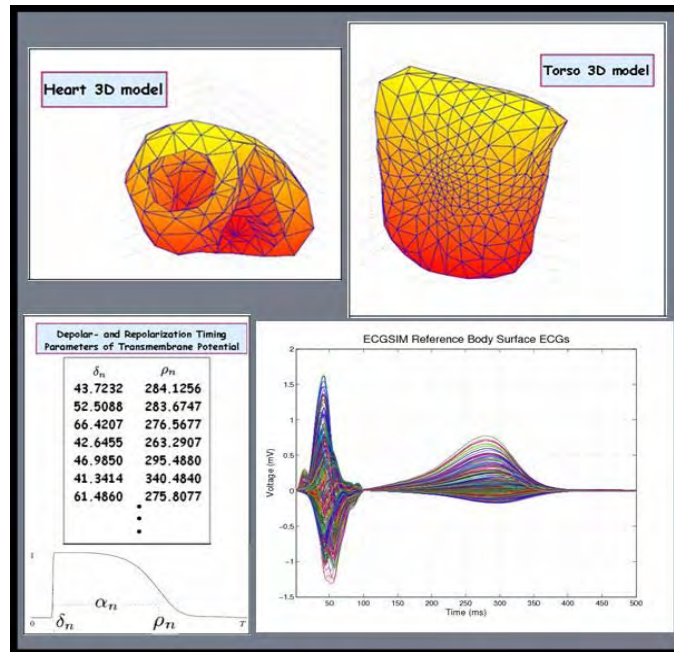


Figure A.2: Data exported from the ECGSIM platform. Upper left) Normal ventricular geometry. Upper right) Normal torso geometry. Lower left) Depolarization and repolarization parameters at 257 nodes on the ventricular surface. Lower right) Body surface potentials during the QRS complex and T wave.

# Appendix B

## Deflation Procedure

To find proper numerical approaches to solve the bidomain forward problem equation (3.23), we need to consider the singularity problem. To solve this problem, the deflation method was employed to remove the undesired eigenvalues of  $\mathbf{B}$ . The resulting matrix  $\mathbf{C}$  shares all the rest of the eigenvalues with  $\mathbf{B}$ . By replacing  $\mathbf{B}$  with  $\mathbf{C}$  in Equation (3.23), we can get the correct solution for the surface potentials.

To simplify the problem let us consider only the torso surface boundary while ignoring the inhomogeneities of the heart and lungs. Based on the definition of solid angle, the summation of each row of matrix  $\mathbf{B}$  will be one, i.e.

$$\mathbf{B}\mathbf{e} = \mathbf{e} \quad , \quad (\text{B.1})$$

where,  $\mathbf{e}$  is the unit column vector. Equation (B.1) indicates  $\mathbf{B}$  has an eigenvalue  $\lambda = 1$ . Correspondingly, one eigenvalue of matrix  $(\mathbf{I} - \mathbf{B})$  will be zero. To avoid this singularity, we need to remove the  $\lambda = 1$  from  $\mathbf{B}$ , by replacing  $\mathbf{B}$  with  $\mathbf{C}$

$$\mathbf{C} = \mathbf{B} - \mathbf{e}\mathbf{p}^t \quad . \quad (\text{B.2})$$

Here,  $\mathbf{p}$  is any column vector, which satisfies

$$\mathbf{e}^t\mathbf{p} = \mathbf{p}^t\mathbf{e} = 1 \quad . \quad (\text{B.3})$$

A common choice for  $\mathbf{p}$  is [64, 65].

$$\mathbf{p} = \mathbf{e}/n \quad , \quad (\text{B.4})$$



where  $n$  is the length of  $\mathbf{e}$ . Matrix  $\mathbf{C}$  has the same eigenvalues as  $\mathbf{B}$ , except for the one at unity, which is replaced by zero [41]. For a homogeneous body, with only one boundary, the torso, we can estimate BSPs  $V_t$  by multiplying the inverse of  $(\mathbf{I} - \mathbf{C})$  with corresponding primary source potentials. If we want to increase the accuracy of estimation by adding more inhomogeneities, such as heart, lungs, or even blood mass, we need to apply multiple deflations to matrix  $\mathbf{B}$ .

During multiple deflation, a set of  $\lambda_s$  need to be removed from  $\mathbf{B}$ . Each  $\lambda_s$  corresponds to one boundary  $S_s$  which separates inhomogeneous tissues.

$$\lambda_s = \frac{\sigma_s^- - \sigma_s^+}{\sigma_s^- + \sigma_s^+}, \quad s = 1, 2, \dots, m \quad , \quad (\text{B.5})$$

where  $\sigma_s^-$  and  $\sigma_s^+$  are conductivities inside and outside boundaries  $S_s$  and  $m$  represents the number of boundaries considered. The corresponding eigenvector  $f_s$  is a column vector with length of  $n_1 + n_2 + \dots + n_m$ , where,  $n_r$  ( $r = 1, 2, \dots, m$ ) is the number of observation locations on surface  $S_r$ .

$$\mathbf{f}_s = [(\mathbf{f}_1^s)^t, (\mathbf{f}_2^s)^t, \dots, (\mathbf{f}_m^s)^t]^t \quad , \quad (\text{B.6})$$

with

$$\mathbf{f}_r^s = \gamma_{rs} \mathbf{e} \quad , \quad (\text{B.7})$$

where

$$\gamma_{rs} = \begin{cases} 0 & \text{for } S_r \text{ not inside and not equals to } S_s \\ 1 & \text{for } S_r \text{ equals to } S_s \\ \frac{(\sigma_s^-)^2 - (\sigma_s^+)^2}{(\sigma_s^-)^2 + (\sigma_s^+)^2} & \text{for } S_r \text{ inside } S_s \end{cases} \quad (\text{B.8})$$

Let  $\mathbf{p}$  share the same size as  $\mathbf{f}_s$  then

$$\mathbf{p} = [0^t, \dots, 0^t, \mathbf{e}_s^t/n_s, 0^t, \dots, 0^t]^t \quad , \quad (\text{B.9})$$

where  $0^t$  are zero vectors with length of  $n_1, n_2, \dots, n_{s-1}, n_{s+1}, \dots, n_m$ . The deflated matrix  $\mathbf{C}$  then becomes

$$\mathbf{C} = \mathbf{B} - \sum_{s=1}^m \lambda_s \mathbf{f}_s \mathbf{p}_s^t \quad . \quad (\text{B.10})$$

# Appendix C

## Torso Extension Routine

A routine used to extend a normal torso into an obese one is introduced in this section. It allows specifying the desired amount of increase in waist circumference (WC). This technique was used in Chapter 5 to simulate the abdominal enlargement that occurs in obese subjects, so that we could evaluate the influence of obese habitus on BSPs.

To generate an obese torso with a given WC, we used two torso models, one normal template torso and one obese reference torso. The former one was a template which was extended to form the obese torso model. The latter one was a real obese torso shape. In the simulation, the normal torso model was exported from ECGSIM [111], as shown in the left of Figure C.1.

As shown on the right of Figure C.1, the reference obese model, with a total of 2840 nodes, provided sufficient detail to guide the extension of the normal torso model. The underlying strategy was to interpolate the space between the given normal template and the obese reference model. Specifically, the procedure can be broken down into the following steps:

1. Adjust the reference obese torso, so that it has the same height as the normal template torso. Specifically, we first shift the centers of both the normal and reference obese torsos to the original point, then divide the X-, Y- and Z-coordinates of the obese reference with the ratio  $r_h$ , where

$$r_h = height_{obese}/height_{normal} \tag{C.1}$$

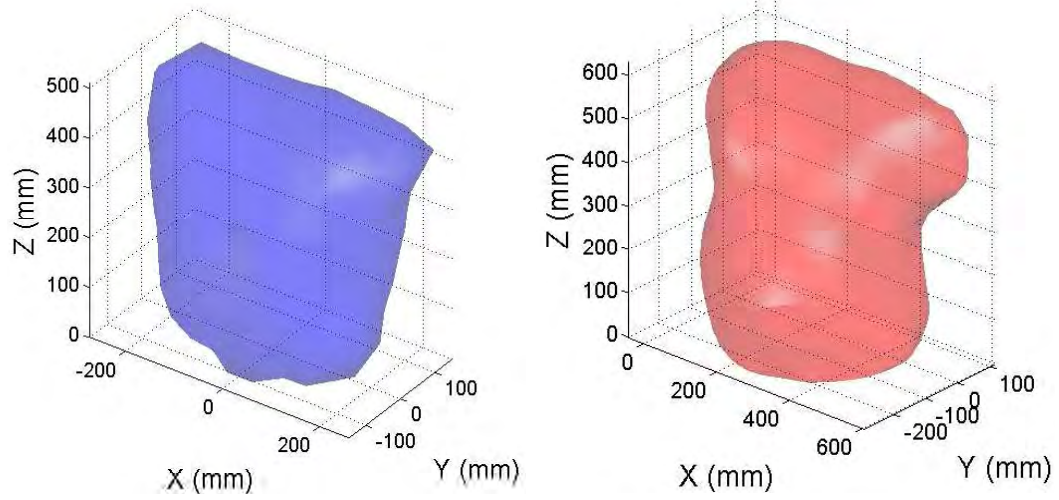


Figure C.1: Left) The ECGSIM torso served as the normal template. Right) Torso model of an obese subject provided detailed information on obese torso shape.

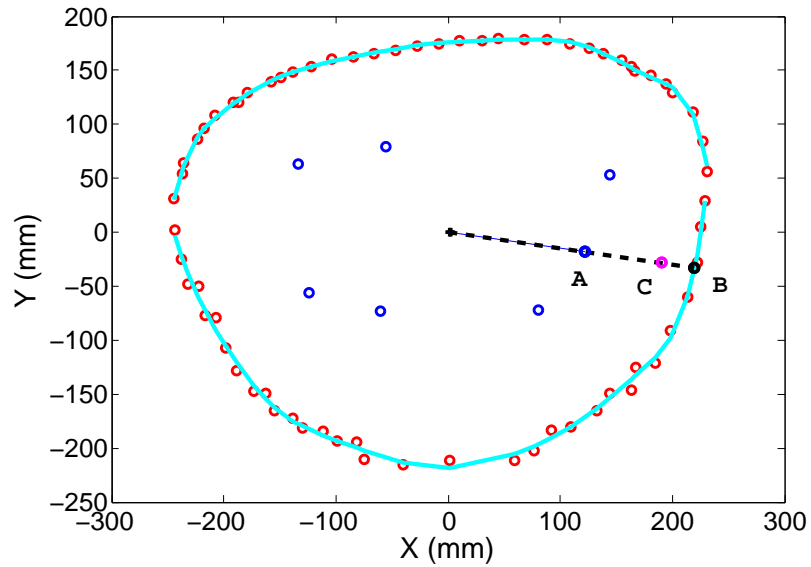


Figure C.2: In one coronal slice, nodes on the boundaries of normal and obese reference torsos are marked as blue and red circles. The red circles were fitted with a polynomial curve (in cyan), which represents a contour of the obese reference torso. For each blue node A, the corresponding node B (in black) was identified on the obese contour. Node C (in magenta) is a node of the output obese torso, corresponding to node A of the normal template. It was determined by interpolating between node A and B.

Given the reference obese torso and the normal template, the ratio  $r_h$  is 1.18 in this study.

2. Lay the normal template and the adjusted obese reference models side by side, then 'cut' them from waist to shoulder, into  $m$  slices, here  $m=20$ .
3. Pick the  $i$ th slice ( $i=1, 2, \dots, m$ ) of the normal and reference obese torsos, and project them onto coronal plane. Now we have two contours composed of nodes from normal and obese torso surfaces, as the blue and red circles shown in Figure C.2
4. For each node on the contour of the normal template, find the corresponding node on the output obese torso with the following sub-steps
  - (a) Curve fit the obese contour with polynomial function, as

$$y = \sum_{j=1}^{n+1} p_j x^{n+1-j} \quad (\text{C.2})$$

here, the polynomial order  $n$  equals to 10.  $x$  and  $y$  are coordinates in coronal plane. The fitted curve is shown in cyan in Figure C.2.

- (b) Draw a ray from origin to node A.
- (c) Find node B, as the cross point of the above ray and the fitted curve of obese boundary.
- (d) Find a point C along the ray crossing both node A and B with a linear interpolation approach. The interpolation ratio  $p$  is preselected based on the amount of waist circumference extension. In Figure C.2, the X- and Y-coordinates for node A and B are  $x_A, y_A, x_B$  and  $y_B$ . Based on them, the coordinates for node C could be found with the following equations.

$$x_C = x_A + (x_B - x_A) \times p \quad (\text{C.3})$$

$$y_C = x_C \times y_A / x_A \quad (\text{C.4})$$

- (e) Repeat sub-steps (b) through (d) until we find all node C's for nodes A's on the normal contour.
5. Repeat Step 3 and 4 for all  $m$  torso slices.

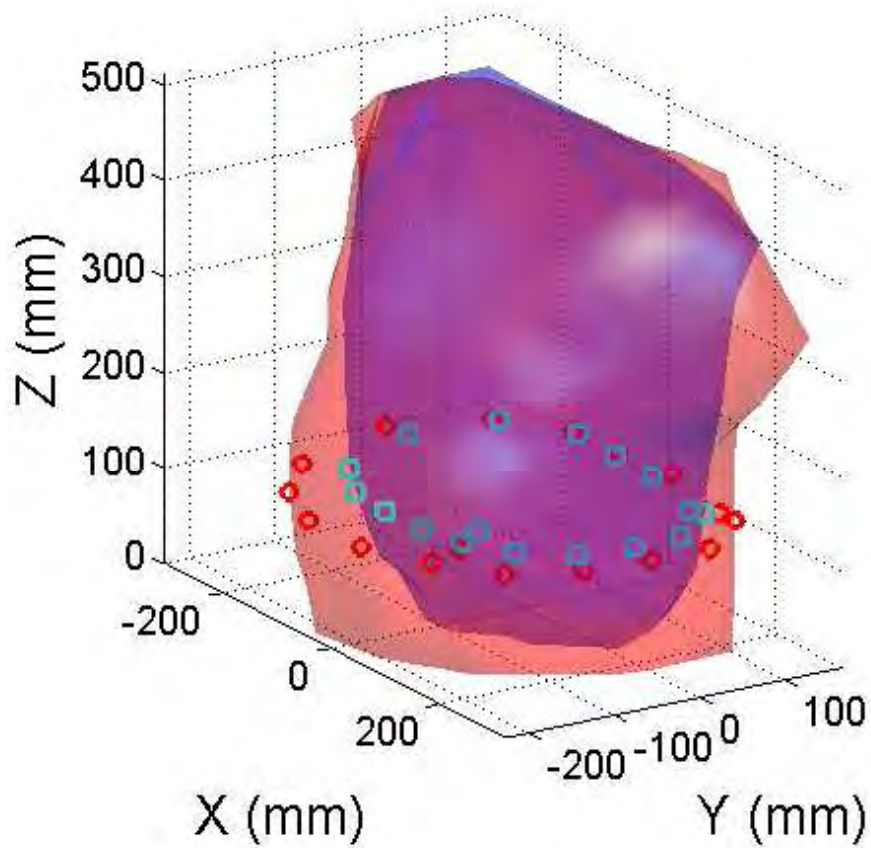


Figure C.3: The normal template (in blue) and the corresponding output obese torso (in red).

Figure C.3 shows the normal reference torso and the interpolated obese torso, with 16% WC increase. These models were used in Chapter 5, to study the influence of abdominal enlargement on ECGs. The routine was designed to generate an obese torso shape by interpolating the space between one normal and one obese torso. The approach developed here can be applied to generate one convex close surface by interpolating two other convex surfaces.

# Appendix D

## Clinical Data Acquisition Protocol

This appendix describes the procedures used to acquire torso and heart geometry as well as electrical body-surface maps for inverse electrocardiography, i.e., to find cardiac-source descriptions from these body-surface measurements.

### D.1 Equipment

The items used in the data collection procedure listed below are shown in Figure 7.1.

- Vac-Lok patient immobilizing system (Civco Medical Solutions, Kalona, IA ) with vacuum pump
- 3D Immersion digitizer (Immersion Human Interface Corp., Palo Alto, CA)
- Biosemi body-surface mapping system (Amsterdam, Netherlands) with 120 electrodes
- Terason 3000 ultrasonic imaging system (Teratech Corporation, Burlington, MA)
- Custom ultrasonic calibration phantom designed by Jason W. Trobaugh and built by Patrick T. Harkins



Figure D.1: Left) Calibration of the ultrasonic view plane with the custom phantom, Right) Ultrasonic scan of the heart with the Terason 3000 system using a 4VC (64-element, 2 MHz) transducer.

## D.2 Preparation

1. Deionize and degas water for the ultrasound calibration phantom (15 minutes)
2. Charge the battery for the Biosemi System (3-4 hours)
3. Prepare the reference electrodes CMS and DRL and the back electrodes D1-D24, E1-E24 by attaching adhesive rings, removing paper covers, and applying electrode paste (13 minutes)
4. Calibrate the ultrasound system as seen in Figure D.1 (16 minutes)
  - Measure the reference-point divots on the phantom with the 3D Immersion digitizer
  - Record images of filaments in the phantom with the focal point near mid-depth of the filaments
  - Mark centers of the filament images
5. Connect the components of the BioSemi system together (1 minute)

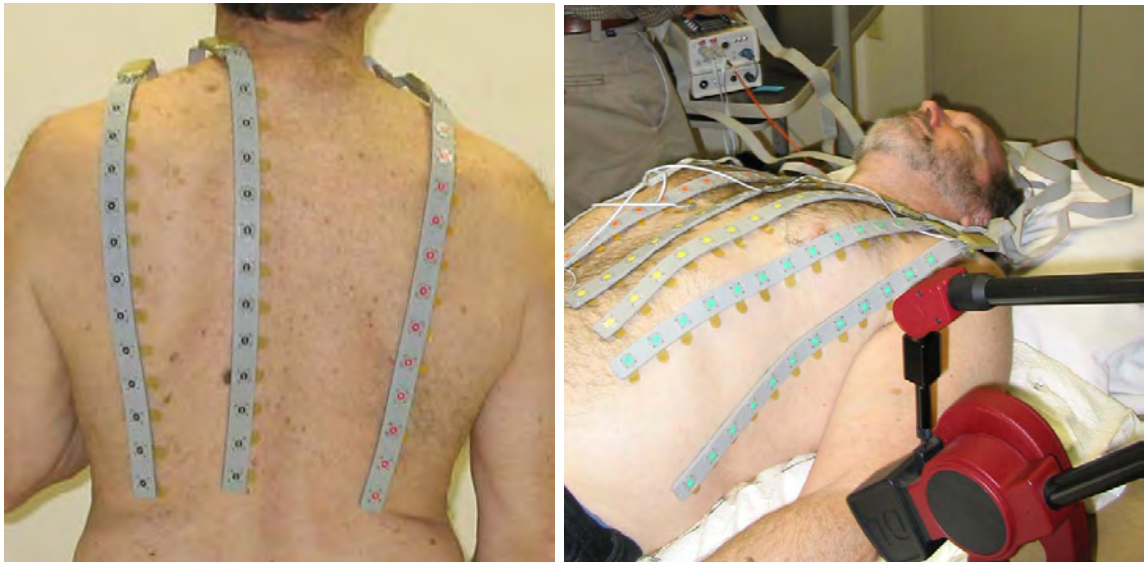


Figure D.2: Left) Position of back electrodes A1-A24 (left two strips) and B1-B12 (right strip). Electrodes B13-B24 are on the right side, Right) Position of front electrodes with C1-24 and on the right side of the anterior midline and D1-24 and E1-E24 on the left side.

### D.3 Data Acquisition

1. Attach reference electrodes (CMS and DRL) and back and right side electrodes (A1-A24 and B1-B24) to the subject, as seen in Figure D.2 (7 minutes)
2. Run the ActiView software, click "start" to request data, check for signal quality and range (2 minutes)
3. Place the subject on the Vac-Lok cushion (10 minutes)
4. Mark 3 table reference points and 4 anatomic reference points, specifically the right arm, left arm, left leg and CMS electrode sites.
5. Check the quality and ranges of the back electrodes signals
6. Acquire apical 4-chamber and parasternal short axis-views of the heart with the Terason 3000 using a 4VC transducer as seen in Figure D.1 (16 minutes)
7. Attach the front electrodes (C1-C24, D1-D24 and E1-E24) to the subject [prepared during the above acquisition steps] as seen in Figure D.2 (18 minutes)



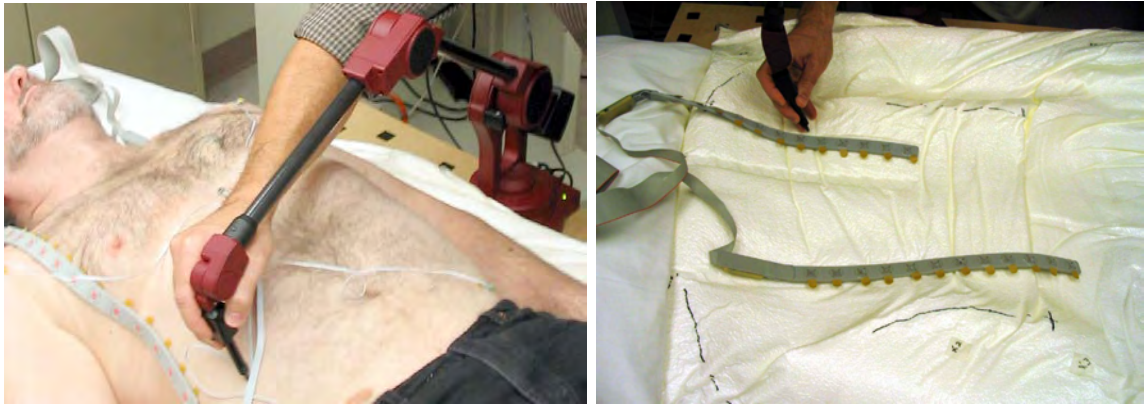


Figure D.3: Torso surface measurement with the Immersion 3DL digitizer. Left) Front torso scan, Right) Back torso scan and measurement of electrode location from Vac-Lok impressions.

8. Check the quality and ranges of the front electrode signals
9. Record body-surface ECGs (5 minutes)
  - Select specific torso channels, reference channels and display scales to view during recording
  - Record ECG signals for 100 seconds, save channels A1-E24, plus EXGs
  - Repeat this procedure to record a second 100-second body-surface map
10. Measure torso surface locations in 3D as shown in Figure D.3 (21 minutes)
  - Record front torso 3D points (8 minutes)
  - Mark tops of strips of D13-D24, E1-E12 and E13-E24 on the Vac-Lok
  - Draw the positions of torso sides on the Vac-Lok
  - Remove front electrodes from the subject (4 minutes)
  - Measure the reference sites on the table and the anatomical sites on the subject
  - Help patient sit up and get off the Vac-Lok
  - Record the location of back torso points and electrodes (9 minutes)
11. Clean up

- Remove back electrodes from the patient during geometrical measurements on the back impressions in the Vac-Lok
- Remove the adhesive rings and electrode paste from the electrodes during geometrical measurement on the back
- Disassemble the Biosemi system and put into its backpack
- Put the Terason 3000, power supply, and the 4VC transducer into its case
- Put the 3DL digitizer into its case
- Store the Vac-Lok and calibration phantom

## D.4 Notes

1. When helping the subject onto or off of the Vac-Lok care must be taken to reduce movement of the Vac-Lok and wrinkling of its surface both of which compromises making accurate geometrical measurements on the back
2. Some electrodes at the end of electrode strips on the front of the torso may need tape to keep them tightly connected to the torso surface
3. We used two electrode paste products; 1) "Signa Gel", which tended to dry out after 15-20 minutes and 2) "Redux Creme", which remained moist throughout ECG body-surface mapping

# Appendix E

## Table of Symbols

$\mathbf{A}$ :	The transfer matrix in the forward and inverse problem.
$A_k$ :	The rank-deficient transfer matrix. It is calculated by removing the small singular values from the original transfer matrix $\mathbf{A}$ .
$\delta$ :	The depolarization timing parameter, indicating the instant when the steepest transmembrane potential incline happens.
$\mathbf{J}$ :	The overall current density.
$\mathbf{J}^i$ :	The impressed current density.
$\Omega_{ji}$ :	The solid angle subtended by source triangle $\Delta_j$ at observation point $i$ .
$\nabla$ :	The gradient operator.
$\vec{p}$ :	A current dipole source.
$\Phi_{ave}, \phi_{ave}$ :	The averaged waveform matrix and vector. The rows of $\Phi_{ave}$ are identical and equal to vector $\phi_{ave}$ , which represents the spatial average of transmembrane potentials on heart.
$\phi_{dep}$ :	The transmembrane potential waveform during the depolarization.
$\Phi_{esti}$ :	The final estimation of transmembrane potentials on heart.
$\Phi_i, \phi_i$ :	The intracellular potential matrix and vector.
$\Phi_m, \phi_m$ :	The transmembrane potential matrix and vector.
$\Phi_o, \phi_o$ :	The extracellular potential matrix and vector.
$\phi_{rep}$ :	The transmembrane potential waveform during the repolarization.

$\Phi_{Laplacian}$ :	The transmembrane potential matrix estimated with the first-order Tikhonov regularization.
$\Phi_{\mathbf{n}}$ and $\Phi_{\mathbf{d}}$ :	The transmembrane potentials on the heart surface for the normal and obese diabetic subjects.
$\Phi_{Tikh}$ :	The transmembrane potential matrix estimated with the Tikhonov regularization.
$\Phi_{TSVD}$ :	The transmembrane potential matrix estimated with the truncated singular value decomposition.
QTd:	The dispersion of QT interval.
QTc:	QT interval correction.
$r$ :	The vector from observation to source boundary element
$\mathbf{R}$ :	The Tikhonov regularization matrix. It is an identity matrix for the zero-order Tikhonov method, and a surface gradient operator for the first-order Tikhonov methods, respectively.
$\rho$ :	The repolarization timing parameter, indicating the instant when the steepest transmembrane potential decline happens.
$\rho_{ave}$ :	The repolarization timing parameter for the averaged waveform.
RR:	The interval between the peaks of two R-waves, representing the pulse rate.
$\sigma_s^-, \sigma_s^+$ :	The conductivities inside and outside a boundary surface.
$S_H$ :	The heart surface.
$T_{dom}$ :	The dominant T-wave waveform.
$U$ and $V$ :	Unitary matrices the results of singular value decomposition. Then contain orthonormal basis vectors.
$\mathbf{V}$ :	The boundary surface potential matrix.
$\mathbf{V}_{\mathbf{n}}$ and $\mathbf{V}_{\mathbf{d}}$ :	The body surface potentials for the normal and obese diabetic subjects.
$V_t, V_h$ and $V_l$ :	The potentials distributed on three closed surfaces surrounding torso, heart, and lung.

# References

- [1] KJ Acton, NR Burrows, LS Geiss, and T Thompson. Diabetes prevalence among american indians and alaska natives and the overall population – united states, 1994-2002. *Morb Mortal Wkly Rep (MMWR)*, Centers for Disease Control and Prevention (CDC), 2003.
- [2] KGMM Alberti, P Aschner, and coworkers. Definition, diagnosis and classification of diabetes mellitus and its complications. Technical report, World Health Organisation Department of Noncommunicable Disease Surveillance, 1999.
- [3] RM Arthur. *Evaluation and use of a human dipole plus quadrupole equivalent cardiac generator*. PhD thesis, University of Pennsylvania, 1968.
- [4] RM Arthur. Signal quality of resting electrocardiograms. *Journal of Electrocardiology*, 16(3):235–244, 1983.
- [5] RM Arthur. Spherical-harmonic approximation to the forward problem of electrocardiology. *Journal of Electrocardiology*, 32:22–33, 1999.
- [6] RM Arthur, DB Geselowitz, SA Briller, and RF Trost. Quadrupole components of the human surface electrocardiogram. *American Heart Journal*, 83:663–677, 1972.
- [7] American Heart Association. Diabetes mellitus: A major risk factor for cardiovascular disease: A joint editorial statement by the american diabetes association; the national heart, lung, and blood institute; the juvenile diabetes foundation international; the national institute of diabetes and digestive and kidney diseases; and the american heart association. *Circulation*, 1999.
- [8] E Avelar, TV Cloward, JM Walker, RJ Farney, M Strong, RC Pendleton, N Segerson, TD Adams, RE Gress, SC Hunt, and SE Litwin. Left ventricular hypertrophy in severe obesity: Interactions among blood pressure, nocturnal hypoxemia, and body mass. *Hypertension*, 49:34–39, 2007.
- [9] JJ Bailey, AS Berson, A Garson, LG Horan, PW Macfarlane, DW Mortara, and C Zywertz. Recommendations for standardization and specifications in automated electrocardiography: bandwidth and digital signal processing. a report for health professionals by an ad hoc writing group of the committee on electrocardiography and cardiac electrophysiology of the council on clinical cardiology, american heart association. *Circulation*, 81:730–739, 1990.

- [10] RC Barr, M Ramsey, and MS Spach. Relating epicardial to body surface potential distributions by means of transfer coefficients based on geometry measurements. *IEEE Trans Biomed Eng*, 24:1–11, 1977.
- [11] DG Beetner. *Inference of spectral and temporal characteristics of pericardial potentials using individualized human heart-torso models and the multipole-equivalent method*. PhD thesis, Washington University in St. Louis, 1997.
- [12] DG Beetner and RM Arthur. Estimation of heart-surface potentials using regularized multipole sources. *IEEE Transactions On Biomedical Engineering*, 51:1366–1373, 2004.
- [13] K Bibbins-Domingo, F Lin, E Vittinghoff, E Barrett-Connor, SB Hulley, D Grady, and MG Shlipak. Predictors of heart failure among women with coronary disease. *Circulation*, 110:1424–1430, 2004.
- [14] NK Bracken, AJ Woodall, FC Howarth, and J Singh. Voltage-dependence of contraction in streptozotocin-induced diabetic myocytes. *Molecular and Cellular Biochemistry*, 261:235–243, 2004.
- [15] DH Brooks, G Ahmad, and RS MacLeod. Multiply constrained inverse electrocardiography: combining temporal, multiple spatial, and iterative regularization. *Proceedings of the 16th Annual International Conference of the IEEE Engineering in Medicine and Biology Society*, 1:137–138, 1994.
- [16] DH Brooks, G Ahmad, RS MacLeod, and GM Maratos. Inverse electrocardiography by simultaneous imposition of multiple constraints. *IEEE Transactions on Biomedical Engineering*, 46:3–18, 1999.
- [17] Dobbelsteyn C. A comparative evaluation of waist circumference, waist-to-hip ratio and body mass index as indicators of cardiovascular risk factors. the canadian heart health surveys. *Int J Obes Relat Metab Disord*, 25:652–661, 2001.
- [18] ME Cain, HD Ambos, J Markham, BD Lindsay, and RM Arthur. Diagnostic implications of spectral and temporal analysis of the entire cardiac cycle in patients with ventricular tachycardia. *Circulation*, 83(5):1637–1648, 1991.
- [19] CRL Cardoso, GF Salles, and W Deccache. Prognostic value of QT interval parameters in type 2 diabetes mellitus results of a long-term follow-up prospective study. *Journal of Diabetes and Its Complications*, 17:169–178, 2003.
- [20] VJ Carey, EE Walters, GA Colditz, CG Solomon, WC Willett, BA Rosner, FE Speizer, and JE Manson. Body fat distribution and risk of non-insulin-dependent diabetes mellitus in women. the nurses’ health study. *Am J Epidemiol*, 145:614–619, 1997.

- [21] O Casis, M Gallego, M Iriarte, and JA Sanchez-Chapula. Effects of diabetic cardiomyopathy on regional electrophysiologic characteristics of rat ventricle. *Diabetologia*, 43:101–109, 2000.
- [22] HC Chiu, A Kovacs, RM Blanton, X Han, M Courtois, CJ Weinheimer, KA Yamada, S Brunet, H Xu, JM Nerbonne, MJ Welch, NM Fettig, TL Sharp, N Sambandam, KM Olson, DS Ory, and JE Schaffer. Transgenic expression of fatty acid transport protein 1 in the heart causes lipotoxic cardiomyopathy. *Circulation Research*, 96:225–33, 2005.
- [23] PK Christensen. QTc interval length and QT dispersion as predictors of mortality in patients with non-insulin-dependent diabetes. *Scandinavian Journal of Clinical and Laboratory Investigation*, 60:323–332, 2000.
- [24] PK Christensen, MA Gall, A Major-Pedersen, A Sato, P Rossing, L Breum, A Pietersen, J Kastrup, and HH Parving. QTc interval length and QT dispersion as predictors of mortality in patients with non-insulin-dependent diabetes. *Scand J Clin Lab Invest*, 60:323–332, 2000.
- [25] RB Devereux, MJ Roman, M Paranicas, MJ O’Grady, ET Lee, TK Welty, RR Fabsitz, D Robbins, ER Rhoades, and BV Howard. Impact of diabetes on cardiac structure and function : The strong heart study. *Circulation*, 101:2271–2276, 2000.
- [26] D di Bernardo, P Langley, and A Murray. Effect of changes in heart rate and in action potential duration on the electrocardiogram T wave shape. *Physiological Measurement*, 23:355–364, 2002.
- [27] MP ESauviat and D Feuvray. Electrophysiological analysis of the sensitivity to calcium in ventricular muscle from alloxan diabetic rats. *Basic Res Cardiol*, 81:489–96, 1986.
- [28] G Fischer, B Tilg, R Modre, GJM Huiskam, J Fetzer, W Rucker, and P Wach. A bidomain model based bem-fem coupling formulation for anisotropic cardiac tissue. *Annals of Biomedical Engineering*, 28(10):1229–1243, 2000.
- [29] Wilson FN, Macleod G, Barker PS, Johnston FD, and Mich AA. The determination and the significance of the areas of the ventricular deflections of the electrocardiogram. *Am Heart J*, 10:46–61, 1934.
- [30] M Foppa, BB Duncan, DK Arnett, EJ Benjamin, PR Liebson, TA Manolio, and TN Skelton. Diabetes, gender, and left ventricular structure in african-americans: the atherosclerosis risk in communities study. *Cardiovasc Ultrasound*, 4:43, 2006.

- [31] CS Fox, MJ Pencina, JB Meigs, RS Vasan, YS Levitzky, and RB D'Agostino. Trends in the incidence of Type 2 diabetes mellitus from the 1970s to the 1990s: The framingham heart study. *Circulation*, 113:2914–2918, 2006.
- [32] E Fox, H Taylor, M Andrew, H Han, E Mohamed, R Garrison, and T Skelton. Body mass index and blood pressure influences on left ventricular mass and geometry in african americans the atherosclerotic risk in communities (aric) study. *Hypertension*, 44:55–60, 2004.
- [33] DB Geselowitz. Multipole representation for an equivalent cardiac generator. *Proc IRE*, pages 48–75, 1960.
- [34] DB Geselowitz. A bidomain model for anisotropic cardiac muscle. *Annals of Biomedical Engineering*, 11:191–206, 1983.
- [35] DB Geselowitz. Use of time integrals of the ecg to solve the inverse problem. *IEEE Trans on Biomed Engr*, 32(1):73–75, 1985.
- [36] DB Geselowitz. On the theory of the electrocardiogram. *processings of the IEEE*, 77(6):857–876, 1989.
- [37] DB Geselowitz and OH Schmitt. *Biomedical Engineering*, chapter Electrocardiography, pages 333–390. McGraw-Hill, New York, NY, 1969.
- [38] W Deccache GF Salles and CRL Cardoso. Usefulness of QT-interval parameters for cardiovascular risk stratification in Type 2 diabetic patients with arterial hypertension. *Journal of Human Hypertension*, 19:241–249, 2005.
- [39] SM Grundy, A Garber, R Goldberg, S Havas, R Holman, C Lamendola, WJ Howard, P Savage, J Sowers, and GL Vega. Prevention conference vi: Diabetes and cardiovascular disease: Writing group iv: Lifestyle and medical management of risk factors. *Circulation*, 105:165–169, 2002.
- [40] RM Gulrajani. The forward and inverse problems of electrocardiography. *IEEE Engineering in Medicine and Biology*, 17:84–101, 1998.
- [41] RM Gulrajani, FA Roberge, and GE Mailloux. Comprehensive electrocardiology. theory and practice in health and disease., 1989. Chapter 8, The forward problem of electrocardiography.
- [42] F Hadaegh, A Zabetian, H Harati, and F Azizi. Waist/height ratio as a better predictor of Type 2 diabetes compared to body mass index in tehranian adult men - A 3.6-year prospective study. *American Journal of Clinical Nutrition*, 81:555–563, 2005.



- [43] TS Han, EM van Leer, JC Seidell, and MEJ Lean. Waist circumference action levels in the identification of cardiovascular risk factors: prevalence study in a random sample. *Br Med J*, 311:1401–1405, 1995.
- [44] Per Christian Hansen, editor. *Rank-deficient and Discrete Ill-posed Problems*. SIAM, 1997.
- [45] BV Howard, ET Lee, LD Cowan, RB Devereux, JM Galloway, OT Go, WJ Howard, ER Rhoades, DC Robbins, ML Sievers, and TK Welty. Rising tide of cardiovascular disease in american indians the strong heart study. *Circulation*, 99:2389–2395, 1999.
- [46] FC Howarth, M Jacobson, O Naseer, and E Adeghate. Short-term effects of streptozotocin-induced diabetes on the electrocardiogram, physical activity and body temperature in rats. *Experimental Physiology*, 90:237–245, 2005.
- [47] G Huiskamp and A van Oosterom. The depolarization sequence of the human heart surface computed from measured body surface potentials. *IEEE Trans on Biomed Engr*, 35(12):1047–1058, 1988.
- [48] V Iyer, R Mazhari, and RL Winslow. A computational model of the human left-ventricular epicardial myocyte. *Biophysical Journal*, 87:1507–1525, 2004.
- [49] PR Johnston and RM Gulrajani. A new method for regularization parameter determination in the inverse problem of electrocardiography. *IEEE Transactions on Biomedical Engineering*, 44:19–39, 1997.
- [50] X Jouven, RN Lemaitre, TD Rea, N Sotoodehnia, JP Empana, and DS Siscovick. Diabetes, glucose level, and risk of sudden cardiac death. *European Heart Journal*, 26:2142–2147, 2005.
- [51] K Karason, I Wallentin, B Larsson, and L Sjostrom. Effects of obesity and weight loss on left ventricular mass and relative wall thickness: survey and intervention study. *BMJ*, 315:912–916, 1997.
- [52] MT Keating and MC Sanguinetti. Molecular and cellular mechanisms review of cardiac arrhythmias. *Cell*, 104:569–580, 2001.
- [53] W Kruskal. When are gauss-markov and least squares estimators identical? a coordinate-free approach. *The Annals of Mathematical Statistics*, 39:70–75, 1968.
- [54] AP Lalani, B Kanna, J John, KJ Ferrick, MS Huber, and LE Shapiro. Abnormal signal-averaged electrocardiogram (saecg) in obesity. *Obesity Research*, 8:20–28, 2000.

- [55] L Lapidus, C Bengtsson, B Larsson, K Pennert, E Rybo, and L Sjoström. Distribution of adipose tissue and risk of cardiovascular disease and death: a 12-y follow-up of participants in the population study of women in gothenburg, sweden. *Br Med J*, 289:1257–1260, 1984.
- [56] B Larsson, K Svardsudd, L Welin, L Wilhelmsen, P Bjorntorp, and G Tibblin. Abdominal adipose tissue distribution, obesity and risk of cardiovascular disease and death: 13-y follow-up of participants in the study of the men born in 1913. *Br Med J*, 288:1401–1404, 1984.
- [57] T Lindström, L Jorfeldt, L Tegler, and HJ Arnqvist. Hypoglycaemia and cardiac arrhythmias in patients with Type 2 diabetes mellitus. *Diabet-Med*, 9(6):536–41, 1992.
- [58] QZ Liu, WC Knowler, RG Nelson, MF Saad, MA Charles, IM Liebow, PH Bennett, and DJ Pettitt. Insulin treatment, endogenous insulin concentration, and ecg abnormalities in diabetic pima indians: cross-sectional and prospective analyses. *Diabetes*, 41(9):1141–1150, 1992.
- [59] PA Lotufo, JM Gaziano, CU Chae, UA Ajani, G Moreno-John, JE Buring, and JE Manson. Diabetes and all-cause and coronary heart disease mortality among us male physicians. *Archives of Internal Medicine*, 161:242–7, 2001.
- [60] National Heart Lung and Blood Institute. Guidelines on overweight and obesity: Electronic textbook - according to waist circumference. [http : //www.nhlbi.nih.gov/guidelines/obesity/e\\_txbk/txgd/4142.htm](http://www.nhlbi.nih.gov/guidelines/obesity/e_txbk/txgd/4142.htm).
- [61] CH Luo and Y Rudy. A dynamic model of the cardiac ventricular action potential. i. simulations of ionic currents and concentration changes. *Circulation Research*, 74:1071–1096, 1994.
- [62] RL Lux. Electrocardiographic mapping. noninvasive electrophysiological cardiac imaging. *Circulation*, 87:1040–1042, 1993.
- [63] RL Lux. Electrocardiographic potential correlations: Rationale and basis for lead selection and ecg estimation rationale. *Journal of Electrocardiology*, 35 Supplement, 2002.
- [64] MS Lynn and WP Timlake. The numerical solution of singular integral equations of potential theory. *Numerische Mathematik*, 11:77–98, 1968.
- [65] MS Lynn and WP Timlake. The use of multiple deflations in the numerical solution of singular systems of equations, with applications to potential theory. *SIAM J of Numerical Analysis*, 5(2):303–322, 1968.
- [66] RS MacLeod and DH Brooks. Recent progress in inverse problems in electrocardiology. *IEEE EMBS Magazine*, 17:73–83, 1998.

- [67] SW MacMahon, DE Wilcken, and GJ Macdonald. The effect of weight reduction on left ventricular mass. a randomized controlled trial in young, overweight hypertensive patients. *N Engl J Med*, 314:334–339, 1986.
- [68] J Malmivuo and R Plonsey. *Bioelectromagnetism: Principles and Applications of Bioelectric and Biomagnetic Fields*. Oxford University Press, USA, 1 edition, 1995.
- [69] BJ Messinger-Rapport and Y Rudy. Regularization of the inverse problem in electrocardiography: A model study. *Mathematical Bioscience*, 89:79–118, 1988.
- [70] B Messnarz, B Tilg, R Modre, G Fischer, and F Hanser. A new spatiotemporal regularization approach for reconstruction of cardiac transmembrane potential patterns. *IEEE Transactions On Biomedical Engineering*, 51:273–281, 2004.
- [71] WT Miller III and DB Geselowitz. Simulation studies of the electrocardiogram. i. the normal heart. *Circulation Research*, 43:301–315, 1978.
- [72] DM Mirvis. *Body Surface Electrocardiographic Mapping*, chapter 4. Methods for body surface electrocardiographic mapping, pages 43–62. Kluwer Academic Publishers, 1988.
- [73] DM Mirvis. *Body Surface Electrocardiographic Mapping*, chapter 5. Validation of Body Surface Electrocardiographic Mapping, pages 63–74. Kluwer Academic Publishers, 1988.
- [74] G Molon, G Targher, A Costa, L Bertolini, E Barbieri, and L Zenari. Measurement of microvolt T-wave alternans, a new arrhythmic risk stratification test, in Type 2 diabetic patients without clinical cardiovascular disease. *Diabetic Medicine*, 23:207–210, 2006.
- [75] AAO Naas, NC Davidson, C Thompson, F Cummings, SA Ogston, RT Tung, RW Newton, and AD Struthers. QT and QTc dispersion are accurate predictors of cardiac death in newly diagnosed non-insulin dependent diabetes: cohort study. *BMJ*, 316:745–746, 1998.
- [76] S Natarajan, Y Liao, G Cao, SR Lipsitz, and DL McGee. Sex differences in risk for coronary heart disease mortality associated with diabetes and established coronary heart disease. *Archives Internal Medicine*, 163:1735–1740, 2003.
- [77] A Nishiyama, DN Ishii, PH Backx, BE Pulford, BR Birks, and MM Tamkun. Altered K<sup>+</sup> channel gene expression in diabetic rat ventricle: isoform switching between Kv4.2 and Kv1.4. *Am J Physiol Heart Circ Physiol*, 281:1800–1807, 2001.

- [78] S Nobe, M Aomine, M Arita, S Ito, and R Takaki. Chronic diabetes mellitus prolongs action potential duration of rat ventricular muscles: circumstantial evidence for impaired Ca<sup>2+</sup> channel. *Cardiovascular research*, 24:381–389, 1990.
- [79] PM Okin, RB Devereux, E Gerdtts, SM Snapinn, KE Harris, S Jern, SE Kjeldsen, S Julius, JM Edelman, LH Lindholm, and B Dahlof. Impact of diabetes mellitus on regression of electrocardiographic left ventricular hypertrophy and the prediction of outcome during antihypertensive therapy. the losartan intervention for endpoint (life) reduction in hypertension study. *Circulation*, 113:1588–1596, 2006.
- [80] PM Okin, RB Devereux, BV Howard, RR Fabsitz, ET Lee, and TK Welty. Assessment of qt interval and qt dispersion for prediction of all-cause and cardiovascular mortality in american indians : The strong heart study. *Circulation*, 101:61–66, 2000.
- [81] PM Okin, RB Devereux, ET Lee, JM Galloway, and BV Howard. Electrocardiographic repolarization complexity and abnormality predict all-cause and cardiovascular mortality in diabetes the strong heart study. *DIABETES*, 53:434–440, 2004.
- [82] HS Oster and Y Rudy. The use of temporal information in the regularization of the inverse problem of electrocardiography. *IEEE Transactions on Biomedical Engineering*, 39:65–75, 1992.
- [83] P Pacher, Z Ungvari, PP Nanasi, and V Kecskemeti. Electrophysiological changes in rat ventricular and atrial myocardium at different stages of experimental diabetes. *Acta Physiologica*, 166:7–13, 1999.
- [84] LR Peterson, AD Waggoner, KB Schechtman, T Meyer, RJ Gropler, B Barzilai, and VG Davaila-Roman. Alterations in left ventricular structure and function in young healthy obese women assessment by echocardiography and tissue doppler imaging. *Journal of the American College of Cardiology*, 43:1399–1404, 2004.
- [85] M Psallasa, N Tentolourisa, D Papadogiannisa, D Doulgerakisa, A Kokkinosa, DV Cokkinosb, and N Katsilambros. QT dispersion comparison between participants with Type 1 and 2 diabetes and association with microalbuminuria in diabetes. *Journal of Diabetes and Its Complications*, 20:88–97, 2006.
- [86] M Ramsey, RC Barr, and MS Spach. Comparison of measured torso potentials with those simulated from epicardial potentials for ventricular depolarization and repolarization in the intact dog. *Circ Res*, 41:660–672, 1977.
- [87] W Rosamond, K Flegal, G Friday, K Furie, and coworkers. Heart disease and stroke statistics – 2007 update. Technical report, American Heart Association and American Stroke Association, 2007.

- [88] P Rossing, L Breum, A Major-Pedersen, A Sato, H Winding, A Pietersen, J Kastrup, and HH Parving. Prolonged qtc interval predicts mortality in patients with Type 1 diabetes mellitus. *Diabetic Medicine*, 18:199–205, 2001.
- [89] Y Rudy. The eccentric spheres model as the basis for a study of the role of geometry and inhomogeneities in electrocardiography. *IEEE Transactions on Biomedical Engineering*, 26:392–399, 1979.
- [90] Y Rudy and HS Oster. The electrocardiographic inverse problem. *Critical Reviews in Biomedical Engineering*, 20:25–46, 1992.
- [91] Y Rudy, R Plonsey, and J Liebman. The effects of variations in conductivity and geometrical parameters on the electrocardiogram, using an eccentric spheres model. *Circ. Res.*, 44:104–111, 1979.
- [92] Y Rudy and JR Silva. Computational biology in the study of cardiac ion channels and cell electrophysiology. *Quarterly Reviews of Biophysics*, pages 1–60, 2006.
- [93] PT Sawicki, S Kiwitt, R Bender, and M Berger. The value of QT interval dispersion for identification of total mortality risk in non-insulin dependent diabetes mellitus. *Journal of Internal Medicine*, 243:49–56, 1998.
- [94] E Seyfeli, M Duru, G Kuvandik, H Kaya, and F Yalcin. Effect of obesity on P-wave dispersion and QT dispersion in women. *International Journal of Obesity*, 30:957–961, 2006.
- [95] V Shahidi, P Savard, and R Nadeau. Forward and inverse problem of electrocardiography: Modeling and recovery of epicardial potentials in humans. *IEEE Trans Biomed Engr*, 41:249–256, 1994.
- [96] M Shields and M Tjepkema. Trends in adult obesity. *Health Reports*, 17(3):53–59, 2006.
- [97] S Shigematsu, T Kiyosue, T Sato, and M Arita. Rate-dependent prolongation of action potential duration in isolated rat ventricular myocytes. *Basic Res Cardio*, 192:123 – 128, 1997.
- [98] S Shigematsu, T Maruyama, T Kiyosue, and M Arita. Rate-dependent prolongation of action potential duration in single ventricular myocytes obtained from hearts of rats with streptozotocin-induced chronic diabetes sustained for 30-32 weeks. *Heart Vessels*, 9:300–309, 1994.
- [99] J Shlens. A tutorial on principal components analysis, version 2. *http : //www.sn1.salk.edu/ shlens/pub/notes/pca.pdf*, December 2005.

- [100] HD Simms and DB Geselowitz. Computation of heart surface potentials using the surface source model. *Journal of Cardiovascular Electrophysiology*, 6:522, 1995.
- [101] MN Stagnitti. The prevalence of obesity and other chronic health conditions among diabetic adults in the US community population. Technical report, Center for Financing, Access, and Cost Trends, AHRQ, Medical Expenditure Panel Survey-Household Component, 2001.
- [102] PC Stanley and TC Pilkington. The combination method: A numerical technique for electrocardiographic calculations. *IEEE Transactions On Biomedical Engineering*, 36(4):456–461, 1989.
- [103] B Tilg, G Fischer, R Modre, F Hanser, B Messnarz, M Schocke, C Kremser, T Berger, F Hintringer, and FX Roithinger. Model-based imaging of cardiac electrical excitation in humans. *IEEE Transactions On Medical Imaging*, 21:1031–1039, 2002.
- [104] JW Trobaugh and RM Arthur. Methods for using ultrasound to generate a heart surface for electrocardiographic inverse problems. *International Journal of Bioelectromagnetism*, 5:314–315, 2003.
- [105] L Tung. *A bidomain model for describing ischemic myocardial D-C potentials*. PhD thesis, MIT Cambridge, 1978.
- [106] A van Oosterom. The dominant T wave and its significance. *Journal of cardiovascular Electrophysiology*, 14:180–187, 2003.
- [107] A van Oosterom. Genesis of the t wave as based on an equivalent surface source model. *Journal of Electrocardiology*, 34S:217–227, 2001.
- [108] A van Oosterom. solidifying the solid angle. *Journal of electrocardiology*, vol:35 Suppl:181–92, 2002.
- [109] A van Oosterom and G Huiskamp. The effect of torso inhomogeneities on body surface potentials quantified using 'tailored' geometry. *Journal of Electrocardiology*, 22:53–72, 1989.
- [110] A van Oosterom and V Jacquemet. A parameterized description of transmembrane potentials used in forward and inverse procedures. *Folia Cardiologica*, 12 (suppl D):111–114, 2005.
- [111] A van Oosterom and T Oostendorp. ECGSIM; an interactive tool for studying the genesis of QRST waveforms. *Heart*, 90:165–168, 2004.
- [112] A van Oosterom and J Strackee. The solid angle of a plane triangle. *IEEE Trans Biomed Engr*, 30(2):125–6, 1983.

- [113] M Veglio, M Borra, LK Stevens, JH Fuller, and PC Perin. The relation between QTc interval prolongation and diabetic complications. the eurodiab iddm complication study group. *Diabetologia*, 42:68–75, 1999.
- [114] G Wahba. Practical approximate solutions to linear operator equations when the data are noisy. *SIAM Journal on Numerical Analysis*, 14:651–67, 1977.
- [115] Johan E.P. Waktare. Cardiology patient page - atrial fibrillation. *Circulation*, 106:14–16, 2002.
- [116] Y Wang, EB Rimm, MJ Stampfer, WC Willett, and FB Hu. Comparison of abdominal adiposity and overall obesity in predicting risk of Type 2 diabetes among men. *American Journal of Clinical Nutrition*, 81:555–563, 2005.
- [117] SG Wannamethee, AG Shaper, and L Lennon. Cardiovascular disease incidence and mortality in older men with diabetes and in men with coronary heart disease. *Heart*, 90:1398–1403, 2004.
- [118] GS Watson. Linear least squares regression. *The Annals of Mathematical Statistics*, 38:1679–1699, 1967.
- [119] WC Willett, WH Dietz, and GA Colditz. Guidelines for healthy weight. *The New England Journal of Medicine*, 341(6):427–434, 1999.
- [120] CY Wong, T O’Moore-Sullivan, R Leano, N Byrne, E Beller, and TH Marwick. Alterations of left ventricular myocardial characteristics associated with obesity. *Circulation*, 110:3081–3087, 2004.
- [121] World Health Organization. Obesity: Preventing and managing the global epidemic - report on a who consultation (technical report series). Technical Report 894, World Health Organization, 2000.
- [122] Z Xu and GJ Rozanski. K<sup>+</sup> current inhibition by amphiphilic fatty acid metabolites in rat ventricular myocytes. *Am J Physiol Cell Physiol*, 275:1660–1667, 1998.
- [123] Yale University Yale Animal Resources Center. Veterinary clinical services - normative data. [http : //www.med.yale.edu/yarc/vcs/normativ.htm](http://www.med.yale.edu/yarc/vcs/normativ.htm).
- [124] GX Yan and C Antzelevitch. Cellular basis for the normal T wave and the electrocardiographic manifestations of the long-QT syndrome. *Circulation*, 98:1928–1936, 1998.

# Vita

Shuli Wang

- Date of Birth**      June 17, 1978
- Place of Birth**      Inner Mongolia, China
- Degrees**              B.S. Electrical Engineering, Tianjin University, 2000  
M.E. Control System, Chinese Academy of Sciences, 2003  
M.S. Electrical Engineering, Washington University in Saint  
Louis, 2005
- Professional  
Societies**              Society for Industrial and Applied Mathematics (SIAM)  
Association for Computing Machinery (ACM)  
Chinese Academy of Sciences
- Publications**        Shuli Wang, R.M. Arthur, "A New Method for Estimating  
Cardiac Transmembrane Potentials from the Body Surface",  
*International Journal of Bioelectromagnetism*, 11(1), 59-63,  
2009.
- R.M. Arthur, Shuli Wang, and J. W. Trobaugh, "Changes in  
Body-Surface Electrocardiograms from Geometric Remodel-  
ing due to Obesity", *International Journal of Bioelectromag-  
netism*, 11(1), 46-49, 2009.
- Shuli Wang, R. Martin Arthur, Jason Trobaugh, "Body-Surface  
Electrocardiography Variations Caused by Changes in Car-  
diac Geometry Due to Diabetes and Obesity", *the 4th Mem-  
phis BioImaging Symposium*, Memphis, TN, Nov. 2007

December 2009



**Remodeling in Diabetes and Obesity, Wang, Ph.D. 2009**